

AD-A109 846

MASSACHUSETTS INST OF TECH CAMBRIDGE DEPT OF OCEAN E--ETC F/G 13/10
EXPERIMENTAL METHODS FOR THE PREDICTION OF THE EFFECT OF VISCOS--ETC(U)

JUN 81 S KOBAYASHI

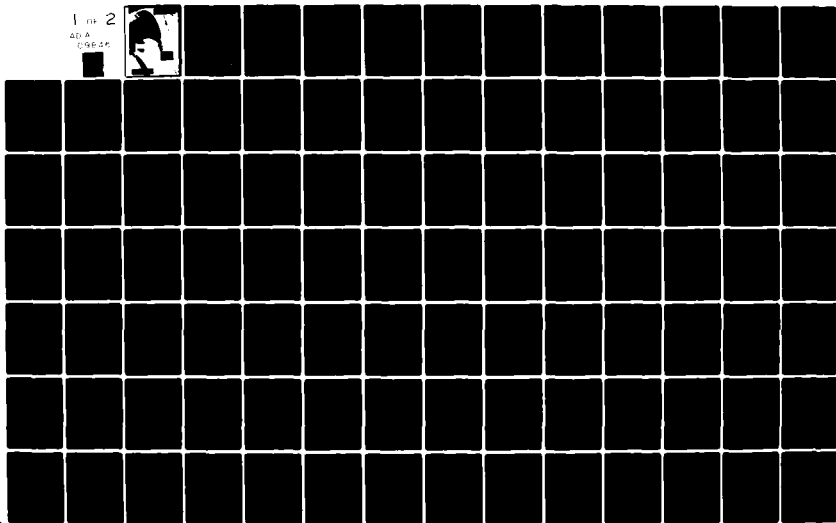
N00014-76-C-0357

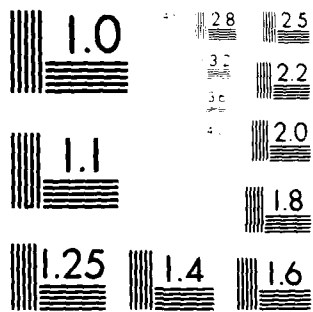
UNCLASSIFIED

OE-81-7

NL

1 OF 2
AD-A
000 00





MICROCOPY RESOLUTION TEST CHART
NATIONAL BUREAU OF STANDARDS-1963-A

12

LEVEL

Experimental Methods for
the Prediction of the Effect of
Viscosity on
Propeller Performance

by
Sukeyuki Kobayashi

AD A109846

DTIC
ELECTE
JAN 20 1982
B

Report No. 81-7
June 1981

Massachusetts Institute of Technology
Department of Ocean Engineering
Cambridge, Ma. 02139

DISTRIBUTION STATEMENT A

Approved for public release;
Distribution Unlimited

MASSACHUSETTS INSTITUTE OF TECHNOLOGY
DEPARTMENT OF OCEAN ENGINEERING
CAMBRIDGE, MASS. 02139

Technical Report

OE -

Report No. 81-7

EXPERIMENTAL METHODS FOR THE PREDICTION
OF THE EFFECT
OF VISCOSITY ON PROPELLER PERFORMANCE

by

Sukeyuki Kobayashi

June 1981

Reproduction in whole or in part is permitted
for any purpose of the United States Government.

Approved for public release; distribution unlimited

This research was carried out under the
Naval Sea Systems Command
General Hydromechanics Research Program
Subproject SR 009 01 01, Administred by the
Naval Ship Research and Development Center
Office of Naval Research Contract N00014-76-C-0357
MIT OSP 83456

DTIC
SELECTED
JAN 20 1982
B

SECURITY CLASSIFICATION OF THIS PAGE (When Data Entered)

REPORT DOCUMENTATION PAGE		READ INSTRUCTIONS BEFORE COMPLETING FORM
1. REPORT NUMBER 81-7	2. GOVT ACCESSION NO. AD-A109 846	3. RECIPIENT'S CATALOG NUMBER
4. TITLE (and Subtitle) EXPERIMENTAL METHODS FOR THE PREDICTION OF THE EFFECT OF VISCOSITY ON PROPELLER PERFORMANCE		5. TYPE OF REPORT & PERIOD COVERED Technical Report
7. AUTHOR(s) Sukeyuki Kobayashi		6. PERFORMING ORG. REPORT NUMBER
9. PERFORMING ORGANIZATION NAME AND ADDRESS Department of Ocean Engineering MIT, Cambridge, MA 02139		8. CONTRACT OR GRANT NUMBER(s) N00014-76-C-0357
11. CONTROLLING OFFICE NAME AND ADDRESS Office of Naval Research		10. PROGRAM ELEMENT, PROJECT, TASK AREA & WORK UNIT NUMBERS SR 009-01-01
13. MONITORING AGENCY NAME & ADDRESS (if different from Controlling Office) David W. Taylor Naval Ship Research and Development Center Bethesda, MA 20084		12. REPORT DATE June 19, 1981
		13. NUMBER OF PAGES 153
		15. SECURITY CLASS. (of this report) Unclassified
		15a. DECLASSIFICATION/DOWNGRADING SCHEDULE
16. DISTRIBUTION STATEMENT (of this Report) This document has been approved for public release and sale; its distribution is unlimited.		
17. DISTRIBUTION STATEMENT (of the abstract entered in Block 20, if different from Report)		
18. SUPPLEMENTARY NOTES		
19. KEY WORDS (Continue on reverse side if necessary and identify by block number) Propeller Blade Profile Drag Vorticity Boundary Layer Laser Doppler Velocimeter		
20. ABSTRACT (Continue on reverse side if necessary and identify by block number) A Laser Doppler Velocimeter (LDV) was used to perform a pro- peller wake survey for DTNSRDC propellers 4381 and 4383. Three components of the velocity were measured and from this, the velocity field and the vorticity field were constructed. Through a coordinate transformation, the vorticity field was separated into two parts i.e., trailing vorticity and boundary layer type vorticity in the viscous wake.		

DD FORM 1473
1 JAN 73

EDITION OF 1 NOV 65 IS OBSOLETE
S/N 0102-014-6601

SECURITY CLASSIFICATION OF THIS PAGE (When Data Entered)

SECURITY CLASSIFICATION OF THIS PAGE(When Data Entered)

The data was used for the prediction of propeller blade profile drag (viscous sectional drag). The idea of hypothetical flow by Betz was extended to propeller flow and a formula for the profile drag was derived in terms of velocities, which is suitable for LDV application. The radial distribution of profile drag was computed using the velocity data. It was shown that the value of Cd is close to that of 2-dimensional section at mid-radius range, but becomes substantially lower at inner and outer radii and that it goes up again near the tip and the hub. This trend is consistent with the behavior of profile drag of a finite span wing.



Accession For		
NTIS CHAI	<input checked="" type="checkbox"/>	
DTIC TAB	<input type="checkbox"/>	
Unannounced	<input type="checkbox"/>	
Justification		
Distribution/		
Availability Codes		
Dist and/or		
Dist Special		
A		

EXPERIMENTAL METHODS FOR THE PREDICTION
OF THE EFFECT
OF VISCOSITY ON PROPELLER PERFORMANCE

by

Sukeyuki Kobayashi

This report is essentially identical to the thesis submitted by the author in May, 1981 in partial fulfillment of the requirements for the degree of Doctor of Philosophy at the Massachusetts Institute of Technology.

Thesis Supervisor: Justin E. Kerwin
Professor of Naval Architecture

ABSTRACT

A Laser Doppler Velocimeter (LDV) was used to perform a propeller wake survey for DTNSRDC propellers 4381 and 4383. Three components of the velocity were measured and from this, the velocity field and the vorticity field were constructed. Through a coordinate transformation, the vorticity field was separated into two parts i.e., trailing vorticity and boundary layer vorticity in the viscous wake.

The data was used for the prediction of propeller blade profile drag (viscous sectional drag). The idea of hypothetical flow by Betz was extended to propeller flow and a formula for the profile drag was derived in terms of velocities, which is suitable for LDV application. The radial distribution of profile drag was computed using the velocity data. It was shown that the value of C_d is close to that of 2-dimensional section at mid-radius range, but becomes substantially lower at inner and outer range, but becomes substantially lower at inner and outer radii and that it goes up again near the tip and the hub. This trend is consistent with the behavior of profile drag of a finite span wing.

ACKNOWLEDGEMENTS

This thesis project was supported by The U.S. Navy GHR Contract No. N00014-76-C-0357.

I would like to express my gratitude to my thesis supervisor Professor Justin E. Kerwin for his continuous support and advice given during my graduate study at the Massachusetts Institute of Technology.

I also would like to express my appreciation to my thesis committee members; to Professor Eugene. E. Covert who gave many important suggestions as an aerodynamics expert, to Professor Patrick Leehey who stimulated my energy to attack the problems through the questions and to Professor Robert J. Van Houten whoes deep understanding on the topic often encouraged me.

Special thanks are extended to Mr. S. Dean Lewis, in charge of the Marine Hydrodynamics Laboratory, for his advice and assistance which often made the experiments more efficient, and to Dr. Keh-Sik (Peter) Min who taught me everything about the LDV and motivated me into this thesis work.

I would like to thank my friends and colleagues who helped me out in various ways :

David S. Greeley and James S. Uhlman Jr. often joined me in the discussions of the experimental results and gave me useful suggestions and sometimes were willing to give me the computational results to compare with the experiment. Dave also offered a kindness to check the wordings and

expressions in this paper which was written by a non-native speaker of English.

Elwyn S. Baker spent a considerable amount of time to discuss with me the flow around a moving source.

Robert B. Schoenberger worked hard one summer to add the LDV the third degree of freedom. Without his work, the vorticity measurement would have been impossible.

Eduardo Moas' experiment with 2-D hydrofoil was a great help to prove the validity of the formula for the profile drag.

Jens P. Kaalstad's help in the experiment with the 3-D hydrofoil saved my time during the rush toward the completion of this thesis.

Dr. A. Bruce Dunwoody's and Dr. R. Brad Campbell's efforts to initialize the digital plotter which was used to draw the nice graphs in this paper are greatly appreciated.

Mr. Raymond E. Johnson and his colleagues' professional skills were great back-up in the experiments. Especially, I was lucky to use the newly polished plexiglass (optical) window done by his team for the LDV measurements.

Miss Joanne M. Sullivan's secretarial ability (in arranging the thesis committee meetings, etc.) saved me a great amount of time and I could concentrate more on my thesis work.

I also owe many other people who directly or indirectly helped me through the whole process toward the degree.

My gratitude goes to my parents who gave the strength and confidence in me to accomplish the work toward the

degree and who gave supports to me in various ways.

My appreciation is given to my parents-in-law (Mr. and late Mrs. Yoshio Ando) who showed deep understanding in me and gave continuous support.

I have to confess that without the continuous support and encouragement of my wife Eiko, the life as a student here at MIT would have been impossible. I owe her forever.

Finally, my wife and I would like to thank Dr. and Mrs. Ralph Katz for having been our host family. Their hospitality has made our life here very much enjoyable.

Sukeyuki Kobayashi

May 1981

TABLE OF CONTENTS

Title	Page
Report Documentation Page	1
Abstract	1b
Acknowledgements	2
Table of Contents	5
List of Tables and Figures	7
Nomenclature	11
1. Indroduction	15
2. Experimental Facility	18
MIT Water Tunnel	18
LDV System	18
Data Acquisition	18
Propellers	19
Wall Effect	19
3. Experiments and Results	21
3.1 Field Point Velocity and Vorticity	21
Coordinate Systems	21
Construction of Velocity Field	22
Vorticity Field	25
3.2 Discussion on Velocity and Vorticity Field	26
Velocity Field	26
Comparison with FPV-10 Output	31
Vorticity Field	32
Error in Vorticity	35

Title	Page
4. Profile Drag of Propeller Blade	38
4.1 Derivation of The Formula	39
Momentum Theorem	39
Introduction of Hypothetical Flow	41
Decomposition of Force and Moment	47
The Force and Moment computed in Hypothetical Flow	49
Construction of Hypothetical Flow	51
4.2 Application to 2-D Hydrofoil	53
Formula	53
Construction of Hypothetical Flow	55
Experimental Results	57
4.3 3-D Hydrofoil	59
4.4 Application to Propeller	61
Formula	61
Construction of Hypothetical Flow for Propeller	69
Induced Velocity	71
Profile Drag Coefficient	72
Results	76
5. Conclusions	81
References	84
Appendix A	88

List of Tables

	Title	Page
Table 2-1	Data Acquisition System	90
2-2	Geometry of The Propellers	91
3-1	Distance from T.E. along Helical Line to Each Measurement Point	93
4-1	Experimental Conditions (2-D Hydrofoil)	58
4-2	Dimensions of the Model and Experimental conditions (3-D Hydrofoil)	59

List of Figures

Figure 2-1	Experimental Set-up for Velocity Measurement	94
2-2	Schematic Representation of Data Acquisition System	94
2-3	Result of Open Water Test DTNSRDC4381	95
2-4	" 4382	95
2-5	" 4497	96
2-6	" 4383	96
2-7	" 4498	97
3-1	Coordinate systems	22
3-2	Restriction to the LDV measurement	24
3-3	Measurement Stations for Vorticity	26
3-4	Coordinate Transformation	33
3-5	Field Point Velocity Measured by LDV	97

	Title	Page
Figure 3-6	Field Point Velocity (3-components)	98
	Prop.4381 at $x=-0.333R$	
3-16	and at various radii	114
3-17	Field Point Velocity (3-components)	114
	Prop.4383 at $x=-0.488R$	
3-24	and at various radii	126
3-25	Vorticity Distribution	
	Prop.4381 at $x=-0.333R$, $r=0.7R$ at Design J	126
3-26	Velocity Component Parallel to Viscous Wake	
	Prop.4381	127
3-27	"	Prop.4383 127
3-28	Geometry of the Two Wakes	
	Prop.4381 at $x=-0.333R$	128
3-29	"	Prop.4383 at $x=-0.488R$ 128
3-30	Field Point Velocity Prop.4381	
	at $x=-1.0R$, $r=0.7R$	129
3-31	"	at $x=-2.0R$, $r=0.7R$ 130
3-32	FPV-10 Output at $x=-0.333R$, $r=1.0R$ Prop.4381	132
3-33	Field Point Velocity (Measured)	
	Prop.4381 at $x=-0.333R$, $r=1.0R$	132
3-34	PSFFPV Output at $x=-0.333R$, $r=1.0R$	
	Prop.4381	133
3-35	FPV-10 Output at $x=-0.333R$, $r=0.7R$	
	Prop.4381	133

Title	Page
Figure 3-36 Field Point Velocity (Measured)	
Prop.4381 at $x=-0.333R$, $r=0.7R$	134
3-37 FPV-10 Output at $x=-0.470R$, $R=0.924R$	
Prop.4383	134
3-38 Field Point Velocity (Measured)	
Prop.4383 at $x=-0.470R$, $r=0.924R$	135
3-39 } Transformed Vorticity	135
} Prop.4381 at $x=-0.333R$,	
3-48 } and at various radii	140
3-49 } Transformed Vorticity	140
} Prop.4383 at $x=-0.488R$	
3-56 } and at various radii	144
3-57 Slope of Bound Circulation	144
4-1 Formulation of the Problem	39
4-2 Hypothetical Flow	43
4-3 2-D Hydrofoil	53
4-4a Velocity Distributions	
NACA 0012 at 0 angle of attack	145
4-4b Vorticity Distribution "	145
4-5a Velocity Distributions	
NACA 66-309 @4.5deg. $Re=900000$	146
4-5b Vorticity Distribution "	146
4-6a Velocity Distributions	
NACA 66-309 @4.5deg. $Re=2000000$	147
4-6b Vorticity Distribution "	147

	Title	Page
Figure 4-7	Coefficient of Profile Drag Obtained at Several Measurement Points	148
4-8	3-D Hydrofoil and the Coordinate System	60
4-9	Velocity in the Wake SNAME Keel Model No.3 ($z=-0.625c$)	148
4-10	" ($z=-0.125c$)	149
4-11	" ($z=-0.063c$)	149
4-12	" (Across the Tip Vortex)	150
4-13	" (" in z)	150
4-14	Spanwise Distribution of Profile Drag SNAME Keel Model No.3	151
4-15	Control Volume	62
4-16	Expanded View of Velocity Diagram	75
4-17	Hypothetical Velocity Constructed from Measured Velocity and Vorticity Prop.4381	151
4-18	Hypothetical Velocity obtained from Constant Pressure Assumption Prop.4381	152
4-19	C_d obtained at different locations Prop.4381 at Design J ($0.7R$)	152
4-20	Coefficient of Profile Drag Prop.4381 and 4383 at Design J	153

NOMENCLATURE

c	chord length
C_d	coefficient of profile (viscous sectional) drag $= \text{Drag} / \frac{1}{2} \rho U_\infty^2 c \quad \text{for hydrofoil}$ $= D R_i / \frac{1}{2} \rho (\nabla \lambda^2 + r^2 \omega^2) c \quad \text{for propeller}$
C_L	coefficient of lift (sectional)
D	propeller diameter
$D R_i$	sectional drag force on the propeller blade
F_B	force on the solid body in the flow
F_{BL}	lifting force on the body
F_{BD}	drag on the body
F_{buoy}	buoyancy force
F^*	force on the singularities in the hypothetical flow
F_L^*	lifting force in the hypothetical flow
F_D^*	drag force in the hypothetical flow
F_{sec}	sectional force
f_M	section camber
g	acceleration of gravity
G	potential of gravity
i, j, k	indices for x, r, θ
J	advance coefficient $= \frac{V_A}{nD}$
J'	$= J / \pi \left(\frac{r}{c} \right)$
K	number of propeller blades
K_T	thrust coefficient
K_Q	torque coefficient
M_B	moment on the body in the flow

M_{BL}	lifting moment on the body
M_{SD}	drag moment on the body
M_{Buoy}	buoyancy moment on the body
M^*	moment on the singularities in the hypothetical flow
M_L^*	lifting moment in the hypothetical flow
M_D^*	drag moment in the hypothetical flow
M_{sec}	sectional moment
n	propeller revolution
n	normal unit vector
P	propeller section pitch
p	static pressure
q	strength of the source
Q	total flux from the source distribution
R	propeller radius
Re	Reynolds number, $= U_\infty c / \nu$ (hydrofoil), $= \sqrt{V_A^2 + (0.7R\Omega)^2} c / \nu$ (propeller blade)
\mathbf{r}	position vector
r	radial position
S	control surface fixed in space
S'	control surface moving with the fluid material
S_B	surface of the body
s	control line (in 2-D flow)
Sw	a part of the control surface which is in the wake
t	time
t	maximum thickness of propeller blade section
U_∞	inflow velocity
U_R	reference velocity, $= \sqrt{V_A^2 + (0.7R\Omega)^2}$

V	control volume fixed in space
V^*	control volume fixed in space for the hypothetical flow
V'	control volume moving with the fluid particle
$V^{*'} $	control volume moving with the fluid particle for the hypothetical flow
V_A	inflow velocity to the propeller
V_b	volume of the solid body
V_e	infinitesimal volume
V_s	volume of the source distribution
\mathcal{V}	velocity vector
\mathcal{V}^*	hypothetical velocity
\mathcal{V}_i	induced velocity
α	angle of attack
β	hydrodynamic pitch angle without induced velocity
β_i	hydrodynamic pitch angle with induced velocity
Γ	circulation
γ	$\beta_i - \beta$
ϵ	error
η	propeller efficiency
θ_s	projected skew angle at radius r
ν	kinematic viscosity
ρ	density of the fluid
τ	time (dummy variable)
ϕ_s^*	velocity potential for the source
Ω	angular velocity of propeller rotation
ω	vorticity vector

ω_r vorticity of the trailing vortex
 ω_θ vorticity of the viscous wake

Coordinate systems

Unit Vectors

o-xyz space fixed Cartesian coordinates	i, j, k
o-xy'z' propeller fixed Cartesian	i', j', k'
o-xr θ space fixed cylindrical	i, e_r, e_θ
o-xr θ' propeller fixed cylindrical	$i', e_{r'}, e_{\theta'}$
o'- $\xi\eta\zeta$ transformed coordinates (Propeller fixed)	

1. Introduction

Marine screw propeller is relatively new in the long history of ships which is comparable to the history of mankind itself. It was only a hundred years ago when the propeller took the present style[1]. Since then, through various evolutionary stages, it has been used almost exclusively as a mean of ship propulsion.

During last two decades, rapid growth of computer technology has made it possible for theoretical and numerical methods to analyze various problems in science and engineering. The field of marine propeller hydrodynamics is not an exception. More than a few computer programs have been or are being developed using numerical lifting-line or lifting-surface theory.

At MIT, there has been a continuous effort for over 20 years by Kerwin and his colleagues to develop computer programs for the design of propeller blades and for the prediction of propeller performance, based on numerical lifting surface theory[2]. The effort has produced some of the best propeller programs around, such as PUF-2[3], PUF-3[4], PBD-10[5] and FPV-10[6].

At almost the same period of time, Laser Doppler Anemometry was introduced as a powerful tool in experimental fluid dynamics. In certain areas of experiments, it enabled us to read flow velocity directly with a very good accuracy and spatial resolution without disturbing the flow. At the Department of Ocean Engineerig, MIT, Laser Doppler

Velocimeter (LDV) has been in operation since 1977. Min[7] was the first to set up the Laser apparatus and bring it into work. He showed various possibilities of the flow measurement around a propeller, thus proving the powerfulness of LDV. After having successfully shown its capability, the LDV is now being used to back up those computer programs as well as in various experiments.

This thesis is intended to extend the work done by Min. Among several things to be done, the author has been particularly interested in the prediction of the profile drag (viscous sectional drag) of a propeller blade, using the velocity data obtained by LDV, which has never been tried so far.*

The current versions of the programs use a constant value for the coefficient of the profile drag (C_d) over the radius of the propeller blade. By feeding the actually measured values of the drag distribution, it is expected that the accuracy of the programs will improve, especially of the design program (PBD-10). One of the objectives of this paper, therefore, is to supply such information using the experimental data obtained by the LDV.

In this paper, the method of Betz[8] for the prediction of profile drag which uses the concept of hypothetical flow

*) There have been some examples of LDV application to lift measurement such as Sayre[9] or Orloff[10]. But as far as the author knows, there is no example of profile drag measurement by LDV.

will be generalized first and a formula will be given in terms of velocities as opposed to in terms of pressures which was given by Betz. A method to obtain the hypothetical flow from measured velocity data will also be discussed.

The measured velocity field, and vorticity distribution which is derived from the velocity data will be presented also, and the flow field in the propeller wake will be discussed. The propellers tested are DTNSRDC research propellers 4381 (no blade skew) and 4383 (with 72 deg skew).

2. Experimental Facility

MIT Water Tunnel The experiments were done in the Variable Pressure Water Tunnel of the Marine Hydrodynamics Laboratory, Department of Ocean Engineering, MIT.

As Min[7] mentions, this water tunnel is ideal for Laser measurements. The tunnel is a closed circulating channel, having a square test section with transparent plastic(plexiglass) viewing windows on four sides. The size of the test section is 20" x 20" and the viewing window is 44" x 16" x 2" thick. The tunnel operates in the speed range of 0 to 30 ft/sec.

LDV system The LDV system is manufactured by Thermo Systems Inc. with Spectra Physics 15mW He-Ne Laser and has Dual Beam Forward Scatter Mode. The LDV mount has a traverse system which has 3-degrees of freedom. Traversing is done by turning the handles by hand, and the position of the Laser beam crossing point is obtained by reading the scales attached to the mount. This traverse gear is rather simple. However, careful reading of the scales can give as much as 0.1mm resolution.

Data Acquisition Data acquisition and reduction is done by a mini-computer (Digital Equipment MINC-11) through an A/D converter. Data sampling is possible at a rate as high as 20kHz. If the propeller rotates at 900rpm, for instance, this gives a resolution of 0.27 degree in angle. The

characteristics of the MIT Water Tunnel LDV and Data acquisition systems are summarized in Table 2-1. The experimental set-up is illustrated in Figure 2-1 and the diagram of data acquisition system is illustrated in Figure 2-2.

Propellers The propellers tested are DTNSRDC 4381 and 4383 research propellers of 12 inch diameter, out of a series of 5 propellers with systematically changing skew and rake[11,12]. Propeller 4381 is the parent propeller of the series and has no blade skew. Propeller 4383 has 72 degree blade skew and also skew induced rake. The principal dimensions are given in Table 2-2. They were designed to give the same performance characteristics (K_T, K_Q, η) at the design condition of $J=.889$. Figures 2-3 through 2-7 show the result of open water tests done in the MIT Water Tunnel recently. The propeller efficiencies at design J are similar to each other except for Prop.4381 which has lower efficiency than the others. This is due to the fact that, as the parent propeller, it has been used more than any others in the series and has been wearing and getting roughened leading edges.

Wall Effect For experiments in the water tunnel, there is always a problem to be kept in mind. That is the tunnel wall effect or so-called blockage effect. The presence of the walls give a restriction to the flow. The streamlines on the wall have to be parallel to it, since no flow into

the wall is possible. This distorts the flow from what it would be in an unbounded fluid flow. The significance of this effect varies depending on the kind and size of the test model one uses, as well as the flow conditions. For the propeller 4381 operating at the design condition, the magnitude of the wall effect was checked using FPV-10. By replacing the walls with the images of the propeller, it is possible roughly to know the wall effect. At $J=.889$ and at $0.7R$, for example, this effect is about a few per cent at most. Hence it can be said that the wall effect is negligible in this particular case. In the computation of profile drag, the flow is assumed to be unbounded.

3. Experiments and Results

3.1 Field Point Velocity and Vorticity

Coordinate Systems Four coordinate systems are used :

i) Cartesian coordinates o-xyz

where the x-axis is along the propeller shaft center line, pointing upstream. The y-axis is set horizontally toward starboard and the z-axis is vertically downward. The y-z plane corresponds to the center plane of propeller rotation.

ii) Cylindrical coordinate system o-xr θ

where r is radially outward, θ goes clockwise when looked from downstream, and the r- θ plane is identical to y-z plane. $\theta=0$ corresponds to the y-axis.

There is a relation between the two systems, which is

$$\left. \begin{aligned} y &= r \cos \theta \\ z &= r \sin \theta \end{aligned} \right\} \quad (3-1)$$

The above two are space-fixed (or tunnel-fixed) frames of reference. The following are blade attached coordinate systems :

iii) Cartesian coordinates o-xy'z'

iv) Cylindrical coordinates o-xr θ'

Each of the two moving systems is defined to be in the same way as i) or ii) at time 0.

The relations between the coordinate systems are :

$$\left. \begin{aligned} \theta' &= \theta - \Omega t \\ y' &= r \cos \theta' = y \cos \Omega t + z \sin \Omega t \\ z' &= r \sin \theta' = z \cos \Omega t - y \sin \Omega t \end{aligned} \right\} \quad (3-2)$$

where Ω is angular velocity of the propeller rotation, which is constant in this paper.

The unit vectors are also defined as shown in the figure below.

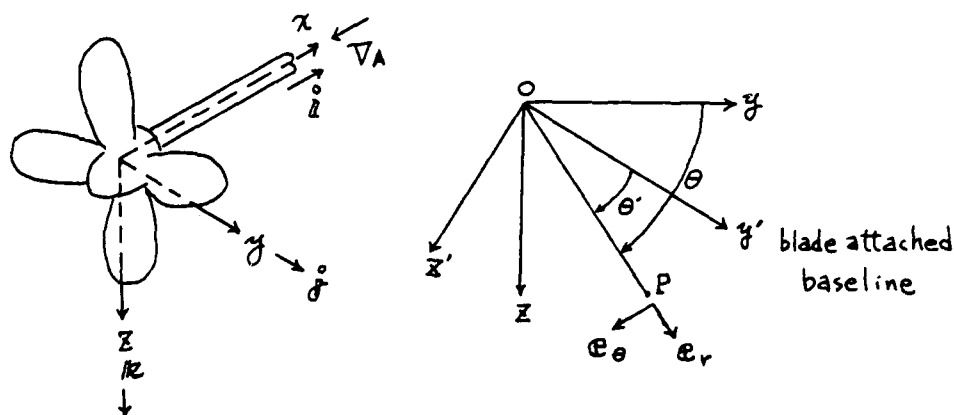


Figure 3-1 Coordinate systems

Construction of Velocity Field The Laser system in the MIT Water Tunnel is a one component Laser which reads one component of the velocity at a time. Therefore, to get three components, three identical running conditions have to be repeated. The axial component is taken essentially at any location as long as the beam crossing point is visible from the photo-multiplier. But it is convenient if the measurement point is on the z -axis where the radial component can be also measured. The radial component is taken as the vertical component on z -axis, and the tangential component can be measured as the vertical velocity component along the y -axis. The velocity field can be constructed from the 3 velocity components thus obtained. This technique is only valid when the flow around the

propeller is steady, in other words, constant propeller rotation in a uniform flow or in an axisymmetrical flow. The phase lag between the velocity components measured at different places will be taken care of by shifting the phase of the data in the computer.

The propellers were run at 900rpm most of the time, which gives blade Reynolds No. of 0.5×10^6 to 1.5×10^6 . A few data were taken at 600 and 1200rpm also. One limitation is that we can not get broad range of Reynolds No. in MIT Water Tunnel if we are to run the propeller at one fixed J.

The Laser signal usually contains noise from various sources as mentioned by Min[7]. Removal of noise from the real signal is necessary. One possibility is averaging (ensemble average). If the flow is laminar, this technique gives good results. If the flow contains turbulence, however, this will eliminate the turbulence component together with the noise. Taking rms turbulence may be satisfactory, but discrimination of noise from turbulence remains a problem. Although it is said that turbulence measurement is possible by LDV[13], the author is not quite convinced of that, at least with the propeller flow. When calculating drag from wake survey data, velocity comes in quadratic form in the momentum flux. If there is 10% turbulence in the flow, for example, this becomes a 1% fluctuation in momentum. Fortunately, in most of the conditions discussed in this paper, the turbulence level in the propeller wake is considered to be relatively small. Hence, turbulence is neglected and only mean velocities are

measured.

Figure 3-5 shows an example of ensemble average of the velocity for 360 degrees.

Figures 3-6 a,b,c to 3-24 a,b,c show the field point velocities taken at various radii on the $x=-0.333R$ (downstream) plane for Prop.4381 and on the $x=-0.488R$ plane for Prop.4383. Each of these positions (in x) is almost the closest possible to each propeller in the downstream direction.

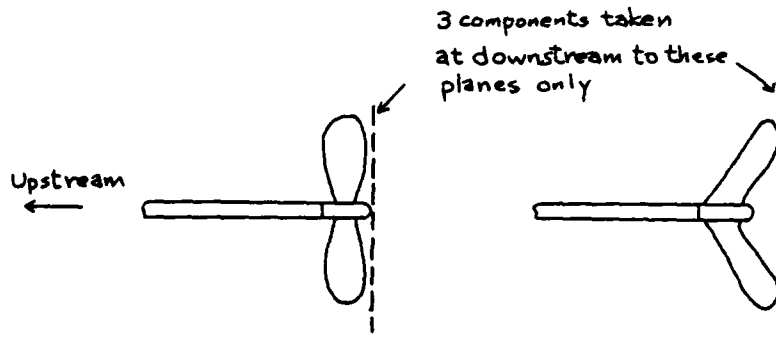


Figure 3-2 Restriction to the LDV measurement

In table 3-1 is shown the distance of each measurement point from the trailing edge, along the helical line constructed with uniform inflow and propeller rotation.

Data sampling frequency was either 10kHz or 20kHz and ensemble average of 1000 or 2000 was taken for each component. Only one blade passage is given here.

In these figures, sub number a is for x -component (axial), b is for r -component (radial) and c is for θ -component (tangential). Note that the frame of reference is fixed in space so that θ -component does not include

virtual velocity due to propeller rotation which will be observed from propeller-fixed frame of reference. The angle in the abscissa corresponds to $-\theta'$, since the measurement point moves in the negative θ' -direction against the propeller. Smaller angles correspond to the pressure side of the blade.

Note : The propeller rpm for these figures is 900rpm except for Figures 3-12, 3-22 (600rpm) and Figure 3-13 (1200rpm).

Vorticity Field Vorticity of the flow is given by

$$\omega = \nabla \times \mathbf{v} \quad (3-3)$$

Since the velocities are easily obtained, the computation of vorticity can be done through the formula (3-3) numerically.

If we discretize Eq.(3-3), we have

$$\begin{aligned} \omega_{i,j,k} = & \left(\frac{v_\theta}{r} + \frac{v_{\theta,i+1} - v_{\theta,i-1}}{2\Delta r} - \frac{1}{r} \frac{v_{r,k+1} - v_{r,k-1}}{2\Delta\theta} \right) \hat{z} \\ & + \left(\frac{1}{r} \frac{v_{x,k+1} - v_{x,k-1}}{2\Delta\theta} - \frac{v_{\theta,i+1} - v_{\theta,i-1}}{2\Delta x} \right) \hat{e}_r \\ & + \left(\frac{v_{r,i+1} - v_{r,i-1}}{2\Delta x} - \frac{v_{x,i+1} - v_{x,i-1}}{2\Delta r} \right) \hat{e}_\theta \end{aligned} \quad (3-4)$$

Where i is the subscript for x, j is for r and k is for θ .

To do this computation, four more measurement stations were set around the field point of interest and velocities were measured.

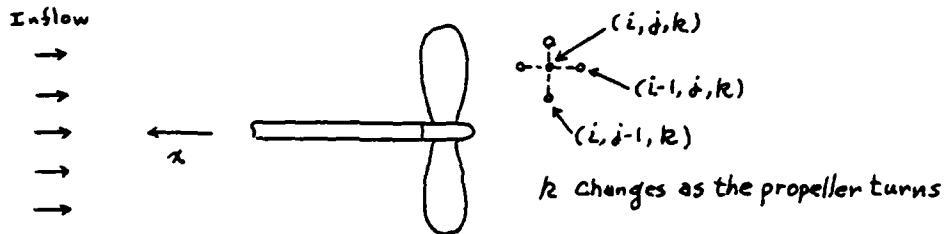


Figure 3-3 Measurement stations for Vorticity

Figure 3-25 shows an example of thus computed vorticities at the measurement point $x=-0.333R$, $r=0.7R$ for Propeller 4381. For the convenience of coordinate transformation which will be discussed later in drag calculation, the frame of reference is set to the propeller blade and the computation of vorticity was done in $xr\theta'$ coordinates. Therefore, twice the propeller rotation, 2Ω , is introduced into x -component. To distinguish the vorticity in blade attached coordinates from that in fixed frame of reference, the notations ω'_x , ω'_r and $\omega'_{\theta'}$ are used. If ω_x , ω_r and ω_{θ} represent the vorticity in space fixed coordinates, the relation between the two vorticities is :

$$\omega'_x = \omega_x - 2\Omega, \quad \omega'_r = \omega_r, \quad \omega'_{\theta'} = \omega_{\theta}$$

3.2 Discussion on Velocity and Vorticity Field

Velocity Field The three components of the velocity and vorticity tell us various things. First of all, if we look at the radial component of velocity, we find that the

velocity jump across the trailing vortex sheet is there. (In the real flow, of course, the sheet is not really a sheet of zero thickness, but has a finite thickness. The velocity jump has a width for transition as a consequence. However, the word 'sheet' will be used in this paper for convenience.) Although this component is not all for the flow due to trailing vortex, it is considered to be very close to it, especially for the no skewed propeller (Prop.4381). Vortex core type flow is well represented there as we expect (Figure3-11b for example).

This velocity jump switches its sign (the shape becomes the other way) as we go along r-direction. For Prop.4381, U_r at $r/R=0.6$ and above are different from that at $r/R=0.5$ and below. The implication is that the slope of the bound circulation changes its sign and consequently the sign of trailing vortex sheet changes at a point between the two corresponding radii. This occurs, on Prop.4383 between $r/R=0.6$ and 0.7 (Figures 3-20b and 3-21b).

As the measurement point moves radially outward toward the tip, the influence of tip vortex becomes pronounced. Since vorticity in the tip vortex is much stronger than the trailing vortex sheet, the velocity jump becomes much larger (Fig.3-15b and 3-24b). U_x and U_θ also pick up the influence of tip vortex. The large hump in U_x (Fig.3-15a and 3-24a) is the flow due to the tip vortex. Since this measurement point is still inside the slip stream ($0.91R$ for Prop.4381, $0.95R$ for Prop.4383 at these measurement locations), it appears as strong negative x-flow (in other

words, the same direction as freestream). At a point outside the propeller wake, the tip vortex gives positive x-flow as shown in Figure 3-16a. When this comes to U_θ , it is a little confusing, because it appears as a dent as shown in Figs. 3-15c and 24c. The first (i.e. at smaller angle) of the two dents in either figure is considered to be the wake which is due to the boundary layer and the second is the flow due to tip vortex. It is interesting to see that this component (θ -component) hardly picks up the influence of tip vortex once outside the wake (Fig.3-16c).

The wake of the blade (which comes off the boundary layer on the blade) appears as velocity defect (or dent) typically in x- or θ -component at most of the radii of measurement. (Let us call this 'viscous wake'.) However, by carefully examining the radial velocity component, we find that it is also there. The little hump on top of the velocity peak on pressure side of U_r in Figure 3-11b for example, is considered to be a projection of viscous wake. Across the sign change of trailing vortex, it then appears on the suction side as in Figure 3-9b. Since the flow field is under the strong influence of slipstream contraction, we can not say that the hump always has outward velocity. However, it consistently shows a tendency to go outward compared with the other part. This can be explained by centrifugal force. Due to the no-slip condition, the fluid in the boundary layer on the blade tends to move together with the blade. When it leaves the blade to form the wake, it tries to flow along the tangent line to that radius,

giving radial component to the velocity. It is also consistent with the idea of centrifugal force that the radial speed of the little hump increases toward outer radii. The magnitude of outward velocity may not change in proportion to r . It is expected that at some radii on the blade, there is a transition from laminar to turbulent flow. Once it is turbulent, the flow should have less influence from the blade[14], changing the magnitude of outward flow in the wake.

In Figures 3-26 and 3-27 are shown the projection of the velocity defect, at each radius of measurement, to the direction of the flow in the viscous wake (ξ -direction, say). The coordinate system here is blade attached. Hence, the velocity is larger at outer radii. Note that the abscissa is blade passage (in non-dimensional distance, $r/Rd\theta'$) and not in angle, consequently giving different lengths to one blade passage between different radii. The velocity defect is deeper at mid-radius range (in the vicinity of $r/R=0.6$), where the flow is considered to be reasonably 2-dimensional. Near the blade tip, or near the propeller hub, the velocity defect becomes shallower. This is particularly so for Prop.4383. One of the possible reasons for this is that there is a nontrivial 3-dimensional effect. At outer radii, relatively large centrifugal force and roll-up of the tip vortex may be causing cross flow. Near the propeller hub, where the distance between the blades becomes smaller and where blades go into the hub, strong interactions between them possibly exist, creating

another 3-dimensional effect.

One interesting thing is that the two sheets - trailing vortex and viscous wake - are not in the same location, as might be noticed when looking at the little hump in U_r . The hump is clearly off the center of velocity jump. This is not surprising at all since the origins of the two wakes are different. The trailing vortex is created by the presence of tip vortex while viscous wake comes from the boundary layers on the blade. Figures 3-28 and 3-29 illustrate the geometry of the two sheets and also in-plane velocity of each point on the sheets for the two propellers observed on the measurement planes ($x=-0.333R$ for Prop.4381 and $x=-0.488R$ for Prop.4383). These graphs were obtained by finding the angular location of the viscous wake and the center of the velocity jump using the graphs of U_r and U_θ . The graphs clearly show the different locations and motions of the two sheets. The sheets for Prop.4383 have larger curvature than Prop.4381, implying the effect of large skew of the blade. At outer radii, the trailing vortex sheet is fairly far away from the viscous wake, toward suction side. At the inner radii, the two sheets almost line up (.4R and below). Correspondingly, the viscous wake does not show itself in U_r .

Field point velocities were also measured at $x=-1.0R$ and $-2.0R$ at $r=0.7R$ for Prop.4381. They are shown in Figures 3-30 and 3-31. Two blade passages are shown in these figures. At $x=-1.0R$, the velocity defect and velocity jump are still there although becoming shallower and smaller

because of diffusion. But at $x=-2.0R$ they seem to have disappeared. It would be interesting to examine what is going on between these two points by taking finer spacing in x and getting more data.

Comparison with FPV-10 output As a byproduct of PUF-2, a field point velocity program (FPV-10[6]) was written and has been in use to predict field point velocities around the propeller. It is now possible by using the LDV to map the velocity field and back up the program.

At some measurement points, velocity components were compared with FPV-10 output. Since the program uses a potential flow model, we should not expect the velocity defect in the wake. First, comparisons were made in the potential flow region i.e. outside the wake. They are shown in Figures 3-32 and 3-33. There is some D.C. offset between the two, especially in the x -components. The amplitudes in the radial components are a little discrepant. Tangential components are close to each other. Phases in each velocity component are in good agreement. A modification to this program is being made as PSFFPV by Greeley[15]. An output of this program for the same field point is shown in Figure 3-34. Although there is D.C. offset, the amplitude of each component is closer to the measured velocity.

Once the field point is in the wake, there is some difference (Figs. 3-35 and 3-36). While the measured velocity shows a velocity defect in the wake of the blade,

the computed velocity does not. Since both velocities (measured and computed) must satisfy the continuity equation, discrepancy between the two is larger to compensate the velocity defect in the wake.

Figure 3-37 for the computed velocity (Prop.4383 $x=-.47R$, $r=0.924R$) shows the influence of tip vortex fairly well as compared with Figure 3-38, the measured. The peak in U_x (influence by tip vortex) in the computed velocity field is sharper than that measured. The difference is presumably due to the presence of the boundary layer in the real flow. It is considered that the boundary layer smears the tip vortex to some extent.

Vorticity Field The author tried to separate the vorticity in the wake of the propeller into two, corresponding to the two different types of wake, namely trailing vortex wake and viscous wake. This idea is also used by Tan[16] in the analysis of the wake of gas turbine rotor. The vorticity distributions obtained by Eq.(3-4), one example being shown in Figure 3-25 were transformed to a new coordinate system $o'-\xi\eta\zeta$, where ξ -axis is parallel to the flow at the center of trailing vortex wake. The second axis η was made to lie on the trailing vortex sheet. Consequently, the third axis ζ points normal to the trailing vortex sheet. The transformed vorticities are shown in Figures 3-39 through 3-56.

Since ξ -axis is set parallel to the trailing vortex, ω_ξ should represent trailing vorticity. This seems to be

almost successful at most radii. However, as discussed in the previous section, there is a component of viscous wake projected to r -direction and thus to the direction of the trailing vorticity. Therefore it is not completely possible to separate trailing vorticity from the others only by coordinate transformation. This projection appears as a small bump at the foot of large hump of trailing vorticity as shown in Figure 3-44 for instance. Except for that, ω_ξ is a fairly good even function of θ .

η -component shows typical vorticity distribution in the viscous wake. Since the wake comes from the boundary layers on both sides of the blade, this vortex component has two vortices with opposite signs. Hence the vorticity is an odd function of θ . The third component (ω_ξ) shows very little vorticity as is expected through the coordinate transformation. Due to the curvature of the wake sheets and also due to the fact that the two wake (trailing vortex and viscous) sheets are a little apart, this component does not become completely zero, or flat except at a few radii.

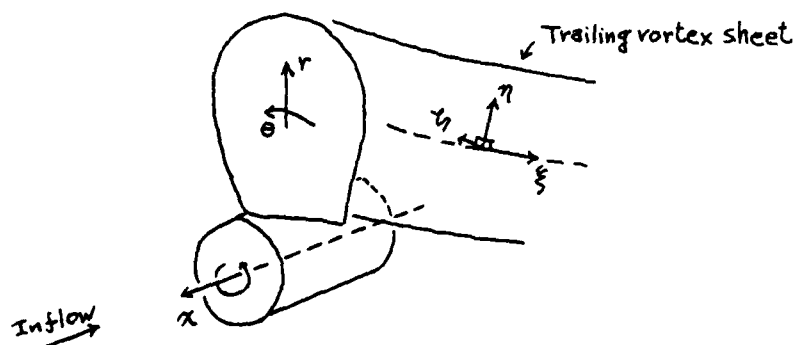


Figure 3-4 Coordinate Transformation

The vorticity plot becomes more noisy at inner radii toward the propeller hub. This is presumed mainly due to the finer spacing of data sampling. Since the sampling frequency was kept constant, in other words angle interval was constant, it gave smaller spacing between the data points at smaller radii. The smaller the interval between the points is, the larger the error in discretized vorticity becomes. But ω_ξ comes out as a nice even function of ξ there.

At $r=0.875R$ for both propellers, the vorticities show fairly complicated aspect, especially in η and ξ components. This is considered to be due to the strong influence of the tip vortex. In certain region on the blade near the tip, a part of the boundary layer is pulled laterally (radially) toward the tip vortex and enters the swirling flow just outside the tip vortex core. And it makes 'roll cake' type structure together with the vortex core. This phenomenon was observed more distinctly in the wake of a hydrofoil. (See Section 4.3)

Aerofoil theory tells us that the strength of the trailing vorticity is proportional to the slope of bound circulation on the blade. The area under ω_ξ has a dimension of circulation/length and corresponds to the slope of circulation. At each radius, the integration was done and thus obtained slopes are plotted in Figure 3-57 for the both propellers. From the analogy to an airplane wing, one might expect for these curves to decrease monotonically from inner radii to outer radii. However, in the case of these

propellers, there is a decrease of the value toward the hub. This trend is considered to be due to the presence of the hub.

In the same figure are also plotted the slopes (dr/dr) obtained by PUF-2 program. They are shown by a solid line and a dashed line. Agreement between the two (measured and computed) is good at mid-radius range. But near the propeller hub, PUF-2 overpredicts the slope. This is partially because PUF-2 neglects the hub. If the hub gives some 2-dimensional effect as does the water tunnel wall on a 2-D hydrofoil, the slope should tend to approach zero. The measured data implies that. Near the tip on the other hand, PUF-2 is underpredicting the slope.

Error in Vorticity The vorticity field was obtained by numerically differentiating the velocity. Differentiation usually enlarges the error (or noise) which is contained in the original signal. Aside the discretization error, the followings are the possible sources of error :

Error in positioning

Error in velocity reading.

Let us discuss how these come into the error of the vorticity. Take the radial component as an example. Discretized vorticity is written as

$$\omega_r = \frac{1}{r} \frac{v_{\theta,k+1} - v_{\theta,k-1}}{2\Delta\theta} - \frac{v_{\theta,i+1} - v_{\theta,i-1}}{2\Delta x}$$

Now suppose that each element contains an error, like

$$\Delta \theta = \Delta \theta^0 (1 + \epsilon_{\Delta \theta})$$

$$\Delta x = \Delta x^0 (1 + \epsilon_{\Delta x})$$

where superscript 0 represents true value and ϵ with subscript is the error. Expand the velocity components in terms of errors. We have

$$v_{x,k+1} = v_{x,k+1}^0 + \epsilon_{v_x}^+ v_{x,k+1}^0 + \frac{\partial v_{x,k+1}}{\partial \theta} \epsilon_{\Delta \theta}^+ \Delta \theta + \dots$$

$$v_{x,k-1} = v_{x,k-1}^0 + \epsilon_{v_x}^- v_{x,k-1}^0 + \frac{\partial v_{x,k-1}}{\partial \theta} \epsilon_{\Delta \theta}^- \Delta \theta + \dots$$

where the second term on the right of each equation is the reading error and the third is the positioning error. Other quantities can be expressed in the same way. The vorticity then becomes

$$\begin{aligned} \omega_r &= \frac{1}{2r\Delta\theta} \left[v_{x,k+1}^0 - v_{x,k-1}^0 + \epsilon_{v_x}^+ v_{x,k+1}^0 - \epsilon_{v_x}^- v_{x,k-1}^0 + \frac{\partial v_{x,k+1}}{\partial \theta} \epsilon_{\Delta \theta}^+ \Delta \theta - \frac{\partial v_{x,k-1}}{\partial \theta} \epsilon_{\Delta \theta}^- \Delta \theta \right] \\ &\quad - \frac{1}{2\Delta x} \left[v_{\theta,i+1}^0 - v_{\theta,i-1}^0 + \epsilon_{v_\theta}^+ v_{\theta,i+1}^0 - \epsilon_{v_\theta}^- v_{\theta,i-1}^0 + \frac{\partial v_{\theta,i+1}}{\partial x} \epsilon_{\Delta x}^+ \Delta x - \frac{\partial v_{\theta,i-1}}{\partial x} \epsilon_{\Delta x}^- \Delta x \right] \\ &= \omega_r^0 + \frac{v_{x,k}}{r\Delta\theta} \epsilon_{v_x} + \frac{1}{r} \frac{\partial v_{x,k}}{\partial \theta} \epsilon_{\Delta \theta} + \frac{v_{\theta,i}}{\Delta x} \epsilon_{v_\theta} + \frac{\partial v_{\theta,i}}{\partial x} \epsilon_{\Delta x} + \dots \end{aligned}$$

If we make rms error, we have

$$\text{rms error} = \frac{1}{|\omega_r^0|} \left[\left(\frac{U_{x,k}^0}{r \Delta \theta} \varepsilon_{v_x} \right)^2 + \left(\frac{1}{r} \frac{\partial U_{x,k}^0}{\partial \theta} \varepsilon_{\Delta \theta} \right)^2 + \left(\frac{U_{\theta,i}^0}{\Delta x} \varepsilon_{v_\theta} \right)^2 + \left(\frac{\partial U_{\theta,i}^0}{\partial x} \varepsilon_{\Delta x} \right)^2 \right]^{1/2}$$

What we need at this point is an estimate of error in each element. The error $\varepsilon_{\Delta x}$ is due to the positioning. That is about 10% with the current traverse system. $\varepsilon_{\Delta \theta}$ is mainly due to the error in the computer clock which is negligibly small. The error in velocity reading can be small also.

A rough estimation showed an error on the order of 10% which mainly comes from the positioning. The current positioning system is rather crude as mentioned in Chapter 2. A modification to the traverse and positioning system is being planned. It is expected that the error is reduced by this.

Fluctuation of the vorticity itself (so-called vortex wandering[17]) may also cause an error. This might be a matter of reproducibility rather than error, however.

4. Profile Drag of Propeller Blade Section

The velocity and vorticity data obtained from the experiments and shown in Chapter 3 will be used in the computation of propeller blade profile drag (viscous sectional drag). To do so, a formula for the drag coefficient has to be developed.

A handy formula for the profile drag of an aerofoil was first derived by Betz[8]. To get the force on a body in a flow, momentum theorem has to be used. To do so, one has to measure velocity and pressure all over the control surface which surrounds the body. Noticing the fact that the flow outside the aerofoil wake is practically inviscid irrotational, Betz introduced a hypothetical flow which is inviscid and irrotational and which has the same pressure as the real flow all over the control surface and the same velocity on the control surface except in the wake. Thus he eliminated the need of measuring the flow except in the wake. His formula is expressed in terms of pressures. This was adequate because what one measured then was pressure (total and static).

With the rapid development of Laser Doppler Anemometry, direct velocity measurement is now possible. Unlike the pressure probe such as Pitot tube, LDV does not disturb the flow. High frequency response of LDV is also suitable for measurements of rapidly changing flow such as propeller flow.

The author's intention here is to derive a formula which gives profile drag of propeller blade, and which is written in terms of velocities, thus suitable for LDV application.

In this chapter, a formula to give viscous drag on a solid body in a uniform flow is derived by extending and generalizing Betz's method. Then it is applied to hydrofoils and propellers.

4.1 Derivation of the Formula

Momentum Theorem The force and moment which act on a solid body in a flow are obtained by considering a momentum balance. Suppose there is a solid body moving in an incompressible fluid flow. Place a control volume V' (material volume) around the body at a particular time, t say.

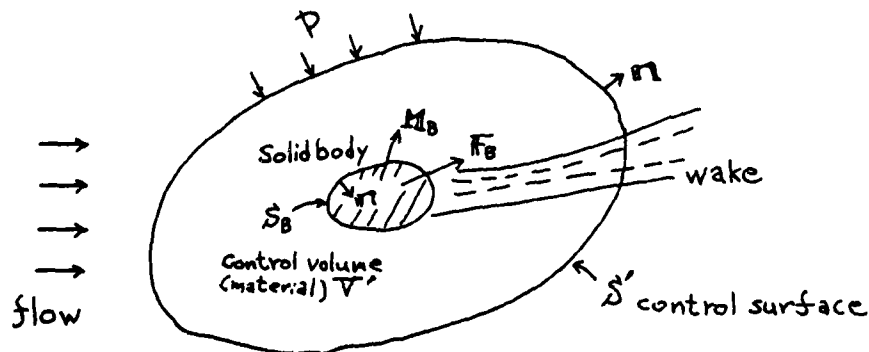


Figure 4-1 Formulation of the problem

Newton's second law of motion gives

$$\frac{d}{dt} \iiint_{V'} \rho \mathbf{v} dV = - \iint_{S'} p \mathbf{n} dS + \iiint_{V'} \rho \mathbf{g} dV - \mathbf{F}_B \quad (4-1)$$

$$\frac{d}{dt} \iiint_{V'} \mathbf{r} \times \rho \mathbf{v} dV = - \iint_{S'} \mathbf{r} \times p \mathbf{n} dS + \iiint_{V'} \mathbf{r} \times \rho \mathbf{g} dV - \mathbf{M}_B \quad (4-2)$$

where

ρ : density of the fluid

\mathbf{v} : velocity vector

S' : surface of control volume V'

S_B : surface of the body

p : static pressure

\mathbf{n} : normal unit vector on S' and S_B

pointing outward the control volume

\mathbf{g} : acceleration of gravity

\mathbf{r} : position vector

\mathbf{F}_B : the force which the body receives from the flow

\mathbf{M}_B : the moment " "

The fluid receives a reaction from the body as $-\mathbf{F}_B$ and $-\mathbf{M}_B$. Here, shearing stresses on the control surface S' due to viscosity of the fluid were neglected because they are considered to be small even in the wake of the body at most of the conditions in which we are interested in.

Since the flow measurement is done at points fixed in space, it is advantageous to use space fixed control volume. If use is made of transport theorem[18] on Equations (4-1) and (4-2), the material volume is replaced by space fixed volume. And if we rearrange them to get expressions for

force and moment, we have

$$F_B = - \iint_S (p v u_n + p n) dS + \iiint_V p g dV - \iiint_V p \frac{\partial v}{\partial t} dV - \iint_{S_B} p v u_n dS$$

and

$$M_B = - \iint_S r \times (p v u_n + p n) dS + \iiint_V r \times p g dV - \iiint_V r \times p \frac{\partial v}{\partial t} dV - \iint_{S_B} r \times p v u_n dS$$

where V and S are fixed in space.

For a solid body, surface integrals over S_B in both equations are zero since there is no net momentum transfer across S_B . Thus, we obtain

$$F_B = - \iint_S (p v u_n + p n) dS + \iiint_V p g dV - \iiint_V p \frac{\partial v}{\partial t} dV \quad (4-3)$$

$$M_B = - \iint_S r \times (p v u_n + p n) dS + \iiint_V r \times p g dV - \iiint_V r \times p \frac{\partial v}{\partial t} dV \quad (4-4)$$

These two equations are the ones which basically give the force and moment from measured velocity and pressure. However, these formulas are not so practical. The reason is obvious. Velocity and pressure have to be evaluated all over the control surface. And if the flow is unsteady, the acceleration term has to be evaluated everywhere in the volume. At this point, it is necessary to introduce hypothetical flow.

Introduction of Hypothetical flow The presence of the solid body introduces two different types of flows. Downstream the body, there is a strip of flow in which the influence of the body and of the viscosity of the fluid are not

negligible. This is called wake. Vorticity which is generated in the boundary layer on the body is convected downstream and forms the wake. Therefore, the wake is highly rotational. If one dimension of the body perpendicular to the flow is small, like a hydrofoil, the wake is usually confined to a narrow region. Outside the wake, the flow remains almost the same as is in the incoming flow. For example, if the inflow is uniform, then the outside flow is inviscid and irrotational. There, Bernoulli's theorem holds.

Betz extended inviscid irrotational flow into the wake of the aerofoil as hypothetical flow in order to use Bernoulli's theorem. However, in a 3-D flow such as that around a loaded airplane wing or propeller, Bernoulli's theorem may not hold because the flow in the wake is rotational due to trailing vortex. Therefore, the author does not claim that the hypothetical flow is irrotational. Even so, it is still advantageous to introduce inviscid hypothetical flow.

Let velocity \mathcal{V}^* and static pressure p^* be those in the hypothetical flow. This hypothetical flow is to be created by placing distribution of singularities such as sources and vortices in the incoming flow. As previously mentioned, the idea is to eliminate the need of measuring velocity and pressure all over the control surface. Therefore, it is necessary that the hypothetical flow has the same velocity and pressure distribution on S as the real flow at least in the inviscid flow region.

The requirements for the hypothetical flow are:

The hypothetical flow is inviscid flow.

On the control surface S , pressure p^* is everywhere identical to pressure p of the real flow and velocity v^* is identical to v everywhere except in the wake.

The two flows become different in the wake because one is viscous flow and the other is inviscid. This means that there is extra flux in the hypothetical flow.

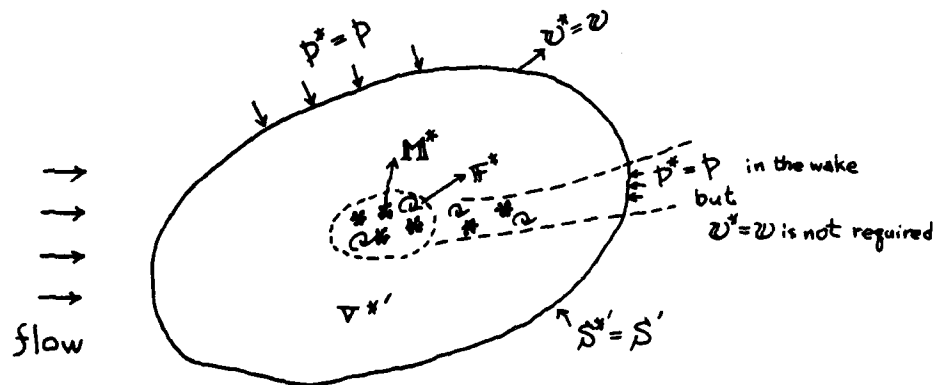


Figure 4-2 Hypothetical flow

The force and moment on the singularities due to the flow are obtained by again applying momentum balance argument,

$$\frac{d}{dt} \iiint_{V^*} \rho v^* dV = - \iint_{S^*} p^* n dS + \iiint_{V^*} \rho g dV - F^* \quad (4-5)$$

$$\frac{d}{dt} \iiint_{V^*} \mathbf{r} \times \rho v^* dV = - \iint_{S^*} \mathbf{r} \times p^* n dS + \iiint_{V^*} \mathbf{r} \times \rho g dV - \mathbf{M}^* \quad (4-6)$$

where F^* and M^* are the force and moment on the source and vortex distribution. $V^{*'} represents the control volume for the hypothetical flow, which is a little different from V' in that $V^{*'} does not have the solid body in it but the singularities instead. The outer surface of $V^{*}' is taken to be identical to S' here.$$$

It is necessary to bring Equations (4-5) and (4-6) into the same form as Equations (4-3) and (4-4). Since the velocity has singularities, care has to be taken in manipulating the integrals which involve velocity.

The hypothetical flow consists of 3 different types of flows; free stream U_∞ , flow from the sources w_s^* and flow due to vortices w_v^* .

$$w^* = U_\infty + w_s^* + w_v^* \quad (4-7)$$

For the vortex part of the flow, vortex core type representation is desired rather than vortex line. As will be mentioned later, the hypothetical flow is asked to simulate lifting problem of the body. This means that the vorticity pattern in the hypothetical flow which is related to the lifting problem has to be the same as that in the real flow. One possible place where this vorticity pattern is seen is the wake on the control surface S , where the trailing vortex passes through toward downstream. As Figure 3-11b shows, it is typically vortex core type flow, which makes sense since there is no vortex line (i.e. zero diameter) in the real flow. w_v^* then becomes continuous and

is not singular. The only singularity comes from ψ_s^* . Hence special care is needed when integrating ψ_s^* . The integral is of Cauchy type and is determined by first excluding an infinitesimal volume (usually sphere) which contains the source, and taking the limit of zero radius, like

$$\iiint_{V^*} \psi_s^* dV = \iiint_{x_s, y_s, z_s} \left[\lim_{V_\epsilon \rightarrow 0} \iiint_{V^* - V_\epsilon} \psi_s^*(x, y, z; x_s, y_s, z_s) dx dy dz \right] dx_s dy_s dz_s \quad (4-8)$$

Here, V_ϵ represents infinitesimal volume (sphere) surrounding the source at (x_s, y_s, z_s) .

Using this, the left side of (4-5) becomes

$$\begin{aligned} \frac{d}{dt} \iiint_{V^*} \rho \psi^* dV &= \rho \frac{d}{dt} \iiint_{V^*} (\psi_\infty + \psi_s^* + \psi_v^*) dV \\ &= \rho \frac{d}{dt} \iiint_{V^*} (\psi_\infty + \psi_v^*) dV + \rho \frac{d}{dt} \iiint_{V^*} \psi_s^* dV \\ &= \rho \iiint_{V^*} \frac{\partial}{\partial t} (\psi_\infty + \psi_v^*) dV + \rho \iint_S (\psi_\infty + \psi_v^*) \psi_n^* dS \\ &\quad + \rho \frac{d}{dt} \iiint_{x_s, y_s, z_s} \left[\lim_{V_\epsilon \rightarrow 0} \iiint_{V^* - V_\epsilon} \phi_s^* r r dS \right] dx_s dy_s dz_s \\ &= \rho \iiint_{V^*} \frac{\partial}{\partial t} (\psi_\infty + \psi_v^*) dV + \rho \iint_S (\psi_\infty + \psi_v^*) \psi_n^* dS \\ &\quad + \rho \frac{d}{dt} \iint_S \phi_s^* r r dS + \rho \frac{d}{dt} \iiint_{x_s, y_s, z_s} \left[\lim_{V_\epsilon \rightarrow 0} \iiint_{V^* - V_\epsilon} \phi_s^* r r dS \right] dx_s dy_s dz_s \end{aligned}$$

where ϕ_s^* is the velocity potential for the source distribution. The velocity potential does not exist for ψ_v^* . Here, the transport theorem and Gauss' theorem were used in the manipulation.

The third term on the right reduces to

$$\rho \frac{d}{dt} \iint_S \phi_s^* r r dS = \rho \iint_S \frac{\partial \phi_s^*}{\partial t} r r dS + \rho \iint_S \psi_s^* \psi_n^* dS$$

This relation is derived if we use space-fixed surface S in (4-5) and compare the result with that obtained by using material surface.

$$\begin{aligned} \text{Then, } \frac{d}{dt} \iiint_{V^*} \rho \psi^* dV &= \rho \iiint_{V^*} \frac{\partial}{\partial t} (\psi_\infty + \psi_v^*) dV + \rho \iint_S \psi^* \psi_n^* dS \\ &+ \rho \iint_S \frac{\partial \phi_s^*}{\partial t} r n dS + \rho \frac{d}{dt} \iiint_{\substack{z_s, y_s, x_s \\ \epsilon \rightarrow 0}} \left[\lim_{\epsilon \rightarrow 0} \iint_{S_\epsilon} \phi_s^* r n dS \right] dx_s dy_s dz_s \end{aligned}$$

Finally, Equation (4-5) reduces to

$$\begin{aligned} H^* &= - \iint_S (\rho \psi^* \psi_n^* + p^* r n) dS + \rho \iiint_{V^*} g dV - \rho \iiint_{V^*} \frac{\partial}{\partial t} (\psi_\infty + \psi_v^*) dV \\ &- \rho \iint_S \frac{\partial \phi_s^*}{\partial t} r n dS - \rho \frac{d}{dt} \iiint_{\substack{z_s, y_s, x_s \\ \epsilon \rightarrow 0}} \left[\lim_{\epsilon \rightarrow 0} \iint_{S_\epsilon} \phi_s^* r n dS \right] dx_s dy_s dz_s \quad (4-9) \end{aligned}$$

The moment (Equation (4-6)) can be handled in a similar way.

$$\begin{aligned} \frac{d}{dt} \iiint_{V^*} (\mathbf{r} \times \rho \psi^*) dV &= \rho \frac{d}{dt} \iiint_{V^*} \mathbf{r} \times (\psi_\infty + \psi_s^* + \psi_v^*) dV \\ &= \rho \frac{d}{dt} \left[\iiint_{V^*} \mathbf{r} \times (\psi_\infty + \psi_v^*) dV + \iiint_{V^*} \mathbf{r} \times \nabla \phi_s^* dV \right] \end{aligned}$$

But

$$\mathbf{r} \times \nabla \phi_s^* = - \nabla \times (\mathbf{r} \phi_s^*)$$

and

$$\begin{aligned} - \iiint_{V^*} \nabla \times (\mathbf{r} \phi_s^*) dV &= \iiint_{\substack{z_s, y_s, x_s \\ \epsilon \rightarrow 0}} \left[\lim_{\epsilon \rightarrow 0} \iint_{S_\epsilon} \phi_s^* (\mathbf{r} \times \mathbf{n}) dS \right] dx_s dy_s dz_s \\ &= \iint_S \phi_s^* (\mathbf{r} \times \mathbf{n}) dS + \iiint_{\substack{z_s, y_s, x_s \\ \epsilon \rightarrow 0}} \left[\lim_{\epsilon \rightarrow 0} \iint_{S_\epsilon} \phi_s^* (\mathbf{r} \times \mathbf{n}) dS \right] dx_s dy_s dz_s \end{aligned}$$

can be shown by vector calculus. And if we use the relation

$$\rho \frac{d}{dt} \iint_{S'} \phi_s^* (\mathbf{r} \times \mathbf{n}) dS = \rho \iint_S \frac{\partial \phi_s^*}{\partial t} (\mathbf{r} \times \mathbf{n}) dS + \rho \iint_S (\mathbf{r} \times \psi_s^*) \psi_n^* dS$$

which is obtained again by comparing the formulas for angular momentum with 2 different types of control surfaces,

one moving with the fluid, the other fixed in space. Then, we get

$$\begin{aligned} \frac{d}{dt} \iiint_{V^*} (\mathbf{r} \times \rho \mathbf{v}^*) dV &= \rho \iiint_{V^*} \mathbf{r} \times \frac{\partial}{\partial t} (\mathbf{u}_\infty + \mathbf{v}_r^*) dV + \rho \iint_S \mathbf{r} \times (\mathbf{u}_\infty + \mathbf{v}_r) \mathbf{v}_n^* dS \\ &+ \rho \iint_S \frac{\partial \phi^*}{\partial t} (\mathbf{r} \times \mathbf{n}) dS + \rho \iint_S \mathbf{r} \times \mathbf{w}_s^* \mathbf{v}_n^* dS \\ &+ \rho \frac{d}{dt} \iiint_{\substack{x,y,z \\ \lim_{\epsilon \rightarrow 0} S_\epsilon}} [\phi_s^* (\mathbf{r} \times \mathbf{n}) dS] dx_s dy_s dz_s \end{aligned}$$

We end up with

$$\begin{aligned} \mathbf{M}^* &= - \iint_S \mathbf{r} \times (\rho \mathbf{v}^* \mathbf{v}_n^* + p^* \mathbf{n}) dS + \rho \iiint_{V^*} \mathbf{r} \times \mathbf{g} dV - \rho \iiint_{V^*} \mathbf{r} \times \frac{\partial}{\partial t} (\mathbf{u}_\infty + \mathbf{v}_r^*) dV \\ &- \rho \iint_S \frac{\partial \phi^*}{\partial t} (\mathbf{r} \times \mathbf{n}) dS - \rho \frac{d}{dt} \iiint_{\substack{x,y,z \\ \lim_{\epsilon \rightarrow 0} S_\epsilon}} [\phi_s^* (\mathbf{r} \times \mathbf{n}) dS] dx_s dy_s dz_s \quad (4-10) \end{aligned}$$

Decomposition of Force and Moment The forces and moments are decomposed as follows.

For the real flow, we have

$$\mathbf{F}_B = \mathbf{F}_{BL} + \mathbf{F}_{BD} + \mathbf{F}_{Buoy} \quad (4-11)$$

$$\mathbf{M}_B = \mathbf{M}_{BL} + \mathbf{M}_{BD} + \mathbf{M}_{Buoy} \quad (4-12)$$

where \mathbf{F}_{BL} is the lifting force produced by inflow + induced velocity, \mathbf{F}_{BD} is the drag force and \mathbf{F}_{Buoy} is the buoyancy force. These notions also apply to moment. Note that 'lift' here means the force which circulation distribution around the body produces against inflow and induced velocity. Consequently, this includes so-called induced drag. This convention is the same in the hypothetical flow. The force which the source distribution receives is not

called 'lift' in this paper even though the force may happen to be parallel to the lift.

It is clear that

$$F_{\text{buoy}} = - \iiint_{V_B} \rho g dV \quad (4-13)$$

$$M_{\text{buoy}} = - \iiint_{V_B} \mathbf{r} \times \rho g dV \quad (4-14)$$

For the hypothetical flow we can write

$$F^* = F_L^* + F_D^* \quad (4-15)$$

$$M^* = M_L^* + M_D^* \quad (4-16)$$

where F_L^* is the lifting force and F_D^* is the drag. There is no buoyancy force in the hypothetical flow.

Since we are interested in the drag, it would be most convenient if $F_L^* = F_L$ and $M_L^* = M_L$ were true. One necessary condition for this is that the vorticity distribution in the hypothetical flow is equal to that which contributes to lift in the real flow. This will be discussed later with each specific case.

Subtracting Equations (4-9) and (4-10) from (4-3) and (4-4) respectively and taking into account the relations (4-11) - (4-16), we have

$$\begin{aligned} & F_R + F_B - F_L^* - F_D^* \\ &= -\rho \iint_{S_w} (v v_n - v^* v_n^*) dS - \rho \iiint_V \frac{\partial \psi}{\partial t} dV + \rho \iiint_{V^*} \frac{\partial}{\partial t} (\psi_0 + \psi^*) dV \\ &+ \rho \iint_S \frac{\partial \phi^*}{\partial t} n dS + \rho \frac{d}{dt} \iiint_{\lim_{z_i, x_i, y_i \rightarrow 0} S_i} \phi^* n dS \end{aligned} \quad (4-17)$$

and

$$\begin{aligned}
 M_{BL} + M_{BD} - M_L^* - M_D^* \\
 = -\rho \iint_{S_w} \mathbf{r} \times (\mathbf{v} v_n - \mathbf{v}^* v_n^*) dS - \rho \iiint_V \mathbf{r} \times \frac{\partial \mathbf{v}}{\partial t} dV + \rho \iiint_{V^*} \mathbf{r} \times \frac{\partial}{\partial t} (\mathbf{v}_0 + \mathbf{v}^*) dV \\
 + \rho \iint_S \frac{\partial \Phi^*}{\partial t} (\mathbf{r} \times \mathbf{n}) dS + \rho \frac{d}{dt} \iiint_{\substack{Z, Y, X, \\ \lim_{t \rightarrow 0} S_\epsilon}} \left[\iint_{S_\epsilon} \Phi_s^* (\mathbf{r} \times \mathbf{n}) dS \right] dX, dY, dZ_s \quad (4-18)
 \end{aligned}$$

where S_w represents the part of the control surface S which is in the wake of the body.

The Force and Moment computed in Hypothetical Flow The net flux from the sources is not zero because velocity \mathbf{v}^* is different from \mathbf{v} in the wake. The real flow satisfies the continuity equation. The net flux produces a non-zero force on the sources (Lagally force). If we write the flux Q in terms of source strength, $q(x_s, y_s, z_s)$, we have

$$\begin{aligned}
 Q &= \iiint_{\substack{Z, Y, X, \\ \lim_{t \rightarrow 0} S_\epsilon}} q(x_s, y_s, z_s) dX, dY, dZ_s \\
 (\text{or, } &= \iiint_{V_s} q(\mathbf{v}_s) dV_s) \quad (4-19)
 \end{aligned}$$

If the sources are moving and also changing their intensity in time, q becomes a function of time. But in this paper, let us just assume no time variation of intensity and no relative motion between the sources (or source elements), which are suitable assumptions for the hypothetical flow simulating that around a solid body in a uniform stream. The integral (4-19) then becomes time independent.

The flux is also expressed by the velocity on S as

$$Q = \iint_{S_w} (\mathbf{v}^* - \mathbf{v}) \cdot \mathbf{n} dS \quad (4-20)$$

Lagally's theorem for the force on singularities gives

$$\mathbb{F}_D^* = -\rho \iiint_{V_S} (\mathbf{U}_\infty + \mathbf{v}_i) \delta dV_S - \rho \frac{d}{dt} \iiint_{V_S} \left[\lim_{\epsilon \rightarrow 0} \iint_{S_\epsilon} \phi_s^* \mathbf{r} dS \right] dV_S \quad (4-21)$$

and

$$\mathbb{M}_D^* = -\rho \iiint_{V_S} \mathbf{r}_s \times (\mathbf{U}_\infty + \mathbf{v}_i) \delta dV_S - \rho \frac{d}{dt} \iiint_{V_S} \left[\lim_{\epsilon \rightarrow 0} \iint_{S_\epsilon} \phi_s^* (\mathbf{r} \times \mathbf{r}) dS \right] dV_S \quad (4-22)$$

where \mathbf{U}_∞ is incoming flow and \mathbf{v}_i is velocity induced by other singularities (vortices) and by sources if any at outside S. \mathbf{r}_s is the position vector of the source. The second term on the right of each equation is due to the motion of the sources. The forces which act between the sources inside S cancel out and do not remain in the total force.

Substituting Equations (4-21) and (4-22) into (4-17) and (4-18), we get

$$\begin{aligned} \mathbb{F}_{BL} + \mathbb{F}_{BD} - \mathbb{F}_L^* = & -\rho \iint_{S_w} (\mathbf{v} \mathbf{U}_\infty - \mathbf{v}^* \mathbf{U}_\infty^*) dS - \rho \iiint_V \frac{\partial \mathbf{v}}{\partial t} dV + \rho \iiint_{V^*} \frac{\partial}{\partial t} (\mathbf{U}_\infty + \mathbf{v}_v^*) dV \\ & + \rho \iint_S \frac{\partial \phi_s^*}{\partial t} \mathbf{r} dS - \rho \iiint_{V_S} (\mathbf{U}_\infty + \mathbf{v}_i) \delta dV_S \end{aligned} \quad (4-23)$$

and

$$\begin{aligned} \mathbb{M}_{BL} + \mathbb{M}_{BD} - \mathbb{M}_L^* = & -\rho \iint_{S_w} \mathbf{r} \times (\mathbf{v} \mathbf{U}_\infty - \mathbf{v}^* \mathbf{U}_\infty^*) dS - \rho \iiint_V \mathbf{r} \times \frac{\partial \mathbf{v}}{\partial t} dV \\ & + \rho \iiint_{V^*} \mathbf{r} \times \frac{\partial}{\partial t} (\mathbf{U}_\infty + \mathbf{v}_v^*) dV + \rho \iint_S \frac{\partial \phi_s^*}{\partial t} (\mathbf{r} \times \mathbf{r}) dS \\ & - \rho \iiint_{V_S} \mathbf{r}_s \times (\mathbf{U}_\infty + \mathbf{v}_i) \delta dV_S \end{aligned} \quad (4-24)$$

Construction of Hypothetical Flow Different from Betz's method where measured pressure automatically gives the hypothetical flow, it is necessary to construct the hypothetical velocity in the present method.

As mentioned in the previous section, most convenient is that the hypothetical flow gives the same lift as the real flow. This requires that the trailing vorticity be identical in both flows. Hence there is a possibility that we are able to get the hypothetical flow by measuring the trailing vorticity and using Biot-Savart's law. However, it may be tedious and time consuming to do so.

The author has come up with an idea to use Navier-Stokes equation provided that the real flow is satisfying it. The equation is written in a form with vorticity expressed explicitly,

$$\frac{\partial \mathbf{v}}{\partial t} + \nabla \left(\frac{1}{2} |\mathbf{v}|^2 + \frac{p}{\rho} + G \right) = \mathbf{v} \times \boldsymbol{\omega} \quad (4-25)$$

where G is potential of gravity. Here, the viscosity term $\nabla^2 \mathbf{v}$ was neglected, because it is presumed to be small. This is consistent with the assumption stated in Equations (4-1) and (4-2). This approximation makes the equation appear to be identical to Euler's Equation. However, note that the vorticity has difference as will be mentioned later.

The hypothetical flow is supposed to be inviscid and to satisfy Euler's equation,

$$\frac{\partial \psi^*}{\partial t} + \nabla \left(\frac{1}{2} |\psi^*|^2 + \frac{p^*}{\rho} + G \right) = \psi^* \times \omega^* \quad (4-26)$$

Now, the real flow in the wake is considered to have two types of vorticity. One is boundary layer type vorticity, which originates in the boundary layers on the body surface. The other is trailing vorticity which can be modeled by inviscid flow.

Write

$$\omega = \omega_r + \omega_b \quad (4-27)$$

where ω_r = vorticity which constructs trailing vortex system, hence contributes to circulation and hence to the lift,

ω_b = vorticity other than ω_r ,
originating in the boundary layers
on the blade.

The vorticity in the hypothetical flow is just trailing vorticity. There are no vorticity which originates in the boundary layers.

$$\omega^* = \omega_r \quad (4-28)$$

Subtracting Equation (4-25) from Equation (4-26), we obtain

$$\frac{\partial \psi^*}{\partial t} - \frac{\partial \psi}{\partial t} + \nabla \left(\frac{1}{2} |\psi^*|^2 - \frac{1}{2} |\psi|^2 \right) = (\psi^* - \psi) \times \omega_r - \psi \times \omega_b \quad (4-29)$$

This is now a differential equation to give ψ^* , the boundary condition being $\psi^* = \psi$ on the edges of the wake.

It is not advantageous to solve this in an ordinary way for three unknowns of the velocity components. By making an assumption, things can be greatly simplified.

That is :

The difference of the two velocities is parallel to the trailing vortex,

or
$$\mathbf{v}^* - \mathbf{v} \parallel \boldsymbol{\omega}_r .$$

This assumption is essentially the same as Betz made in his hypothetical flow, and is necessary to maintain the same lift.

Equation (4-29) then reduces to

$$\frac{\partial \mathbf{v}^*}{\partial t} + \nabla \left(\frac{1}{2} |\mathbf{v}^*|^2 \right) = \frac{\partial \mathbf{v}}{\partial t} + \nabla \left(\frac{1}{2} |\mathbf{v}|^2 \right) - \mathbf{v} \times \boldsymbol{\omega}_s \quad (4-30)$$

4.2 Application to 2-D Hydrofoil

Formula To check the validity of the method described above, experiments were conducted first with 2-D hydrofoils so that the results could be compared with other data.

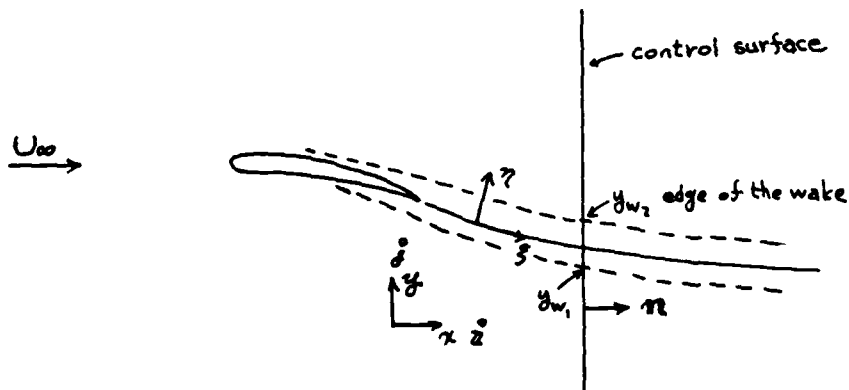


Figure 4-3 2-D Hydrofoil *

For a steady 2-D hydrofoil or aerofoil, in a uniform

flow of unbounded fluid, Equation (4-23) reduces to

$$F_{BL} + F_{BD} - F_L^* = -\rho \iint_{S_w} (w v_n - w^* v_n^*) dS - \rho \iiint_{V_S} (U_\infty + w_i) g dV,$$

where w_i is the induced velocity due to vorticity distribution (foil) in the hypothetical flow. Since the vorticity distribution in the hypothetical flow is intended to be identical to that which contributes to lift in the real flow, F_L^* contains the same force as F_{BL} . Besides, it has the lift due to the induced velocity from the extra source distribution. But this lift exactly cancels out with the last term on right side as internal force, even if there are extra sources, provided that those extra sources are inside the control surface S . Therefore, we have

$$F_{BD} = -\rho \iint_{S_w} (w v_n - w^* v_n^*) dS - \rho \iiint_{V_S} U_\infty g dV,$$

For unit length of span (or for 2-D foil), the surface integrals reduce to line integrals. Also, making use of the relation (4-19) and (4-20), we have

$$F_{BD} = -\rho \int_{S_w} (w v_n - w^* v_n^*) dS - \rho U_\infty \int_{S_w} (w^* - w) \cdot n dS$$

The drag acts parallel to x-axis. Taking x-component, we have

$$F_{BDx} = -\rho \int_{S_w} (u_x v_n - v_x^* v_n^*) dS - \rho U_\infty \int_{S_w} (w^* - w) \cdot n_x dS$$

*) Note that the coordinate system is defined differently from the propeller case.

If we take $x=\text{const.}$ line as a part of the control surface(line) downstream the foil, we have

$$\eta = \bar{a}, \quad v_n = v_x, \quad v_n^* = v_x^*.$$

Hence,

$$\begin{aligned} F_{B0x} &= -\rho \int_{y_{w1}}^{y_{w2}} (v_x^2 - v_x^{*2}) dy - \rho U_\infty \int_{y_{w1}}^{y_{w2}} (v_x^* - v_x) dy \\ &= \rho \int_{y_{w1}}^{y_{w2}} (v_x^* - v_x)(v_x^* + v_x - U_\infty) dy \end{aligned} \quad (4-31)$$

The drag coefficient C_d is given by

$$\begin{aligned} C_d &= \frac{F_{B0x}}{\frac{1}{2} \rho U_\infty^2 c} \\ &= 2 \int_{y_{w1}}^{y_{w2}} \left(\frac{v_x^*}{U_\infty} - \frac{v_x}{U_\infty} \right) \left(\frac{v_x^*}{U_\infty} + \frac{v_x}{U_\infty} - 1 \right) d\left(\frac{y}{c}\right) \end{aligned} \quad (4-32)$$

Construction of Hypothetical Flow Equation (4-30) becomes

$$\left(i \frac{\partial}{\partial x} + j \frac{\partial}{\partial y} \right) \left[\frac{1}{2} (v_x^{*2} + v_y^{*2}) \right] = \left(i \frac{\partial}{\partial x} + j \frac{\partial}{\partial y} \right) \left[\frac{1}{2} (v_x^2 + v_y^2) \right] - (v_y \omega_z \bar{a} - v_x \omega_z \bar{b})$$

In 2-D steady flow, there should be no trailing or shed vorticity in the wake. All that is there is the boundary layer type vorticity in the viscous wake. Therefore, there is no need to discriminate one type from the other.

Taking y -component, we have

$$\frac{\partial}{\partial y} \left[\frac{1}{2} (v_x^{*2} + v_y^{*2}) \right] = \frac{\partial}{\partial y} \left[\frac{1}{2} (v_x^2 + v_y^2) \right] + v_x \omega_z$$

Integrating with y ,

$$v_x^{*2} + v_y^{*2} = v_x^2 + v_y^2 + 2 \int_{y_{w1}}^y v_x \omega_z dy$$

where y_{w1} is one of the edges of the wake. The integration

should be only in the wake of the foil, since the vorticity is zero outside it.

Transform the coordinates from x, y to ξ, η in which ξ -axis is parallel to the streamline at the center of the wake. Since there is no relative motion between the two systems, the absolute velocity does not change through the transformation, giving

$$v_x^2 + v_y^2 = v_\xi^2 + v_\eta^2$$

The equation then becomes

$$v_\xi^{*2} + v_\eta^{*2} = v_\xi^2 + v_\eta^2 + 2 \int_{y_1}^y v_x \omega_z dy$$

The equation still has two unknowns v_ξ^* and v_η^* . To solve this, we need one assumption. The assumption stated before should be applied.

In this particular case, it comes as

$$v_\eta^* = v_\eta$$

This is explained from the following reasoning.

The trajectory of the wake near the trailing edge is bent due to the presence of lift (bound circulation). To keep the same lift, the geometry of it has to be the same. This means that the difference in the velocity between the two types of flow is permitted only in v_ξ^* , in other words, $v_\eta^* = v_\eta$ has to be maintained.

The equation simplifies to

$$v_\xi^{*2} = v_\xi^2 + 2 \int_{y_1}^y v_x \omega_z dy \quad (4-33)$$

Since the right side is known (given from the experiment), v_f^* is determined. Through the inverse transformation, v_x^* and v_y^* are now given.

To reduce possible numerical errors, a further step should be taken.

Since

$$\omega_z = \frac{\partial v_y}{\partial x} - \frac{\partial v_x}{\partial y},$$

the integral on the right becomes

$$\begin{aligned} 2 \int_{y_{w_1}}^y v_x \omega_z dy &= 2 \int_{y_{w_1}}^y v_x \left(\frac{\partial v_y}{\partial x} - \frac{\partial v_x}{\partial y} \right) dy \\ &= 2 \int_{y_{w_1}}^y v_x \frac{\partial v_y}{\partial x} dy - \int_{y_{w_1}}^y \frac{\partial}{\partial y} (v_x^2) dy \\ &= 2 \int_{y_{w_1}}^y v_x \frac{\partial v_y}{\partial x} dy - (v_x^2 - v_x^2|_{y_{w_1}}) \end{aligned}$$

and

$$v_f^{*2} = v_f^2 + 2 \int_{y_{w_1}}^y v_x \frac{\partial v_y}{\partial x} dy - v_x^2 + v_x^2|_{y_{w_1}} \quad (4-34)$$

Experimental Results Wake surveys were conducted in the MIT Water Tunnel using two hydrofoils :

A) NACA 0012 Basic Thickness form

and

B) NACA 66-309 $a=0.8$ with modified L.E. *)

Both foils have the dimensions of 9"(chord) x 20"(span) and completely span the water tunnel. The experimental conditions are shown in Table 4-1 below.

* The wake survey for Foil B was done by Moas[19].

Table 4-1 Experimental Conditions

	Angle of attack	Reynolds No.
Foil A	0	1×10^6
Foil B	4.5 deg.	9×10^5 and 2×10^6

The wake surveys were done by traversing the laser along midchord plane at several $x=\text{const.}$ lines. Figures 4-4 through 4-6 show measured and hypothetical velocities (x-component) and vorticity distribution computed from the velocity data. Figure 4-7 show the values of the profile drag obtained at various measurement points in x direction. Ideally, C_d value should be independent of the measurement point, unless large dissipation takes place. In fact, the results shown here give fairly constant C_d along x.

For the NACA 0012 foil, C_d at zero degree of angle of attack is somewhere between 0.006 and 0.01 from reference [20]. The values measured by the LDV are considered to be fairly reasonable.

For the NACA 66-309 foil, the author has not found the curves for C_d . However, extrapolating from the chart for NACA 66-209, the angle of attack 4.5 degree gives $C_l=0.6$. Then the corresponding C_d is somewhere between 0.008 and 0.011, to which are comparable the values obtained by the LDV.

The above examples have well demonstrated the validity of the present method.

4.3 3-D Hydrofoil

Wake survey was also done with a 3-D (i.e. finite span) hydrofoil. SNAME Keel Model No.3 was attached to the side window of the water tunnel and the velocity distribution behind the foil was measured. The characteristics of the foil and the conditions of the experiment are listed in Table 4-2.

Table 4-2 Dimensions of the Model
and Experimental Conditions

Identification	SNAME Keel Model No.3
Span (or Height)	7.320"
Chord length	8.000"
Sweep angle	40deg
Section	NACA 63-010
Angle of attack	4deg
Reynolds No. (chord)	1×10^6

The measurement points were taken at $z = -5.0$, -1.0 and -0.5 inches at $x = -0.4$ ", the origin of the coordinates being at the trailing edge of the tip. Along the line parallel to y-axis the velocity was measured. (See Figure 4-8 for the definition of the coordinate system.) Also the velocity was measured across the tip vortex core center, traversing the LDV parallel to y-axis and also parallel to z-axis.

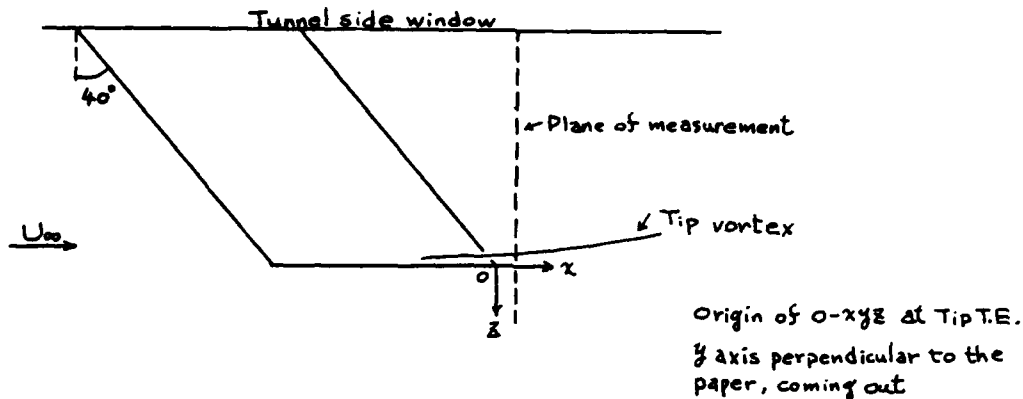


Figure 4-8 3-D Hydrofoil and the Coordinate System

Figures 4-9 to 4-12 show thus obtained velocity distributions. At $z=-0.5"$ (Fig.4-9), the velocity defect is shallower than others. This is because this measurement point is further than other points from T.E. due to the sweep of the foil.

It is interesting to see that the velocity distribution across the tip vortex core shows double dents (Figure 4-12). This also appears in figure 4-13 which corresponds to the traverse parallel to z -axis. These two figures are revealing that a part of the boundary layer on the blade is 'sucked in' the tip vortex and swirl around the vortex core, which was also observed in the propeller flow. If we follow the swirling path of the velocity defect, on these figures (4-12 and 4-13), we see that the defect becomes shallower and wider as it turns.

The profile drag was computed at each point using the measured velocity defect.* The spanwise distribution of the drag (coefficient) is shown in Figure 4-14. At the mid-span

range, C_d is constant. Near the tip, it decreases once and then in the tip vortex, it becomes larger. The drag coefficient obtained at the tip vortex may not be so accurate, because the drag is calculated as sectional drag (in other words, 2-dimensionally) there. To obtain more accurate value, the momentum defect has to be taken for the whole tip vortex area. However, there should be no doubt about the fact that tip vortex region contains considerable amount of momentum loss - drag. Even at zero lift (i.e. without tip vortex), it was shown that the sectional drag decreases toward the tip and then increases. This 'tip effect' could give substantial amount of difference to the drag value from 2-D case [21].

4.4 Application to Propeller

Formula To manipulate Equations (4-23) and (4-24) we need to be more specific about the control volume and the singularity distribution.

As a control volume, choose a circular cylinder of radius R_c whose axis (center line) lies on x-axis. Name the three surfaces which surround the control volume as S_1 , S_2 and S_3 as shown in Figure 4-15. The radius R_c is to be taken large enough so that the propeller is inside this

*) The formula for the profile drag of a 2-D hydrofoil can be also applied to a finite span foil if we assume

- i) Induced velocity is perpendicular to the inflow
- ii) Streamline in the wake is parallel to x-y plane.

control volume.

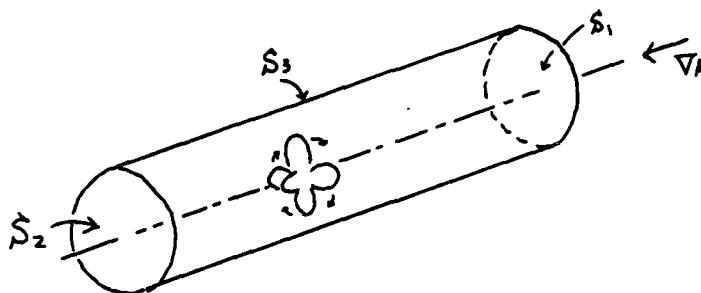


Figure 4-15 Control volume

For the case of constant speed rotation of the propeller in a uniform stream, more modifications are possible on some of the terms in Equations (4-23) and (4-24).

If we write $w(x, r, \theta, t) = w'(x, r, \theta', t) + r\Omega \mathcal{C}_\theta$

then

$$\begin{aligned} \frac{\partial w}{\partial t} &= \frac{\partial}{\partial t} w'(x, r, \theta, t) \Big|_{t=t} + \frac{\partial w}{\partial \theta'} \frac{\partial \theta'}{\partial t} \\ &= \frac{\partial w'}{\partial t} \Big|_{t=t} - \Omega \frac{\partial w'}{\partial \theta'} \end{aligned}$$

From blade fixed frame of reference, the flow looks steady.

This gives $\frac{\partial w'}{\partial t} \Big|_{t=t} = 0$.

Hence

$$\frac{\partial w}{\partial t} = -\Omega \frac{\partial w'}{\partial \theta'} \quad (4-35)$$

The second term on right side of Equation (4-23) becomes

$$\begin{aligned} \rho \iiint_V \frac{\partial w}{\partial t} dV &= -\rho \Omega \iiint_V \frac{\partial w'}{\partial \theta'} r d\theta' dr d\alpha \\ &= -\rho \Omega \int_{\alpha=0}^{2\pi} \int_{r=0}^{\infty} [w']_{\theta'=0}^{\theta'=2\pi} r dr d\alpha \end{aligned}$$

But

$$[w']_{\theta'=0}^{\theta'=2\pi} = w'_{/2\pi} - w'_{/0} = 0$$

due to periodicity if no blade is in the way of integration path. Or, if the blades are in the way, it becomes

$$\begin{aligned} [v']_{\theta'=0}^{2\pi} &= [v']_{\theta'=0}^{\theta_1} + [v']_{\theta_1+\Delta\theta_c}^{\theta_1+\frac{2\pi}{K}} + \dots \\ &= 0 - v'_{\theta'=0} + 0 - 0 + v'_{\theta'=2\pi} - 0 \\ &= -v'_{\theta'=0} + v'_{\theta'=2\pi} \\ &= 0 \end{aligned}$$

where θ_1 designates the angular location of the surface of one of the blades, $\Delta\theta_c$ is the thickness of the blade in angle in θ' direction at radius r and K is the number of blades. This result is obtained from the no-slip condition on the blade surface and from periodicity. Hence the integral is zero in any case.

The first case applies to $\rho \iiint_{V^*} \frac{\partial v^*}{\partial t} dV$ and this integral becomes zero. ($\frac{\partial u_\infty}{\partial t}$ is zero because the inflow is uniform.)

$$\rho \iiint_{V^*} \frac{\partial v^*}{\partial t} dV = -\rho \Omega \iint_{x,r} [v^*]_{\theta'=0}^{2\pi} r dr dx = 0$$

Similarly,

$$\begin{aligned} \rho \iiint_V r \times \frac{\partial v}{\partial t} dV &= -\rho \Omega \iiint_V \frac{\partial}{\partial \theta} (r \times v') dV \\ &= -\rho \Omega \iint_{x,r} [r \times v']_{\theta'=0}^{2\pi} r dr dx = 0 \end{aligned}$$

and

$$\rho \iiint_{V^*} r \times \frac{\partial v^*}{\partial t} dV = 0$$

Now, let us discuss the fourth term, $\rho \iint_S \frac{\partial \phi^*}{\partial t} n dS$ on the

right of Equation (4-23). The integrand takes different forms depending on the surface along which the integration is to be done, since the normal unit vector becomes different.

On S_1 , the normal unit vector is

$$\mathbf{n} = \hat{\mathbf{z}}$$

on S_2 , it is

$$\mathbf{n} = -\hat{\mathbf{z}}$$

and on S_3 , it becomes

$$\mathbf{n} = \mathbf{e}_r = \cos\theta' \hat{\mathbf{j}}' + \sin\theta' \hat{\mathbf{k}}'$$

To see if the integral vanishes (which is the most convenient for us), we need a more specific expression for ϕ_s^* . The velocity potential for the source distribution which corresponds to K-bladed propeller is given by

$$\phi_s^* = \sum_{k=1}^K \iiint_{x, r, \theta} \frac{1}{4\pi} \frac{q(x_s, r_s, \theta_s')}{[(x-x_s)^2 + r^2 + r_s^2 - 2rr_s \cos(\theta' - \theta_s' - \frac{2\pi k}{K})]^{3/2}} r_s d\theta_s' dr_s dx_s \quad (4-36)$$

where (x_s, r_s, θ_s') is the location of the source element and $q(x_s, r_s, \theta_s')$ is the intensity. The integral is over the volume of the source for one blade. Note that this is the potential in the fixed frame of reference, $xr\theta$, although expressed in terms of $xr\theta'$.

Then,

$$\begin{aligned} \frac{\partial \phi_s^*}{\partial t} &= -\Omega \frac{\partial \phi_s^*}{\partial \theta'} \\ &= \frac{\Omega}{4\pi} \sum_{k=1}^K \iiint_{x, r, \theta} \frac{r r_s^2 \sin(\theta' - \theta_s' - \frac{2\pi k}{K}) q(x_s, r_s, \theta_s')}{[(x-x_s)^2 + r^2 + r_s^2 - 2rr_s \cos(\theta' - \theta_s' - \frac{2\pi k}{K})]^{3/2}} d\theta_s' dr_s dx_s \end{aligned}$$

If we expand the denominator, we have

$$\frac{1}{[(x-x_s)^2 + r^2 + r_s^2 - 2rr_s \cos(\theta' - \theta'_s - \frac{2\pi R}{K})]^{3/2}}$$

$$= \frac{1}{[(x-x_s)^2 + r^2 + r_s^2]^{3/2}} \left[1 + \frac{3}{2} a \cos(\theta' - \theta'_s - \frac{2\pi R}{K}) + \frac{15}{4} a^2 \cos^2(\theta' - \theta'_s - \frac{2\pi R}{K}) + \dots \right]$$

where $a \equiv \frac{2rr_s}{(x-x_s)^2 + r^2 + r_s^2}$, was used for convenience.

And, if we use the following formula,

$$\cos^n \varphi = \begin{cases} \frac{1}{2^{n-1}} \sum_{l=0}^{n-1} \binom{n}{l} \cos(n-2l) \varphi + \frac{1}{2^n} \binom{n}{n/2} & n: \text{even} \\ \frac{1}{2^{n-1}} \sum_{l=0}^{n-1} \binom{n}{l} \cos(n-2l) \varphi & n: \text{odd} \end{cases}$$

we obtain

$$\frac{rr_s^2 \sin(\theta' - \theta'_s - \frac{2\pi R}{K}) g(x_s, r_s, \theta'_s)}{[(x-x_s)^2 + r^2 + r_s^2 - 2rr_s \cos(\theta' - \theta'_s - \frac{2\pi R}{K})]^{3/2}}$$

$$= \frac{g rr_s^2 \sin(\theta' - \theta'_s - \frac{2\pi R}{K})}{[(x-x_s)^2 + r^2 + r_s^2]^{3/2}} \left[C_0 + \sum_{n=1}^{\infty} \sum_l C_{n,l} \cos(n-2l)(\theta' - \theta'_s - \frac{2\pi R}{K}) \right]$$

Then,

$$\frac{\partial \Phi_s}{\partial t} = \frac{Q}{4\pi} \left(\sum_{R=1}^K \frac{g rr_s^2 \sin(\theta' - \theta'_s - \frac{2\pi R}{K})}{[(x-x_s)^2 + r^2 + r_s^2]^{3/2}} \left[C_0 + \sum_{n=1}^{\infty} \sum_l C_{n,l} \cos(n-2l)(\theta' - \theta'_s - \frac{2\pi R}{K}) \right] d\theta'_s dr_s dx_s \right.$$

$$= \frac{Q}{4\pi} \left(\frac{g rr_s^2}{[(x-x_s)^2 + r^2 + r_s^2]^{3/2}} \left[\sum_{R=1}^K C_0 \sin(\theta' - \theta'_s - \frac{2\pi R}{K}) + \sum_{n=1}^{\infty} \sum_l \sum_{R=1}^K C_{n,l} \cos(n-2l)(\theta' - \theta'_s - \frac{2\pi R}{K}) \right] \right.$$

$$\left. \times \sin(\theta' - \theta'_s - \frac{2\pi R}{K}) \right) d\theta'_s dr_s dx_s$$

It is shown that

$$\sum_{R=1}^K \sin(\theta' - \theta'_s - \frac{2\pi R}{K}) = 0$$

and

$$\sum_{n=1}^K \cos((n-2l)(\theta' - \theta'_s - \frac{2\pi R}{K})) \sin(\theta' - \theta'_s - \frac{2\pi R}{K})$$

$$= \begin{cases} \pm \frac{K}{2} \sin jK(\theta' - \theta'_s) & \text{if } n-2l = jK \neq 1 \ (j=1, 2, \dots) \\ & \text{and } j \neq K/2 \\ 0 & \text{otherwise} \end{cases}$$

(See Appendix A.)

Hence, we obtain

$$\frac{\partial \phi_s^*}{\partial t} = \pm \frac{\Omega}{4\pi} \iiint_{x_s, y_s, z_s} \frac{g r r_s^2}{[(x-x_s)^2 + r^2 + r_s^2]^{3/2}} \left[\sum_{n=1}^{\infty} \sum_l C_{n,l} \cdot \frac{K}{2} \sin jK(\theta' - \theta'_s) \right] d\theta'_s dr_s dx_s$$

(l : such that $n-2l = jK \neq 1$)

Together with the normal unit vector, the integral becomes :

On S_1 and S_2 ,

$$\pm \iint_{S_1 \cup S_2} \frac{\partial \phi_s^*}{\partial t} \hat{n} dS = \pm \iint_{r_{\theta'}} \frac{\Omega}{4\pi} \iiint \frac{g r r_s^2}{[(x-x_s)^2 + r^2 + r_s^2]^{3/2}} \left[\sum_j C_j \sin jK(\theta' - \theta'_s) \right] d\theta'_s dr_s dx_s r d\theta dr$$

Change the order of integration and execute the integral with θ' first. We have

$$\int_0^{2\pi} \sin jK(\theta' - \theta'_s) d\theta' = 0$$

Therefore,

$$\iint_{S_1 \cup S_2} \frac{\partial \phi_s^*}{\partial t} r r_s^2 dS = 0$$

On S_3 ,

$$\iint_0^{2\pi} \frac{\partial \phi_s^*}{\partial t} (\cos \theta' \hat{j}' + \sin \theta' \hat{k}') r d\theta' dr$$

$$= \pm \iint_{r_0} \frac{\Omega}{4\pi} \iiint \frac{g r r_s^2}{[(x-x_s)^2 + r^2 + r_s^2]^{3/2}} \left[\sum_j C_j \sin jK(\theta' - \theta'_s) \right] (\cos \theta' \hat{j}' + \sin \theta' \hat{k}') d\theta'_s dr_s dx_s r d\theta' dr$$

By orthogonality of trigonometric functions, we get

$$\int_0^{2\pi} \sin jK(\theta' - \theta'_s) \cos \theta' d\theta' = 0$$

$$\int_0^{2\pi} \sin jK(\theta' - \theta'_s) \sin \theta' d\theta' = 0$$

Hence, we have

$$\iint_{S_3} \frac{\partial \phi_i^*}{\partial t} n dS = 0$$

The term which corresponds to this in the moment equation, $\iint_{S_3} \frac{\partial \phi_i^*}{\partial t} (r \times n) dS$, is handled similarly.

Since

$$r \times n = r e_{\theta'} = r(-\sin \theta' j' + \cos \theta' k') \text{ on } S_1 \text{ or } S_2,$$

$$\text{and } " = r e_{\theta'} = r(-\sin \theta' j' + \cos \theta' k') \text{ on } S_3,$$

the integral is similar to $\iint_{S_3} \frac{\partial \phi_i^*}{\partial t} n dS$. The same argument as was used to handle that can be used.

Then it is obvious that

$$\iiint_{S_1+S_2+S_3} \frac{\partial \phi_i^*}{\partial t} (r \times n) dS = 0$$

Equations (4-23) and (4-24) reduce to

$$F_{B_L} + F_{B_D} - F_L^* = -P \iint_{S_w} (v u_n - v^* u_n^*) dS - P \iiint_{V_s} g(-\nabla_A \tilde{e} + v_i) r_s d\theta_s' dr_s dx_s$$

$$M_{B_L} + M_{B_D} - M_L = -P \iint_{S_w} r \times (v u_n - v^* u_n^*) dS - P \iiint_{V_s} g r_s \times (-\nabla_A \tilde{e} + v_i) r_s d\theta_s' dr_s dx_s$$

In examining the components of lifting force in the hypothetical flow, the same argument as that used in 2-D hydrofoil can be used. In this case however, there is trailing vortex extending to downstream. This has to be taken into account.

The lift F_L^* is decomposed as

$$F_L^* = F_{B_L} + \Delta F_L^*$$

where ΔF_L^* is the extra lift due to extra sources. This term is cancelled by the force on the extra sources due to bound vortices inside S. The force equation reduces to

$$F_{so} = -\rho \iint_{S_w} (v u_n - v^* u_n^*) dS - \rho \iiint_{V_s} \gamma (-v_n \hat{e} + v_i) r_s d\theta_s' dr_s d\chi_s$$

where v_i now represents induced velocity due to trailing vortex.

For the case of moment, the extra sources give rise to extra moment. The moment in the hypothetical flow is decomposed as

$$M_L^* = M_{L_{bl}} + \Delta M_L^*$$

This time, the last term does not cancel with the moment on the extra sources, but produce coupling moments. If we segregate those moments as ΔM_s , the moment equation becomes

$$M_{so} = -\rho \iint_{S_w} r \times (v u_n - v^* u_n^*) dS - \rho \iiint_{V_s} \gamma r_s \times (-v_n \hat{e} + v_i) r_s d\theta_s' dr_s d\chi_s + \Delta M_s$$

where v_i is the same as the force equation.

Since the wake is divided into K-identical wakes from the blades, we can redefine S_w as the wake on S for one blade only. Then, each surface integral will change to the sum of K integrals.

Define S_w : a part of control surface S which lies in the wake of one blade

V_s : volume of source distribution for one blade.

We can choose the radius R_c of the cylinder (control volume) large enough so that S_w lies on S_2 . If this is the

case, we have $\vec{u} = -\vec{e}$ and $u_n = -u_x$.

Hence,

$$\iiint_{V_s} g dV_s = - \iint_{S_w} (u_x^* - u_x) dS$$

And we obtain

$$\begin{aligned} F_{Bo} = & -PK \iint_{S_w} (u u_n - u^* u_n^*) dS - PK \nabla_A \vec{e} \cdot \iint_{S_w} (u_x^* - u_x) dS \\ & - PK \iiint_{V_s} g u_i dV_s \end{aligned} \quad (4-37)$$

$$\begin{aligned} M_{Bo} = & -PK \iint_{S_w} r \times (u u_n - u^* u_n^*) dS - PK \nabla_A \vec{e} \times \iint_{S_w} g r_s dV_s \\ & - PK \iiint_{V_s} (g r_s \times u_i) dV_s + \Delta M_s \end{aligned} \quad (4-38)$$

The axial component of the force and moment will be used later in the drag calculation. They are given by

$$\begin{aligned} F_{Box} = & PK \iint_{S_w} (u_x^2 - u_x^{*2}) dS - PK \nabla_A \cdot \iint_{S_w} (u_x^* - u_x) dS \\ & - PK \iiint_{V_s} g u_{ix} dV_s \end{aligned} \quad (4-39)$$

$$\begin{aligned} M_{Box} = & PK \iint_{S_w} r (u_\theta u_x - u_\theta^* u_x^*) dS - PK \iiint_{V_s} r_s g u_{i\theta} dV_s \\ & + \Delta M_{sx} \end{aligned} \quad (4-40)$$

Construction of Hypothetical Flow for Propeller The measurement point of velocities is fixed in space while the propeller turns. If looked from the propeller attached frame of reference, the measurement point draws a circle. The direction of rotation of the measurement point along this circle is opposite to the direction of propeller

rotation. The following discussion applies to the arc drawn by the measurement point.

If we take θ -component of Equation (4-30), we have

$$\frac{\partial v_{\theta}^*}{\partial t} + \frac{1}{r} \frac{\partial}{\partial \theta} \left(\frac{1}{2} |v^*|^2 \right) = \frac{\partial v_{\theta}}{\partial t} + \frac{1}{r} \frac{\partial}{\partial \theta} \left(\frac{1}{2} |v|^2 \right) - (v_x \omega_{\theta r} - v_r \omega_{\theta x})$$

The time derivative is now replaced by that w.r.t. θ' , if we make use of (4-35).

$$\frac{\partial v_{\theta}^*}{\partial t} = -\Omega \frac{\partial v_{\theta}^*}{\partial \theta'}, \quad \frac{\partial v_{\theta}}{\partial t} = -\Omega \frac{\partial v_{\theta}'}{\partial \theta'}$$

And also partial differentiation w.r.t. θ is replaced by that w.r.t. θ' , giving

$$\begin{aligned} & \frac{1}{r} \frac{\partial}{\partial \theta'} [-\Omega r v_{\theta}^* + \frac{1}{2} \{ v_x^{*2} + v_r^{*2} + (v_{\theta}^* + r\Omega)^2 \}] \\ & = \frac{1}{r} \frac{\partial}{\partial \theta'} [-\Omega r v_{\theta}' + \frac{1}{2} \{ v_x^2 + v_r^2 + (v_{\theta}' + r\Omega)^2 \}] - (v_x \omega_{\theta r} - v_r \omega_{\theta x}) \end{aligned}$$

Here, the relation $v_{\theta} = v_{\theta}' + r\Omega$ was also used. The equation reduces to

$$\frac{1}{r} \frac{\partial}{\partial \theta'} \left[\frac{1}{2} \{ v_x^{*2} + v_r^{*2} + v_{\theta}^{*2} \} \right] = \frac{1}{r} \frac{\partial}{\partial \theta'} \left[\frac{1}{2} \{ v_x^2 + v_r^2 + v_{\theta}'^2 \} \right] - (v_x \omega_{\theta r} - v_r \omega_{\theta x})$$

Integrating with respect to θ' and multiplying by 2, we obtain

$$v_x^{*2} + v_r^{*2} + v_{\theta}^{*2} = v_x^2 + v_r^2 + v_{\theta}'^2 - 2 \int_{\theta'} (v_x \omega_{\theta r} - v_r \omega_{\theta x}) r d\theta' \quad (4-41)$$

This equation still seems to have three unknowns. But if we use the assumption stated previously, which is $v^* - v // \omega_r$, we only need to solve for one component in the transformed coordinates.

Let us define a coordinate system $o' - \xi \eta \zeta$, ξ -axis being

parallel to trailing vorticity ω_r . η and ζ axes are rather arbitrary as long as the three axes make an orthogonal system. This coordinate system should be considered locally, or at each point of interest, since the orientation of the trailing vorticity may vary with radius. The transformation is done by first shifting the origin o' from o to the point of interest and then rotating the axes so that ζ -axis be parallel to the trailing vorticity. There is no relative motion between $o-xr\theta'$ and $o'-\xi\eta\zeta$ systems, which gives

$$v_x^2 + v_r^2 + v_{\theta'}^2 = v_\xi^2 + v_\eta^2 + v_\zeta^2 \quad (4-42)$$

Hence Equation (4-41) becomes

$$v_\xi^{*2} + v_\eta^{*2} + v_\zeta^{*2} = v_\xi^2 + v_\eta^2 + v_\zeta^2 - 2 \int_{\theta'} (v_x \omega_{\theta'} - v_r \omega_{\theta'}) r d\theta'$$

But from the assumption, we have

$$v^* - v = (v_\xi^* - v_\xi) e_\xi.$$

Then we obtain

$$v_\eta^* = v_\eta \quad \text{and} \quad v_\zeta^* = v_\zeta.$$

Finally, we have

$$v_\xi^{*2} = v_\xi^2 - 2 \int_{\theta'} (v_x \omega_{\theta'} - v_r \omega_{\theta'}) r d\theta' \quad (4-43)$$

Once v_ξ^* is obtained, then through inverse transformation, v_x^* , v_r^* and $v_{\theta'}^*$ can be obtained.

Induced velocity The presence of trailing vorticity gives rise to induced velocity which changes the inflow to the

blade.

To fully evaluate the forces in Equations (4-39) and (4-40), the induced velocity and source distribution q have to be obtained. Since the induced velocity is caused by the presence of trailing vortices, the strength of them has to be first obtained. This information is then fed into the Biot-Savart law to calculate the velocity on the blade.

FPV-10 by Kerwin[6] and PSFFPV by Greeley[15] are ones which do such computations. These programs were designed for the computation of field point velocity due to a propeller. They are also capable of separating each element of velocity, like velocity due to trailing vortex only.

The source distribution is more difficult to get. To know it exactly, one has to solve a boundary value problem, which is fairly involved. Since it is not the main theme of this paper to solve for source distribution, a reasonable approximation is to be used to simplify the computation. One such approximation could be to use the mean values of the induced velocities, assuming that the variation of them across the source distribution is relatively small. The third term of Eq.(4-39) and the second term of Eq.(4-40), on right sides, are then approximated by

$$- \rho K \bar{v}_{ix} \iiint_{V_s} q dV_s \quad \text{and} \quad - \rho K \bar{v}_{io} \iiint_{V_s} r_s q dV_s$$

Profile Drag Coefficient The most convenient way for the drag coefficient to be specified would be to have it given at each radius. This requires strip theory assumption, in

other words, flow on the blade is 2-dimensional along the radius. While it is said that the flow on the blade is fairly complicated in 3-dimensional way[14], it is still considered to be convenient to define C_d at each radius. Of course we could define C_d for the whole blade. However, this will not give much detail on the distribution of drag along the radius.

Let the drag be $DR_i(r)$, which is, according to propeller convention, parallel to the resultant inflow. Then profile drag coefficient C_d is given by

$$C_d(r) = \frac{DR_i(r)}{\frac{1}{2} \rho C (\nabla_A^2 + r^2 \Omega^2)} \quad (4-44)$$

where c is the chord length at each radius.

Assuming the drag to be a function of r correspondingly requires that force and moment be given as functions of r .

Suppose

$$F_{BDX} = \int_r F_{sec}(r) dr \quad \text{sec : sectional} \quad (4-45)$$

$$M_{BDX} = \int_r M_{sec}(r) dr \quad (4-46)$$

then

$$\begin{aligned} F_{sec} = & \rho K \int_{s_w} (v_x^2 - v_x^{*2}) ds - \rho K \nabla_A \int_{s_w} (v_x^* - v_x) ds \\ & + \rho K \overline{v_{ix}}(r) \int_{s_w} (v_x^* - v_x) ds \end{aligned} \quad (4-47)$$

$$M_{sec} = PKr \int_{S_w} (v_\theta v_\alpha - v_\theta^* v_\alpha^*) ds + PKr \overline{v_{i0}(r)} \int_{S_w} (v_\alpha^* - v_\alpha) ds \quad (4-48)$$

The surface integral in S_w was replaced by line integral. The approximation stated on the induced velocity is used here, and the extra moment $\Delta M_{s\alpha}$ is neglected. It has to be kept in mind that the radius of measurement does not necessarily correspond to the radius in question on the blade. Proper correction has to be made for the actual trajectory of the viscous wake.

$DR_i(r)$ is given by

$$\begin{aligned} DR_i(r) &= -\frac{1}{K} \left[F_{sec}(r) \sin \beta_i + \frac{M_{sec}(r)}{r} \cos \beta_i \right] \\ &= -\frac{1}{K} \left[F_{sec}(r) (\sin \beta \cos \gamma + \cos \beta \sin \gamma) \right. \\ &\quad \left. + \frac{M_{sec}(r)}{r} (\cos \beta \cos \gamma - \sin \beta \sin \gamma) \right] \end{aligned}$$

where $\gamma = \beta_i - \beta$

and

β : hydrodynamic pitch angle without induced velocity

β_i : " " with induced velocity included

$$D_{Ri}(r) = -\frac{1}{K} \left[F_{sec} \left\{ \frac{J' \cos \gamma}{(1+J'^2)^{1/2}} + \frac{\sin \gamma}{(1+J'^2)^{1/2}} \right\} \right. \\ \left. + \frac{M_{sec}}{r} \left\{ \frac{\cos \gamma}{(1+J'^2)^{1/2}} - \frac{J' \sin \gamma}{(1+J'^2)^{1/2}} \right\} \right]$$

and hence

$$C_d(r) = \frac{D_{Ri}(r)}{\frac{1}{2} \rho c r^2 \Omega^2 (1+J'^2)} \\ = \frac{-2 \cos \gamma}{\rho c r^2 \Omega^2 K (1+J'^2)^{1/2}} \left[F_{sec} (J' + \tan \gamma) + \frac{M_{sec}}{r} (1 - J' \tan \gamma) \right]$$

Substituting Equations (4-47) and (4-48), we have

$$C_d(r) = \frac{-2 \cos \gamma}{c r^2 \Omega^2 (1+J'^2)^{1/2}} \left[\int_{s_w} (\bar{u}_x^* - \bar{u}_x) \{ (-\bar{v}_A + \bar{u}_{ix} - \bar{u}_x^* - \bar{u}_x) (J' + \tan \gamma) \right. \\ \left. + \bar{u}_{i\theta} (1 - J' \tan \gamma) \} ds \right. \\ \left. + (1 - J' \tan \gamma) \int_{s_w} (\bar{u}_\theta \bar{u}_x - \bar{u}_\theta^* \bar{u}_x^*) ds \right] \quad (4-49)$$

where $\tan \gamma$ is given by

$$\tan \gamma = \frac{(\bar{u}_{i\theta} J' - \bar{u}_{ix}) J'}{(\bar{v}_A - \bar{u}_{ix}) J'^2 + \bar{v}_A - \bar{u}_{i\theta} J'}$$

Results The velocity and vorticity distribution obtained

from the experiment and shown in Chapter 3 were used to compute profile drag. First, it was tried to compute the hypothetical velocity using Eq.(4-43). Finding the edges of the wake from vorticity distribution, integration was done with boundary conditions $\mathcal{V}_\xi^* = \mathcal{V}_\xi$ at the both edges of the wake. One successful (which means that the integral started one edge and arrived at the other edge) example is shown in Figure 4-17.

This hypothetical flow seems wiggly. From the comparison with 2-D hypothetical flow, it is suspected that this is due to the noise in the vorticity which was used in the computation. As the vorticity is given by differentiation, it becomes very sensitive to the error in the data. Often at other radii, the computation of the hypothetical flow failed presumably due to the accumulation of error from vorticity.

To improve the situation, it is desired to further modify the integral in Eq.(4-43), or to improve the accuracy of the vorticity measurement.

A first approximation of the boundary layer theory tells us that static pressure is constant across the boundary layer or wake. For a moderately loaded propeller, this assumption is considered to be valid. If this is the case, the hypothetical velocity is also obtained as constant across the wake.

To see this, a few points along a streamline of viscous wake were picked up as control points in the drag calculation. At far downstream, the above assumption is

considered to be more realistic. If the values of the drag obtained at points closer to the blade do not differ so much from the one obtained at the furthest point, then the validity of this assumption is implied.

Figure 4-18 shows an example of straight line hypothetical flow. In figure 4-19 are plotted the values of the profile drag thus obtained at three different positions along the viscous wake streamline for Prop.4381. The agreement of Cd value between the points is quite good, proving the validity of the assumption.

Figure 4-20 illustrates the coefficient of profile drag computed from the measured velocity, under above mentioned assumption, at various radii for the two propellers.

Toward the end of the series of experiments, the author had an opportunity to test Prop.4381 with smoother surface condition than before. This was due to re-surfacing. Hence, the conditions of the blade surfaces are

Prop.4381	Relatively smooth, marked by	X
" "	With rough L.E., marked by	Δ
Prop.4383	Relatively smooth, marked by	\diamond .

The two different surface conditions of the Prop.4381 give considerable difference to Cd.

The propeller rpm for these points is 900rpm. At 0.7R, however, the results at 600rpm and 1200rpm are also added.

The radius vs. Cd curves show fairly complicated behavior. At mid-radius (about 0.6R), the Cd values are not so much different from what they would be in 2-D flow. But toward the outer or inner radii, they become lower. And

this '2-D like' region is narrower at Prop.4383 than Prop.4381, which may imply the skew effect. And at further outer or inner radii, the values go up again. This is particularly so at Prop.4381, but not so distinct at Prop.4383.

This trend of C_d reduction toward the tip is consistent with what we observed in 3-D hydrofoil. Since the aspect ratio of a marine propeller is much smaller than airplane wing, the region of influence by the tip may be larger.

Toward the propeller hub, a similar effect could occur, since the hub corresponds to the tip on the other side of a wing. Besides, the flow in this region may be more complicated due to the presence of the hub and interactions between the blades.

The low C_d at outer radii ($>0.7R$) for Prop.4383 may be partially due to possibly nontrivial turbulence level of the flow. If so, the present method will give an error to C_d , since that is neglecting the turbulence components which appear as Reynolds stress type terms in the C_d calculation. From the analogy to a swept back wing, it is likely that the transition from laminar to turbulent flow is taking place there in the thickened boundary layer due to spanwise (radial) flow[22].

Since the flow is quite 3-dimensional at the both ends of the blade, it may not be adequate to define sectional drag there. For a more accurate estimation of the drag, it is desired first to take the whole drag which is counted in the tip (or hub) vortex and redistribute that over the (part

of the) radius.

The drag coefficient is based on undisturbed inflow to the blade. But near the hub, it could be possible that the inflow is already retarded due to the presence of the propeller shaft boundary layer. If this is the case, the actual inflow velocity should be used. This will increase the C_d values near the hub.

5. Conclusions

The following conclusions were obtained.

1) LDV has proven itself to be a handy and yet powerful tool in the analysis of the flow around a propeller.

2) The wake from a loaded propeller blade is categorized into two, trailing vortex wake and viscous wake. Trailing vortex wake is created by the tip vortex, whereas the viscous wake comes from the blade boundary layers. Since the origins are different, they have to be considered as separate. Trailing vortex wake appears on the suction side of viscous wake. This is particularly so at outer radii. They almost line up at inner radii.

3) Relating to 2), the vorticity in the wake is also separated into two, trailing vorticity and boundary layer type vorticity. By finding the orientation of the trailing vorticity from the velocity components, new coordinate system $O'-\xi\eta$ was constructed in which ξ -axis is parallel to the trailing vorticity at the locus. This method works fairly well to separate the two vorticities. ξ -component of the vorticity (ω_ξ) appears to be an even function of θ' which we expect it to be, and the second component (ω_η) shows a typical vorticity distribution in the boundary layers. It was also found that, at some radii, the complete separation of the vorticities is not possible only by the

coordinate transformation. This is due to the 'contamination' of the viscous wake vorticity into the trailing vorticity.

4) The Propeller Field Point Velocity Program (FPV-10) predicts velocities fairly well within the limit of potential flow. Also, it can be expected that the modified version of it (PSFFPV) improves the ability of FPV-10.

5) A formula for the profile drag (viscous sectional drag) was derived in terms of the velocities (real and hypothetical). And a method to obtain the hypothetical velocity was suggested. It was shown that the formula worked perfectly with 2-D hydrofoils. For propeller case, however, due to the accuracy problem in vorticity measurement, the hypothetical velocity sometimes has a problem. It is desired either or both to improve the measurement accuracy of the vorticity and to further modify the formula for the hypothetical velocity so that it can use the velocity itself rather than the vorticity. It was also shown that a simple assumption for the hypothetical velocity (U_f^* = straight across the wake) could be used for the computation of the profile drag.

6) Radial distribution of the profile drag obtained from the velocity data showed fairly complicated behavior. At mid-radius range, the value is closer to what it would be in 2-D flow. But toward outer or inner radii, C_d becomes

substantially low. It was implied that considerable amount of momentum defect in the blade boundary layer is pulled into the tip vortex, thus making the drag appear lower in its vicinity. The same trend is reported in aerofoil flow even at zero lift.

7) The concept of profile (or sectional) drag may lose its validity near the blade tip (or the propeller hub) since the flow there is fairly 3-dimensional due to the swirling of the tip vortex (or hub vortex). It is therefore desirable to establish a way to estimate the total momentum and pressure loss (drag) which is involved in the tip vortex (hub vortex) and redistribute that over the (part of the) radius (or span) to get correct profile drag distribution.

8) In this paper, the turbulence of the flow (in the wake) was assumed to be small and was neglected. However, for more detailed study of the flow around a propeller, and for more accurate estimation of the profile drag especially for a skewed propeller, it would be desirable to know the turbulence level. To that end, the author feels it necessary first to establish a method to segregate the noise in the Laser signal from the turbulence component of the flow. A flow visualization technique using oil film on the propeller blade would supplement the LDV measurement to get the turbulence level[23].

REFERENCES

1. Lap, J. W. and Van Manen, J. D., Fundamentals of Ship Resistance and Propulsion pp.119 - 121 NSMB
2. Kerwin, J. E. and Lee, C-S "Prediction of Steady and Unsteady Marine Propeller Performance by Numerical Lifting-Surface Theory" SNAME Annual Meeting, New York, 1978
3. Lee, C-S "Documentation of the Program for Propeller Unsteady Force Calculation" Department of Ocean Engineering, MIT December, 1977
4. Lee, C-S "User's Manual of MIT-PUF-3 Program for the Prediction of Cavity Extent and Volume Variation on Marine Propellers" September, 1979 MIT
5. Kerwin, J. E., PBD-10 in preparation at MIT
6. Kerwin, J. E., "Propeller Field Point Velocity Program FPV-10 User's Manual" Department of Ocean Engineering, MIT December, 1979
7. Min, Keh-Sik "Numerical and Experimental Methods for the Prediction of Field Point Velocities Around Propeller Blades" Ph.D. Thesis, Department of Ocean Engineering, MIT, 1978

8. Betz, A. "A Method For The Direct Determination Of Wing-Section Drag" (Translation) National Advisory Committee For Aeronautics, Technical Memorandum No.337, 1925

or, Schlichting, H. Boundary-Layer Theory

7th Edition pp.759 - 761 McGraw-Hill, New York 1979

9. Sayre, H. C., "Laser Doppler Anemometry and The Measurement of Loading Characteristics of Lifting Sections" Presented at The SNAME New England Section Meeting, December, 1980.
10. Orloff, K. L., "Spanwise Lift Distribution on a Wing from Flowfield Velocity Surveys" Journal of Aircraft, Vol.17, No.12, December, 1980
11. Boswell, R. J. "Design, Cavitation Performance, and Open-Water Performance of A Series of Research Skewed Propellers", DTNSRDC Report 3339 March, 1971
12. Nelka, J. J. "Experimental Evaluation of A Series of Skewed Propellers with Forward Rake : Open Water Performance, Cavitation Performance, Field-Point Pressures, And Unsteady Propeller Loading", DTNSRDC Report 4113 July, 1974

13. Goldstein, R. J. and Hagen, W. F. "Turbulent Flow Measurements Utilizing The Doppler Shift of Scattered Laser Radiation", Phys. Fluids 10, 1349 1967
14. Meyne, K. "Investigation of Propeller Boundary-Layer Flow and Friction Effect on Propeller Characteristics" Jahrbuch der Schiffbautechnischen Gesellschaft Band 66 pp.317 - 399
15. PSFFPV by Greeley, D. S. under progress at MIT
16. Tan, C. S. "Vorticity Modelling of Blade Wakes Behind Isolated Annular Blade-Rows: Induced Disturbances in Swirling Flows" Presented at Gas Turbine Conference & Products Show, New Orleans, March, 1980
17. Baker, G. R., Barker, S. J., Bofah, K. K. and Saffman, P. G., "Laser anemometer measurements of trailing vortices in water" Journal of Fluid Mechanics, Vol.65, part 2, pp.325 - 336, 1974
18. Newman, J. N. Marine Hydrodynamics pp.57 - 59 MIT Press 1978
19. Unpublished paper by Moas, E. "Drag Coefficient Determination for a NACA-66 Hydrofoil in 2-D Flow" MIT UROP Project, 1980

20. Abbott, I. H. and Von Doenhoff, A. E., Theory of Wing Sections Dover, New York
21. Hoerner, S. F. Fluid-Dynamic Drag pp.6-4, 6-20
Published by The Author, 1965
22. Hazen, D. C. "The Rebirth of Subsonic Aerodynamics"
Astronautics & Aeronautics pp.24 - 39 November, 1967
23. Unpublished paper by Baker, E. S. and Kobayashi, S.
about the flow visualization on the propeller blade
using oil film, MIT Department of Ocean Engineering,
1981

APPENDIX A

$$i) \sum_{k=1}^K \cos((n-2l)(\phi - \frac{2\pi k}{K})) \sin(\phi - \frac{2\pi k}{K})$$

$$= \begin{cases} \pm \frac{K}{2} \sin(jK\phi) & \text{if } n-2l = jK \neq 1 \text{ (} j=1, 2, \dots \text{) and } K \neq 2 \\ 0 & \text{otherwise} \end{cases}$$

[Proof]

$$\cos((n-2l)(\phi - \frac{2\pi k}{K})) \sin(\phi - \frac{2\pi k}{K})$$

$$= \frac{1}{2} \left[\sin((n-2l+1)(\phi - \frac{2\pi k}{K})) - \sin((n-2l-1)(\phi - \frac{2\pi k}{K})) \right]$$

Then,

$$\sum_{k=1}^K \sin((n-2l+1)(\phi - \frac{2\pi k}{K})) = \mathcal{I}_m \sum_{k=1}^K e^{i(n-2l+1)(\phi - \frac{2\pi k}{K})}$$

$$= \mathcal{I}_m e^{i(n-2l+1)\phi} \sum_{k=1}^K e^{-i(n-2l+1)\frac{2\pi k}{K}}$$

Write $n-2l+1 = m$ and write $S = \sum_{k=1}^K e^{-im\frac{2\pi k}{K}}$.

Then,

$$S - e^{-im\frac{2\pi}{K}} S = (e^{-im\frac{2\pi}{K}} + e^{-im\frac{4\pi}{K}} + \dots + e^{-im\frac{2\pi K}{K}})$$

$$- (e^{-im\frac{4\pi}{K}} + \dots + e^{-im\frac{2\pi K}{K}} + e^{-im\frac{2\pi K}{K} - im\frac{2\pi}{K}})$$

$$= e^{-im\frac{2\pi}{K}} - e^{-im\frac{2\pi}{K}} e^{-2\pi m i}$$

$$(1 - e^{-im\frac{2\pi}{K}}) S = e^{-im\frac{2\pi}{K}} (1 - e^{-2\pi m i})$$

Since $e^{-2\pi m i} = 1$ (m =integer), the right hand side is zero.

Hence, $S = 0$ if $\frac{m}{K}$ is integer, i say.

If $\frac{m}{K} = j$, then

$$S = \sum_{k=1}^K e^{-2\pi j k} = \sum_{k=1}^K 1 = K$$

The same is true with the second term, $\sum_{k=1}^K \sin((n-2l-1)\phi - \frac{2\pi k}{K})$.

It is only when $K=2$ that $n-2l+1=jK$ and $n-2l-1=j'K$ hold simultaneously. Otherwise, we have

$$\begin{aligned} & \cos((n-2l)\phi - \frac{2\pi k}{K}) \sin(\phi - \frac{2\pi k}{K}) \\ &= \begin{cases} \pm \frac{1}{2} K \sin(jK\phi) & \text{if } n-2l = jK \neq 1 \ (j=1,2,3,\dots) \\ & \text{and if } K \neq 2 \\ 0 & \text{otherwise} \end{cases} \end{aligned}$$

$$\text{ii) } \sum_{k=1}^K \sin(\phi - \frac{2\pi k}{K}) = 0$$

[Proof]

This corresponds to the case when $n-2 = 0$ in the above (i). Since $jK+1 \neq 0$, this is the second case. Hence, the sum is zero.

Q.E.D.

Table 2-1 Data Acquisition System

Item	Manufacturer	Remark
Laser Doppler Velocimeter		
Laser Transmitter	Spectra Physics	Dual Beam Forward Scatter Mode He-Ne Laser (15mW) Wavelength=632.8 nm
Transmitting Optics	Thermo-Systems Inc.	
Beam Splitter	"	Model 915
Frequency Shifter	"	Model 985
" (Bragg cell)		Model 982
Transmitting Lenses	Thermo-Systems Inc.	F=309mm 481mm
Receiving Optics		
Photo-Multiplier	"	Model 9162
Signal Processor	"	
LDA Signal Processor	"	Model 1090
Signal Conditioner	"	Model 1057
Monitor and Power Supply	"	Model 1091
Data Reduction		
Mini-Computer	Digital Equipment	MINC-11 (28K words)
A/D Converter	"	Resolution=0.0025Volts
Digital Plotter	TEKTRONIX	Model No.4662
Line Printer	Digital Equipment	Decwriter II

Table 2-2 Geometry of The Propellers

Number of Blades	5
Expanded Area Ratio	0.725
Section Meanline	NACA a=0.8
Section Thickness Distribution	NACA 66 with NSRDC modified nose and tail
Design J	0.889
Design K	0.213

r/R	tan	c/D	t/c
0.2	1.8256	0.174	0.2494
0.3	1.3094	0.229	0.1562
0.4	1.0075	0.275	0.1068
0.5	0.8034	0.312	0.0768
0.6	0.6483	0.337	0.0566
0.7	0.5300	0.347	0.0421
0.8	0.4390	0.334	0.0314
0.9	0.3681	0.280	0.0239

Propeller 4381(Skew=0 deg)

r/R	(deg)	P/D	f /c
0.3	0.0	1.3448	0.0368
0.4	0.0	1.3580	0.0348
0.5	0.0	1.3361	0.0307
0.6	0.0	1.2797	0.0245
0.7	0.0	1.2099	0.0191
0.8	0.0	1.1366	0.0148
0.9	0.0	1.0660	0.0123

Propeller 4382(Skew=36 deg)

r/R	(deg)	P/D	f /c
0.3	4.655	1.4332	0.0370
0.4	9.363	1.4117	0.0344
0.5	13.948	1.3613	0.0305
0.6	18.378	1.2854	0.0247
0.7	22.747	1.1999	0.0199
0.8	27.145	1.111	0.0161
0.9	31.575	1.0270	0.0134

Table 2-2 (Continued)

Propeller 4497(Warp=36 deg)

r/R	(deg)	P/D	f /c
0.3	4.655	1.4332	0.0370
0.4	9.363	1.4117	0.0344
0.5	13.948	1.3613	0.0305
0.6	18.378	1.2854	0.0247
0.7	22.747	1.1999	0.0199
0.8	27.145	1.1117	0.0161
0.9	31.575	1.0270	0.0134

Propeller 4383(Skew=72 deg)

r/R	(deg)	P/D	f /c
0.3	9.293	1.5124	0.0407
0.4	18.816	1.4588	0.0385
0.5	27.991	1.3860	0.0342
0.6	36.770	1.2958	0.0281
0.7	45.453	1.1976	0.0230
0.8	54.245	1.0959	0.0189
0.9	63.102	0.9955	0.0159

Propeller 4498(Warp=72 deg)

r/R	(deg)	P/D	f /c
0.3	9.293	1.5124	0.0407
0.4	18.816	1.4588	0.0385
0.5	27.991	1.3860	0.0342
0.6	36.770	1.2958	0.0281
0.7	45.453	1.1976	0.0230
0.8	54.245	1.0959	0.0189
0.9	63.102	0.9955	0.0159

AD-A109 846 MASSACHUSETTS INST OF TECH CAMBRIDGE DEPT OF OCEAN E--ETC F/6 13/10
EXPERIMENTAL METHODS FOR THE PREDICTION OF THE EFFECT OF VISCOS--ETC(U)
JUN 81 S KOBAYASHI N00014-76-C-0357
UNCLASSIFIED OE-81-7 NL

2 OF 2

AD A
010 66

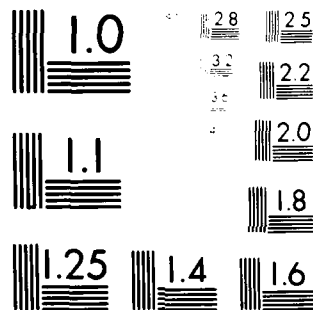
END

DATE

FILED

02-82

DTIC



MICROCOPY RESOLUTION TEST CHART
NATIONAL BUREAU OF STANDARDS-1963-A

Table 3-1 Distance from T.E. along Helical Line
to Each Measurement Point

r/R	Distance/Chord	
	Prop.4381 (X=-0.333R)	Prop.4383 (X=-0.488R)
0.30	0.462	0.860
0.40	0.412	0.688
0.50	0.428	0.567
0.60	0.502	0.483
0.70	0.639	0.427
0.80	0.880	0.407
0.875	-	-
0.90	1.396	0.483

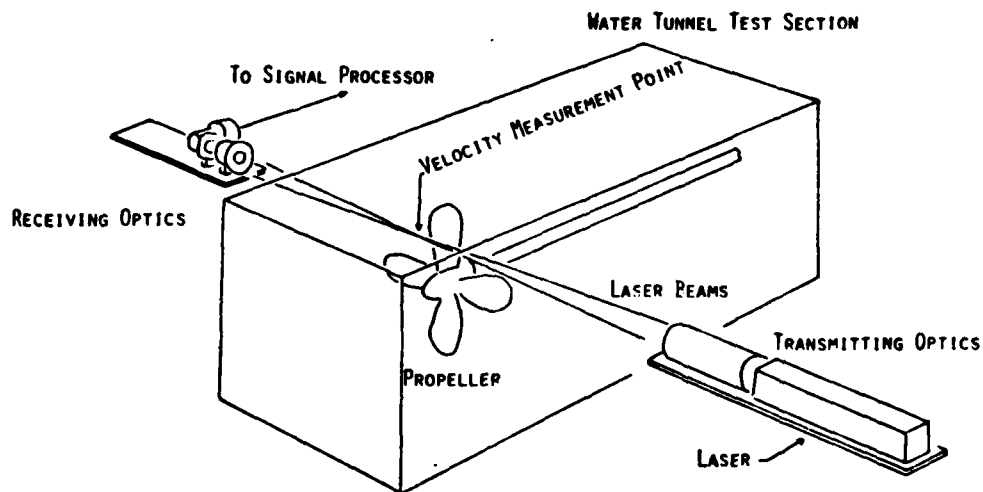


FIGURE 2-1 EXPERIMENTAL SET-UP FOR VELOCITY MEASUREMENT

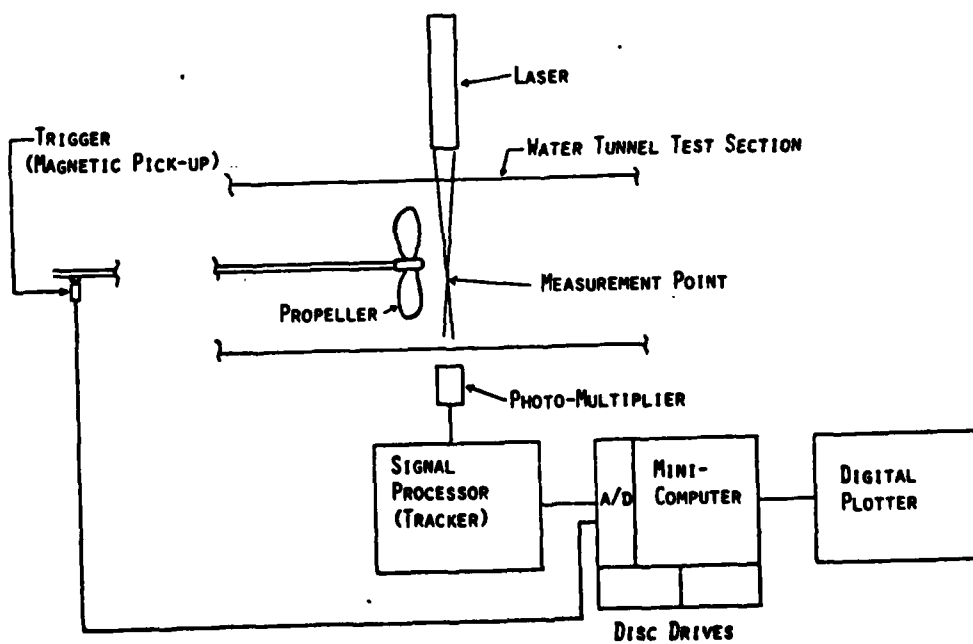


FIGURE 2-2 SCHEMATIC REPRESENTATION OF DATA ACQUISITION SYSTEM

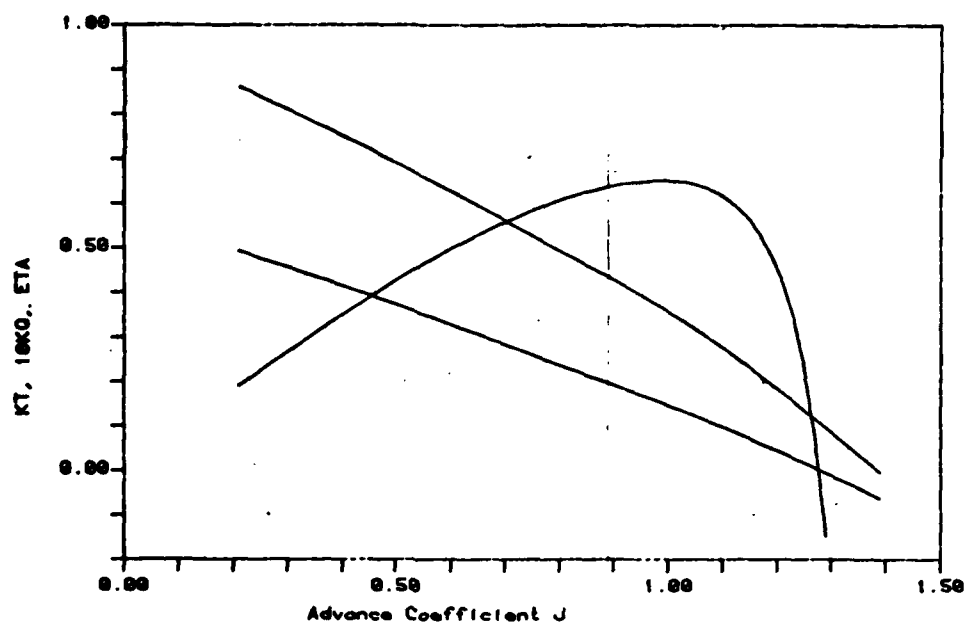


Figure 2-3 Result of Open Water Test
Prop. DTNSRDC4381 Run at 900rpm MIT MHL Sept5, 1980

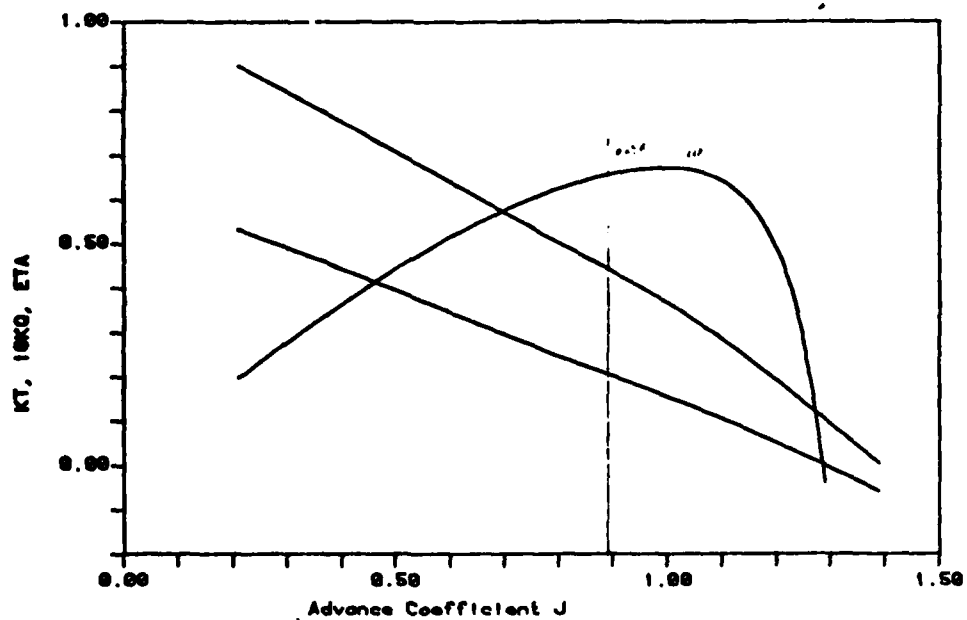


Figure 2-4 Result of Open Water Test
Prop. DTNSRDC4382 Run at 900rpm MIT MHL Sept5, 1980

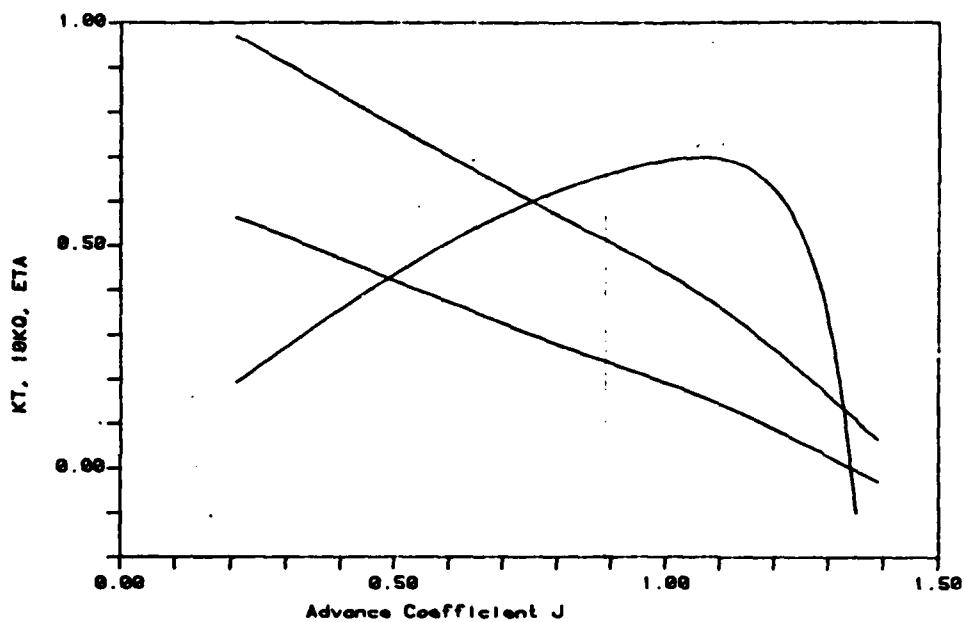


Figure 2-5 Result of Open Water Test
Prop. DTNSRDC4497 Run at 900rpm MIT MHL Sept5, 1980

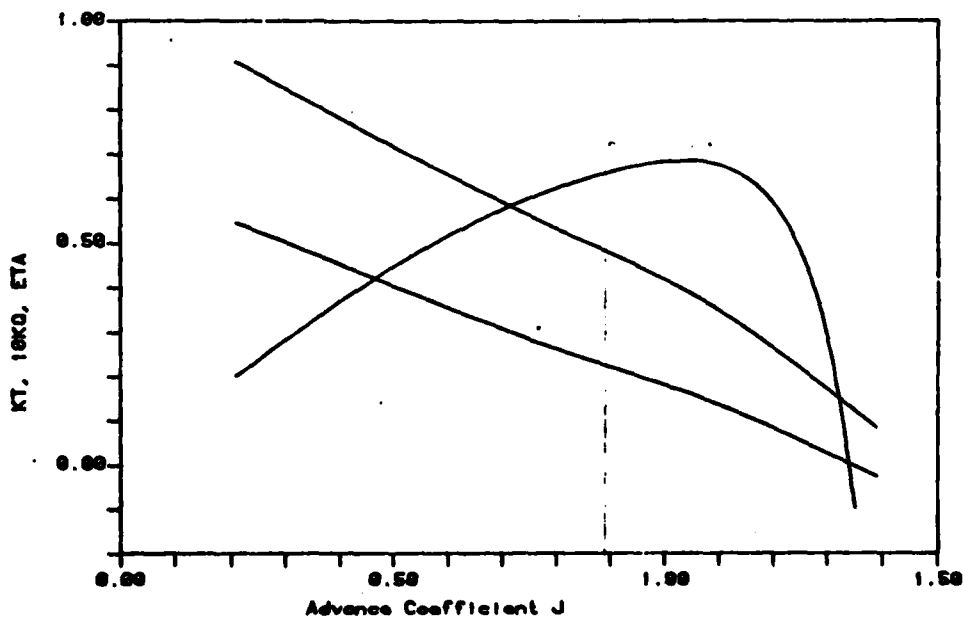


Figure 2-6 Result of Open Water Test
Prop. DTNSRDC4383 Run at 900rpm MIT MHL Sept5, 1980

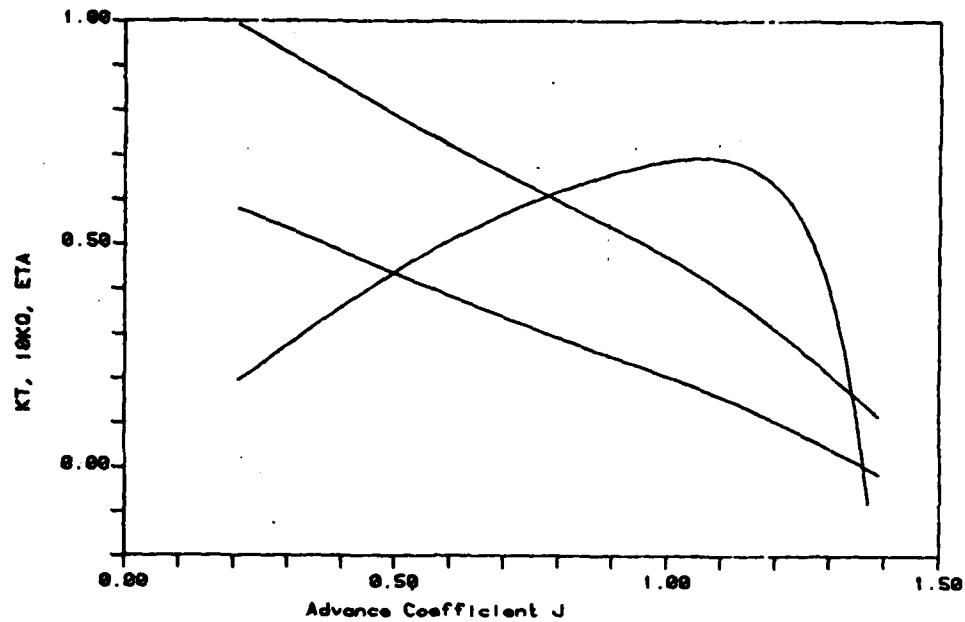


Figure 2-7 Result of Open Water Test
Prop. DTNSRDC4498 Run at 900rpm MIT MHL Sept5, 1980

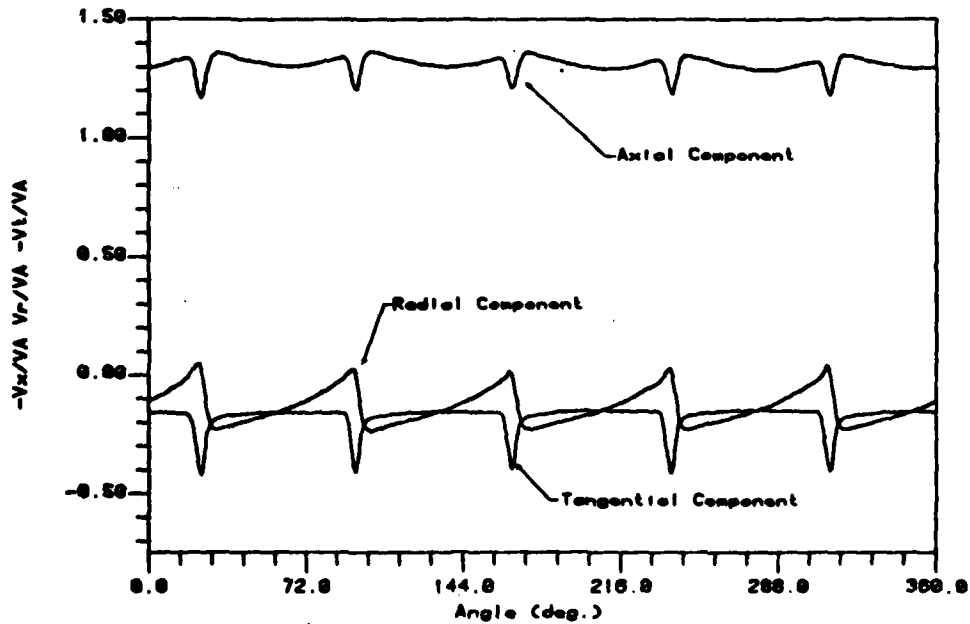


Figure 3-5 Field Point Velocity Measured by LDV
Prop. 4381 at Design J $x=-.33R$, $r=.7R$ Average of 500

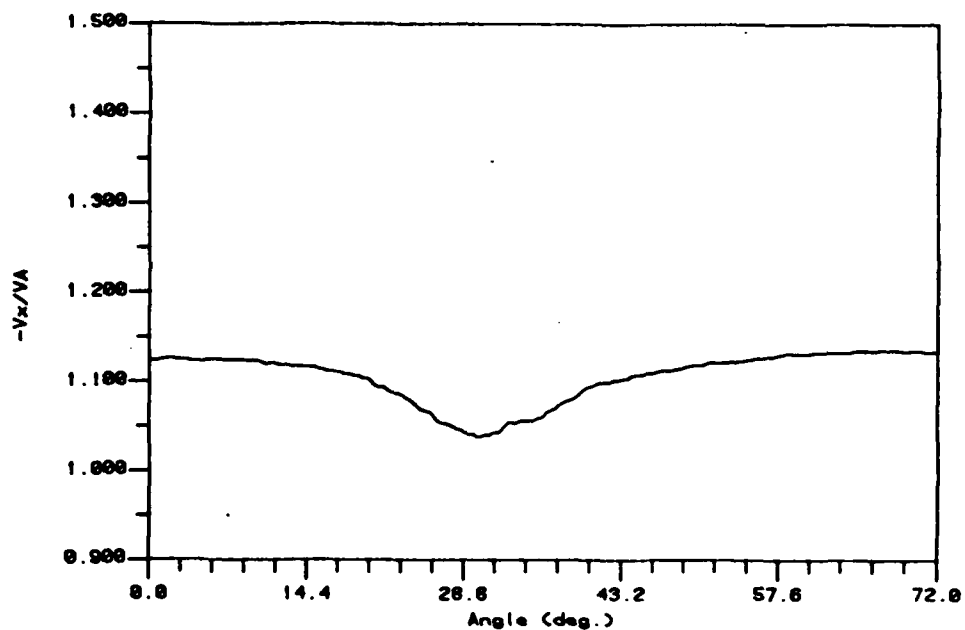


Figure 3-6a Field Point Velocity (Axial component)
Prop. 4381 at $x=-0.333R$, $r=0.250R$ at Design J

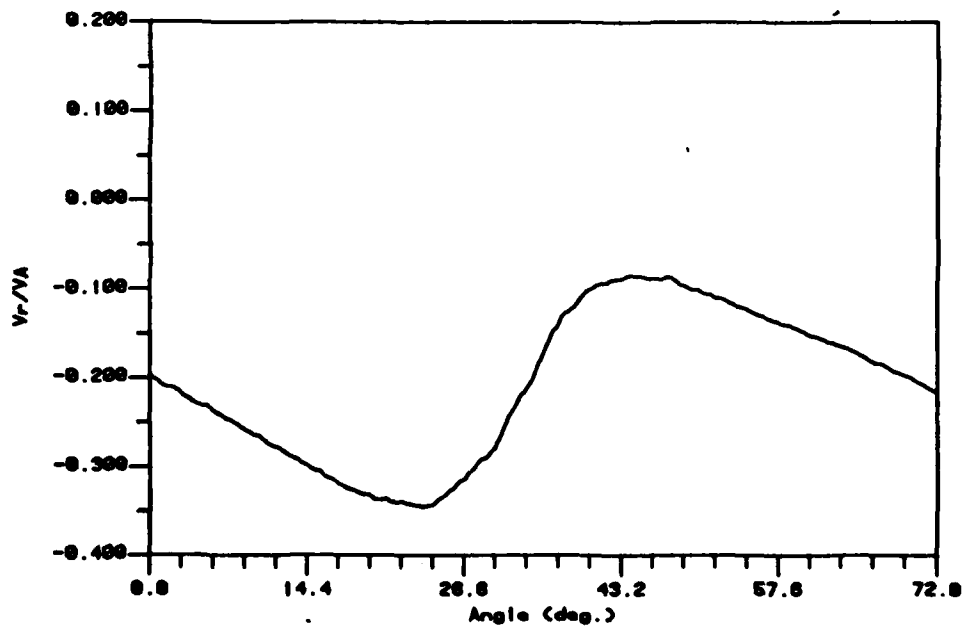


Figure 3-6b Field Point Velocity (Radial component)
Prop. 4381 at $x=-0.333R$, $r=0.250R$ at design J

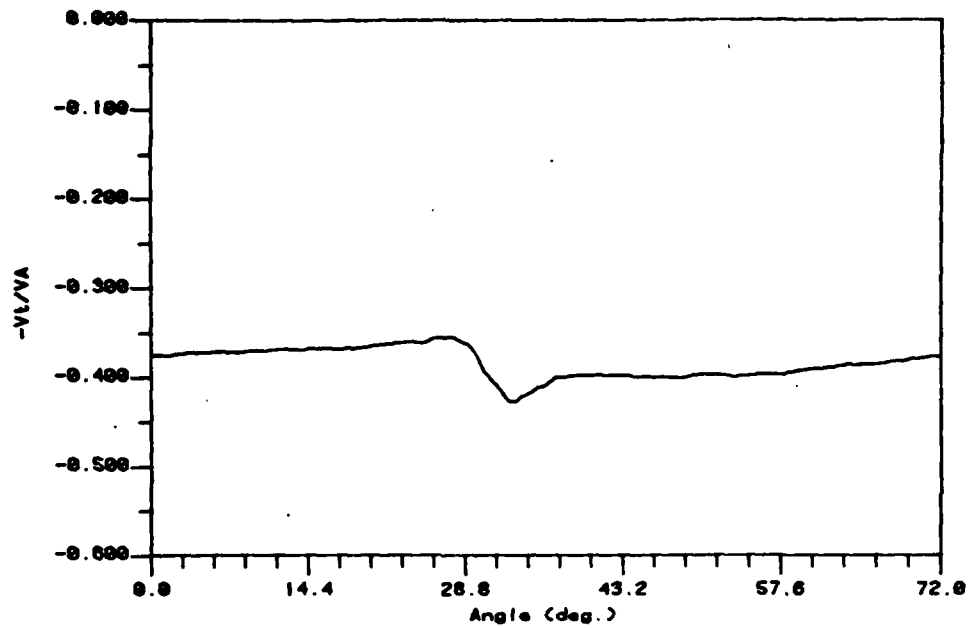


Figure 3-6c Field Point Velocity (Tangential component)
Prop. 4381 at $x=-0.333R$, $r=0.250R$ at Design J

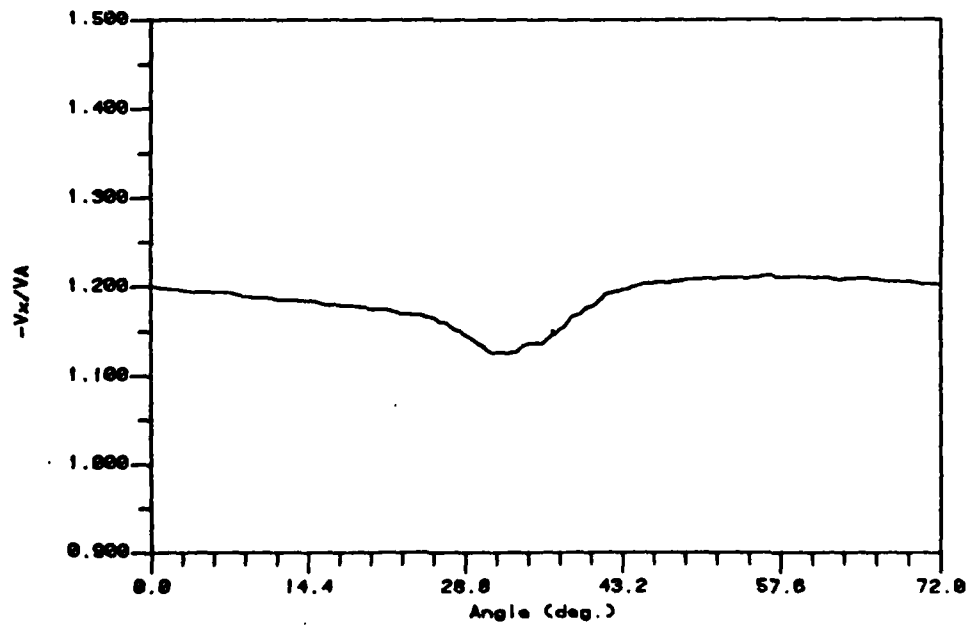


Figure 3-7a Field Point Velocity (Axial component)
Prop. 4381 at $x=-0.333R$, $r=0.300R$ at Design J

-100-

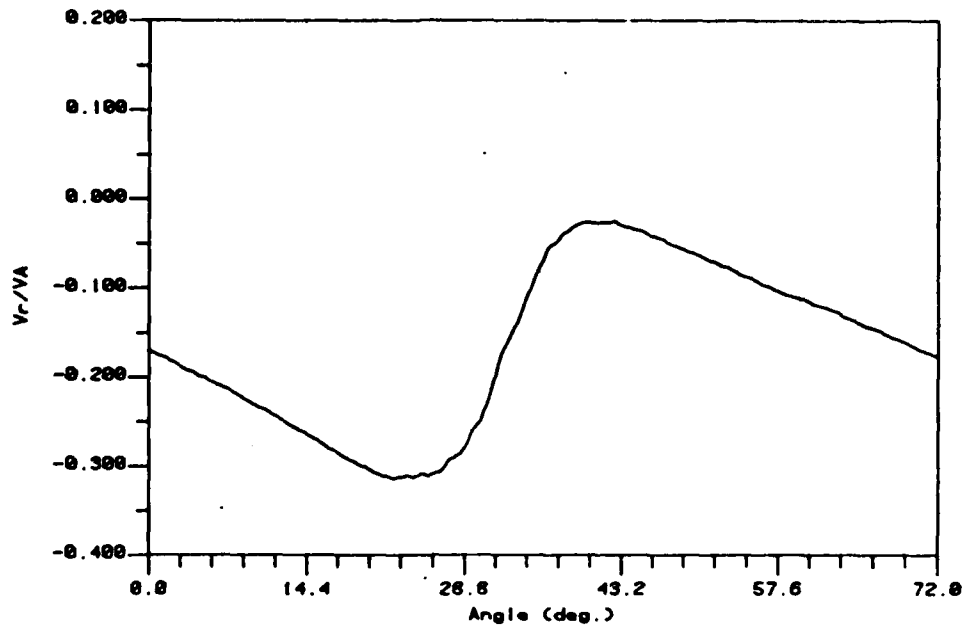


Figure 3-7b Field Point Velocity (Radial component)
Prop. 4381 at $x=-0.333R$, $r=0.300R$ at Design J

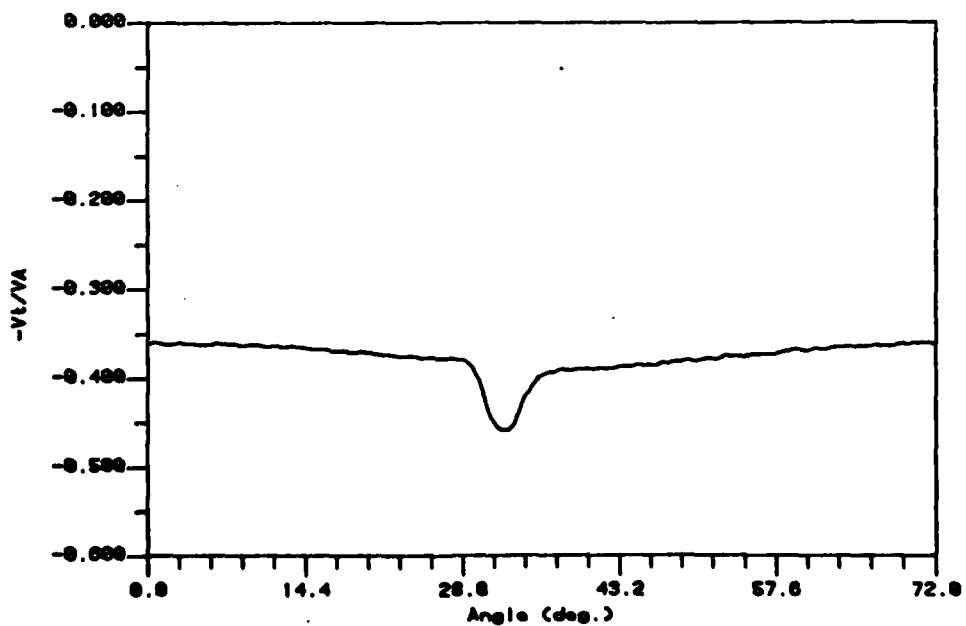


Figure 3-7c Field Point Velocity (Tangential component)
Prop. 4381 at $x=-0.333R$, $r=0.300R$ at Design J

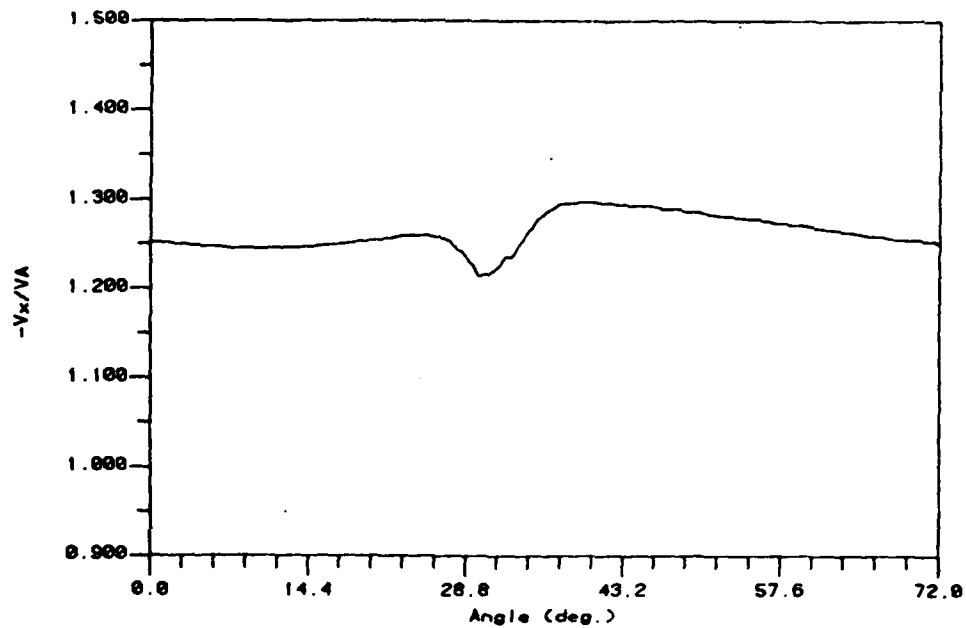


Figure 3-8a Field Point Velocity (Axial component)
Prop. 4381 at $x=-0.333R$, $r=0.400R$ at Design J

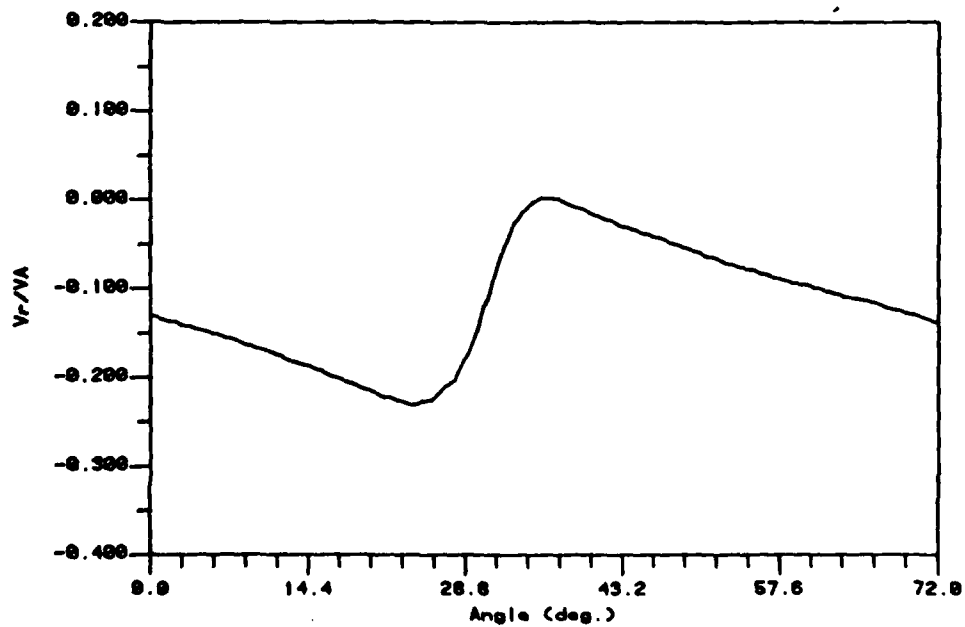


Figure 3-8b Field Point Velocity (Radial component)
Prop. 4381 at $x=-0.333R$, $r=0.400R$ at Design J

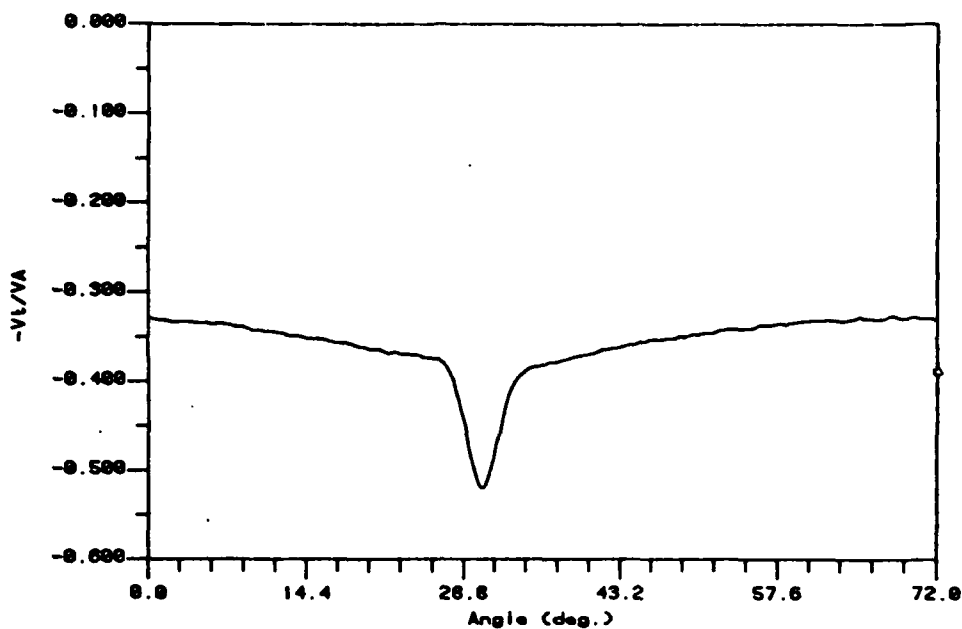


Figure 3-8c Field Point Velocity (Tangential component)
Prop. 4381 at $x=-0.333R$, $r=0.400R$ at Design J

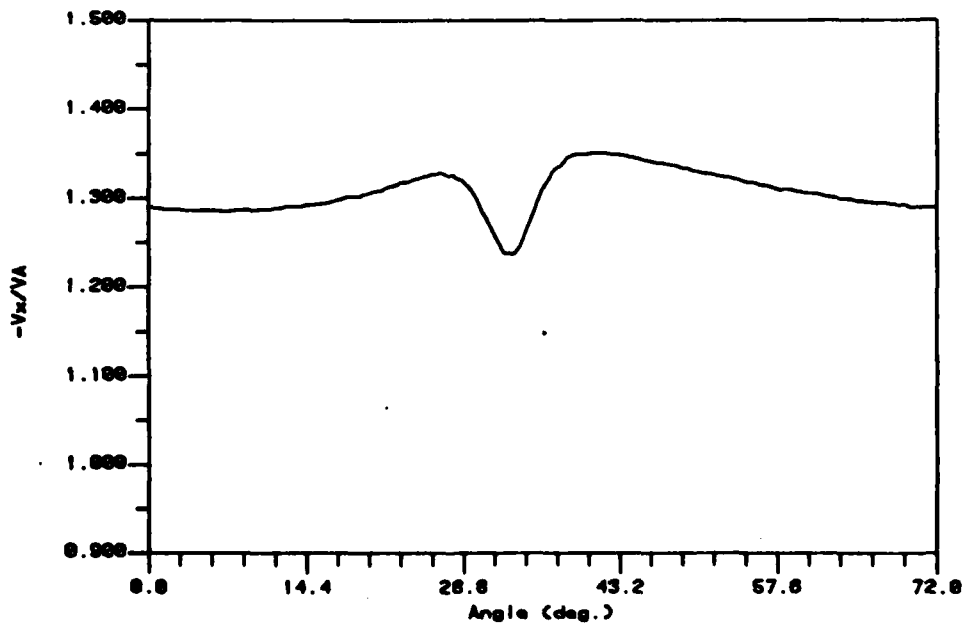


Figure 3-9a Field Point Velocity (Axial component)
Prop. 4381 at $x=-0.333R$, $r=0.500R$ at Design J

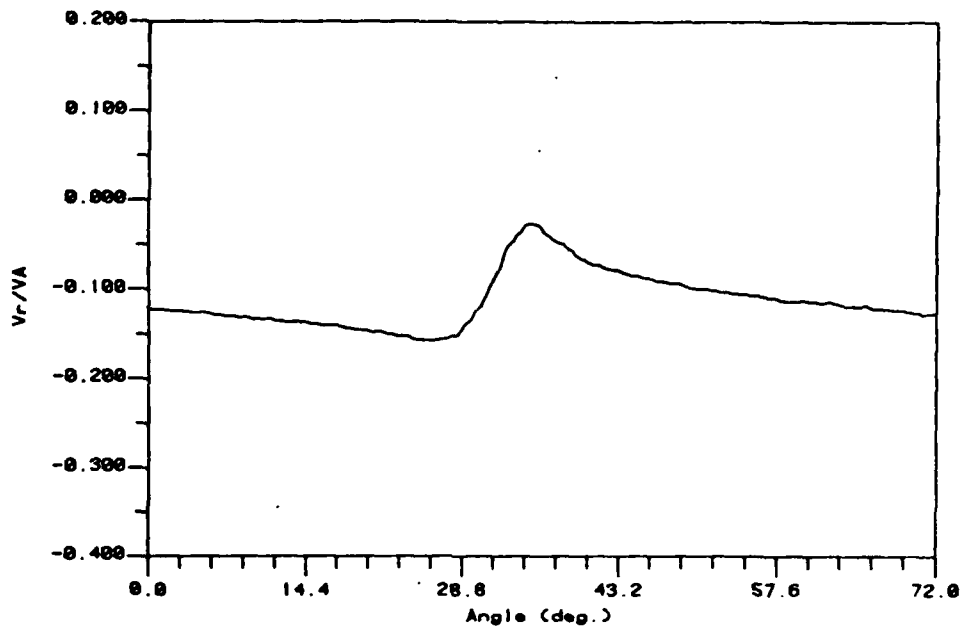


Figure 3-9b Field Point Velocity (Radial component)
Prop. 4381 at $x=-0.333R$, $r=0.500R$ at Design J

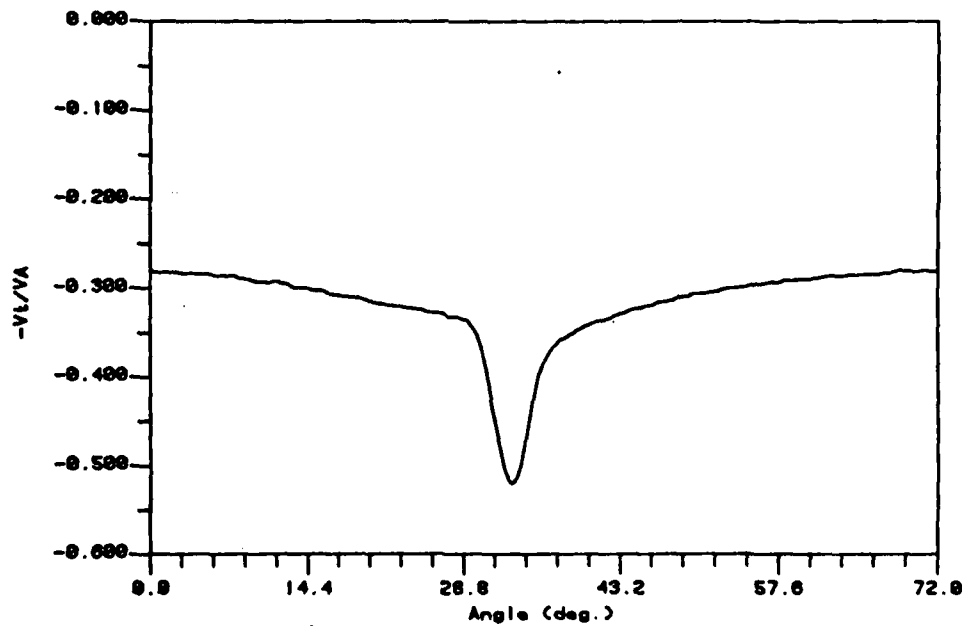


Figure 3-9c Field Point Velocity (Tangential component)
Prop. 4381 at $x=-0.333R$, $r=0.500R$ at design J

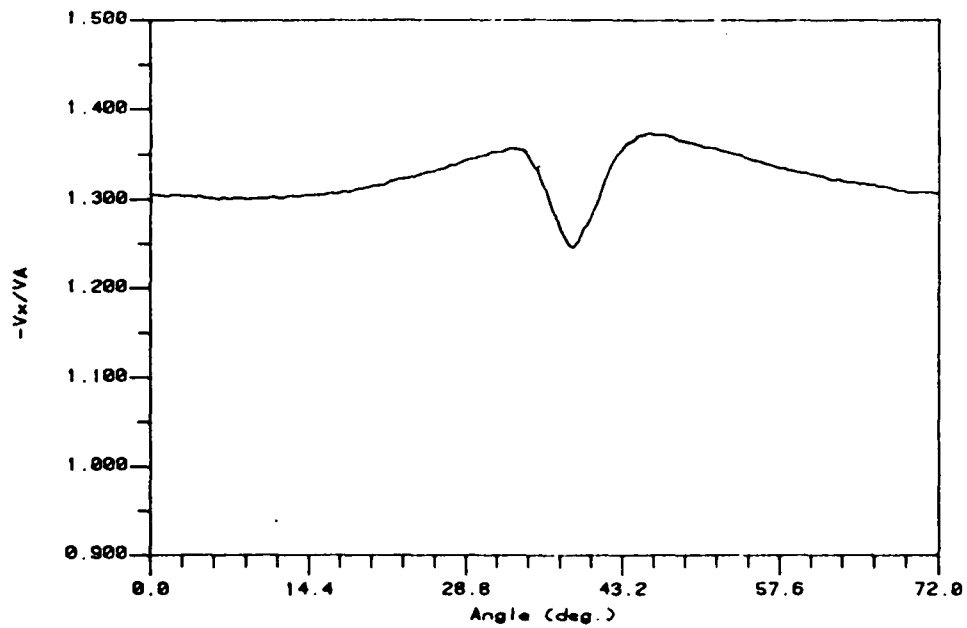


Figure 3-10a Field Point Velocity (Axial component)
Prop. 4381 at $x=-0.333R$, $r=0.600R$ at Design J

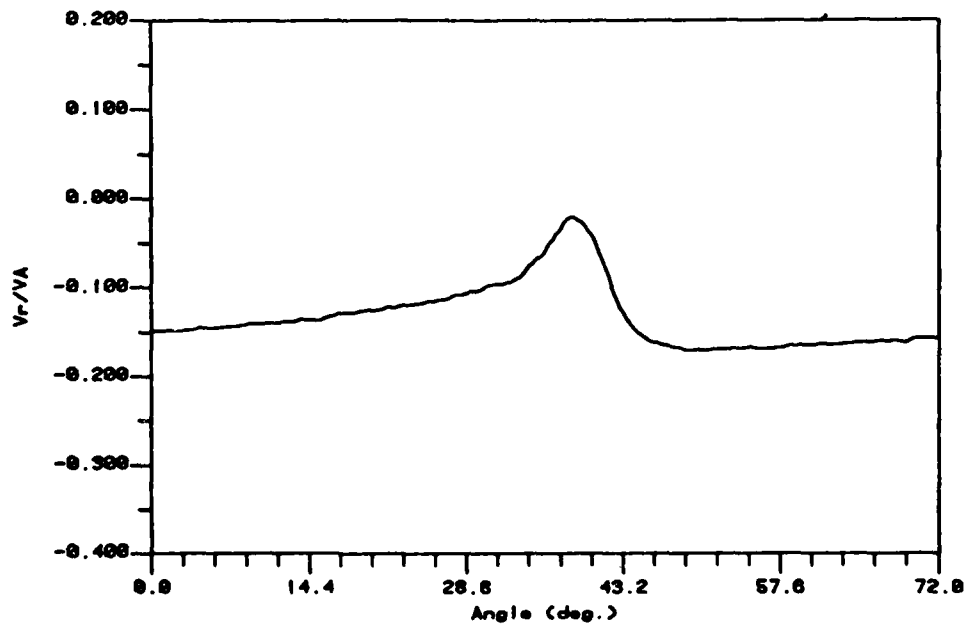


Figure 3-10b Field Point Velocity (Radial component)
Prop. 4381 at $x=-0.333R$, $r=0.600R$ at design J

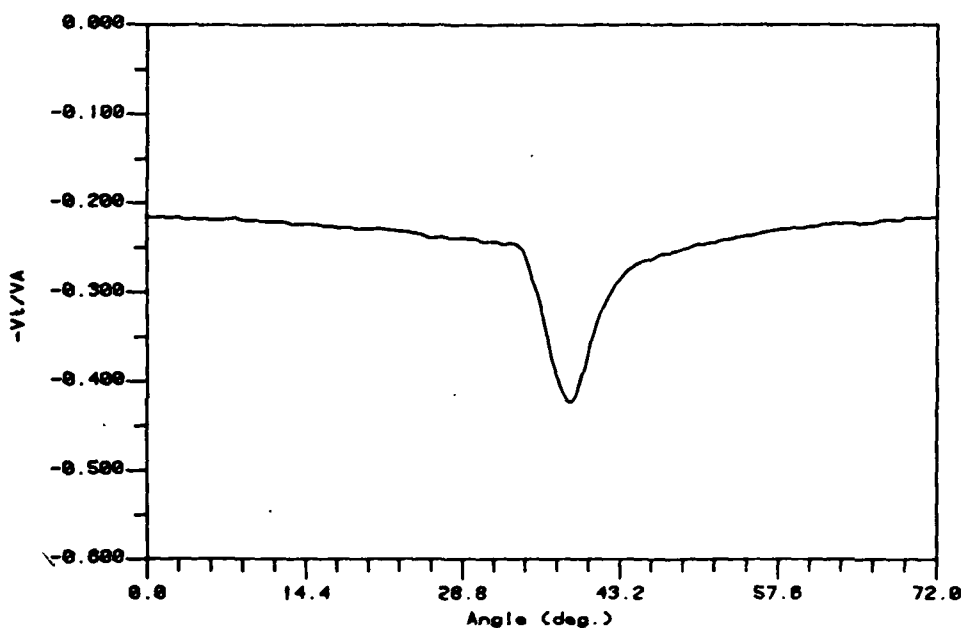


Figure 3-10c Field Point Velocity (Tangential component)
Prop. 4381 at $x=-0.333R$, $r=0.600R$ at design J

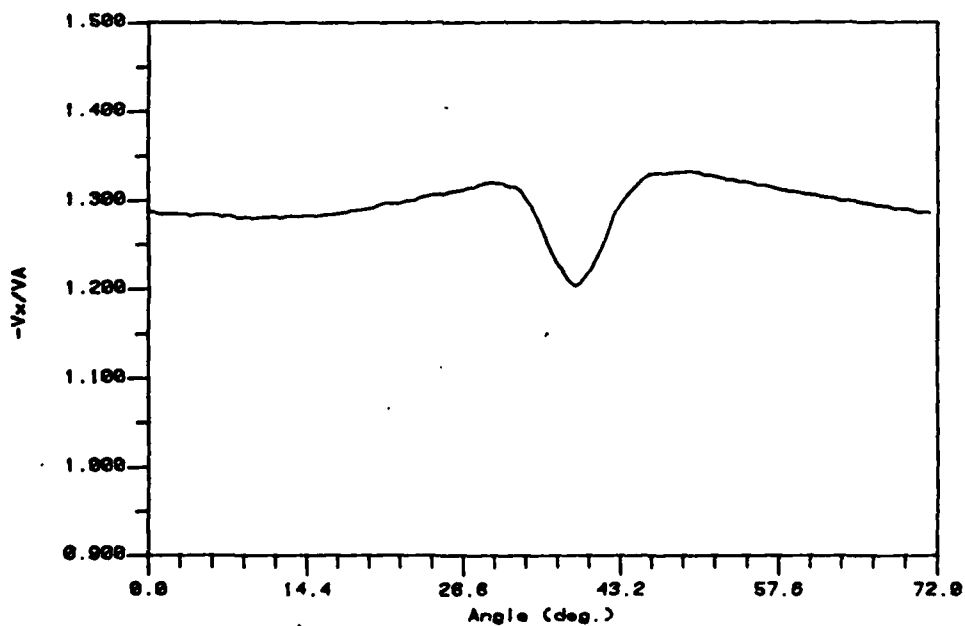


Figure 3-11a Field Point Velocity (Axial component)
Prop. 4381 at $x=-0.333R$, $r=0.700R$ at Design J

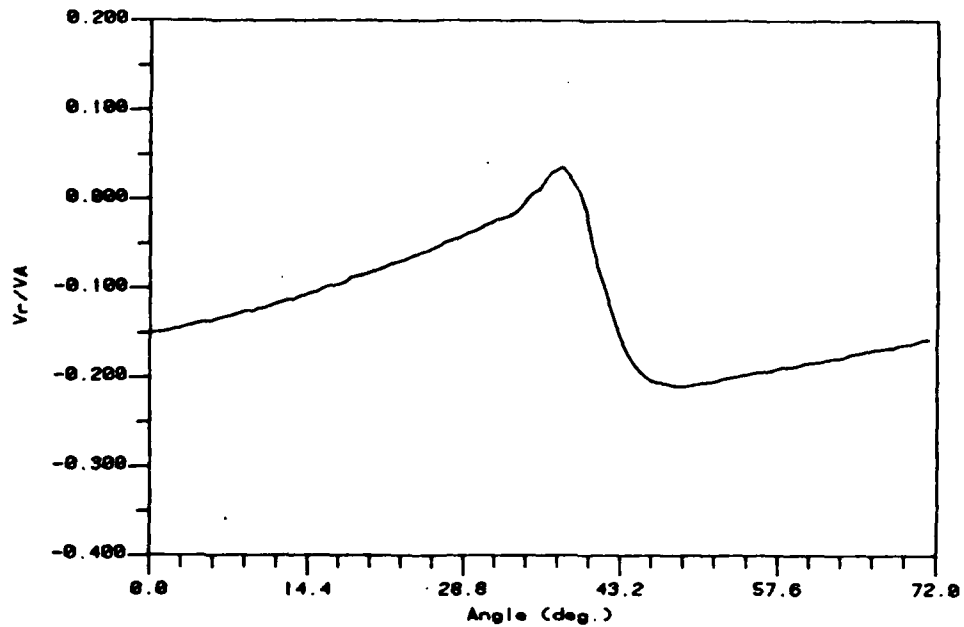


Figure 3-11b Field Point Velocity (Radial component)
Prop. 4381 at $x=-0.333R$, $r=0.700R$ at Design J

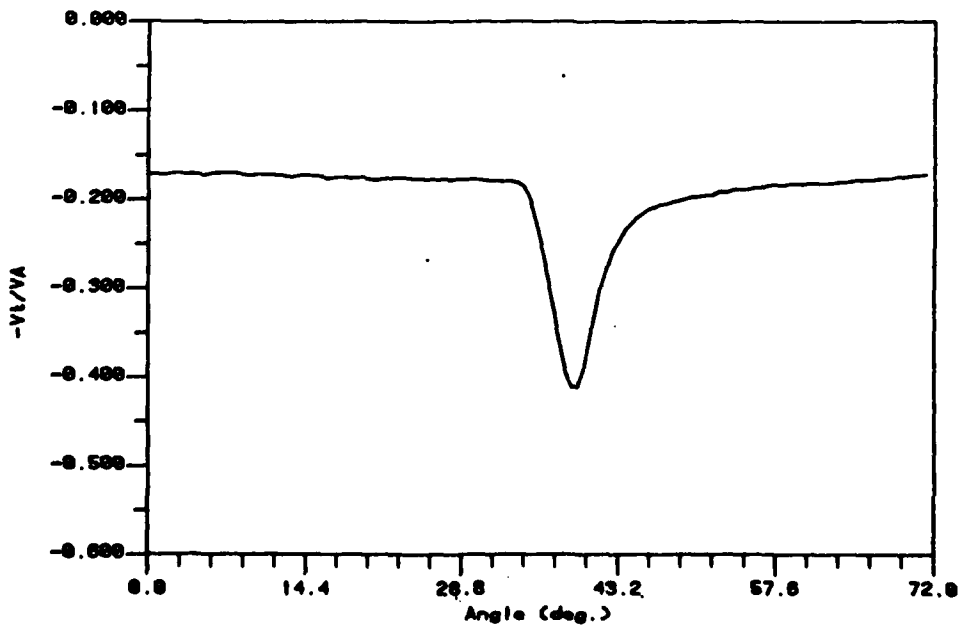


Figure 3-11c Field Point Velocity (Tangential component)
Prop. 4381 at $x=-0.333R$, $r=0.700R$ at Design J

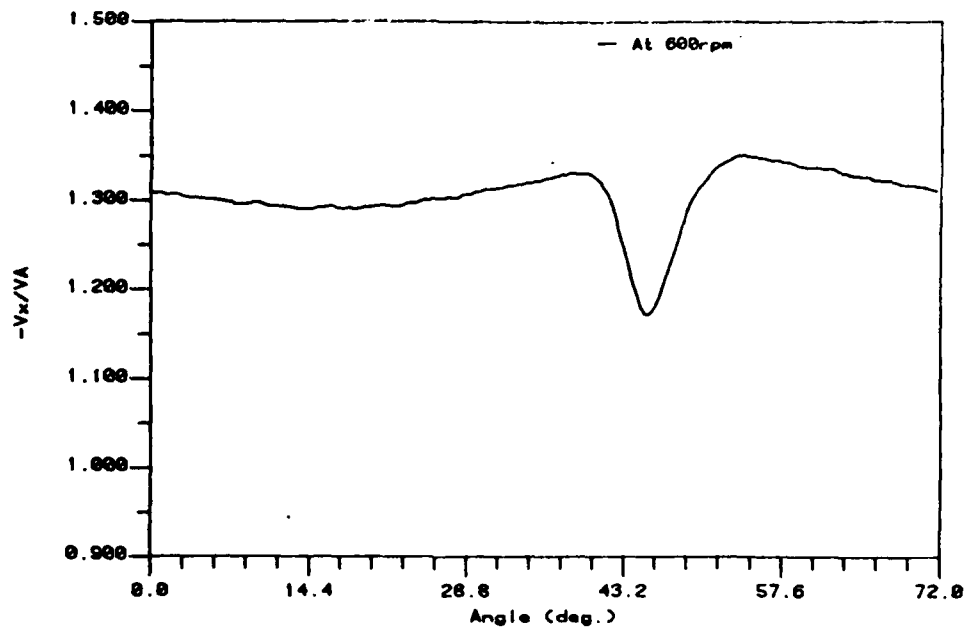


Figure 3-12a Field Point Velocity (Axial component)
Prop. 4381 at $x=-0.333R$, $r=0.700R$ at Design J

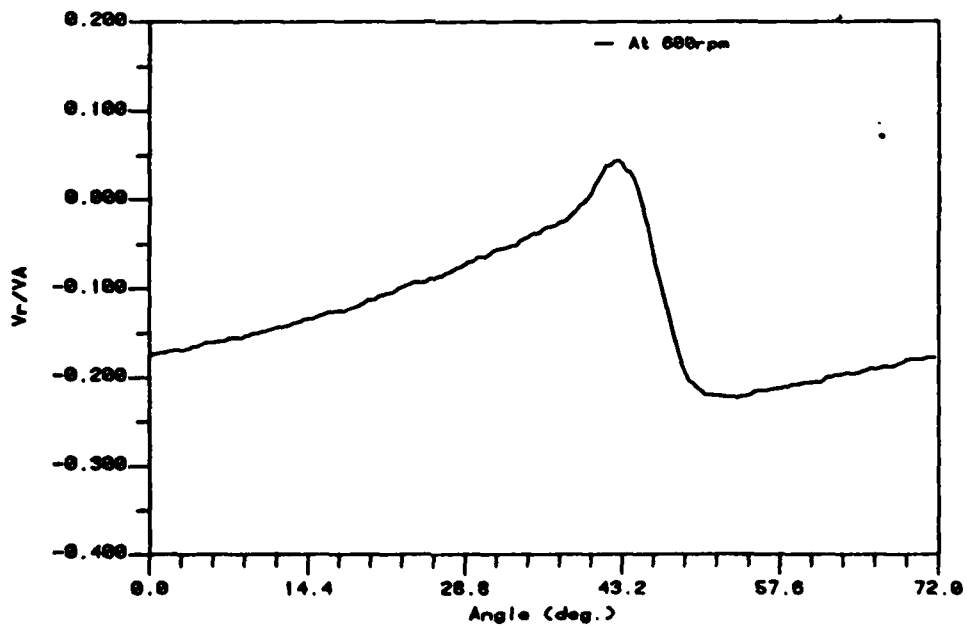


Figure 3-12b Field Point Velocity (Radial component)
Prop. 4381 at $x=-0.333R$, $r=0.700R$ at Design J

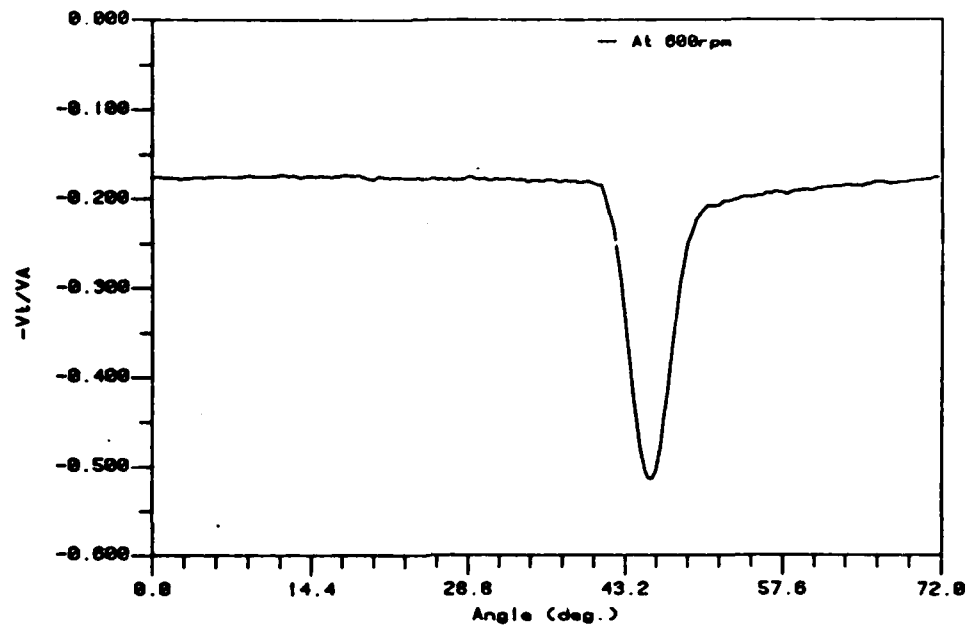


Figure 3-12c Field Point Velocity (Tangential component)
Prop. 4381 at $x=-0.333R$, $r=0.700R$ at Design J

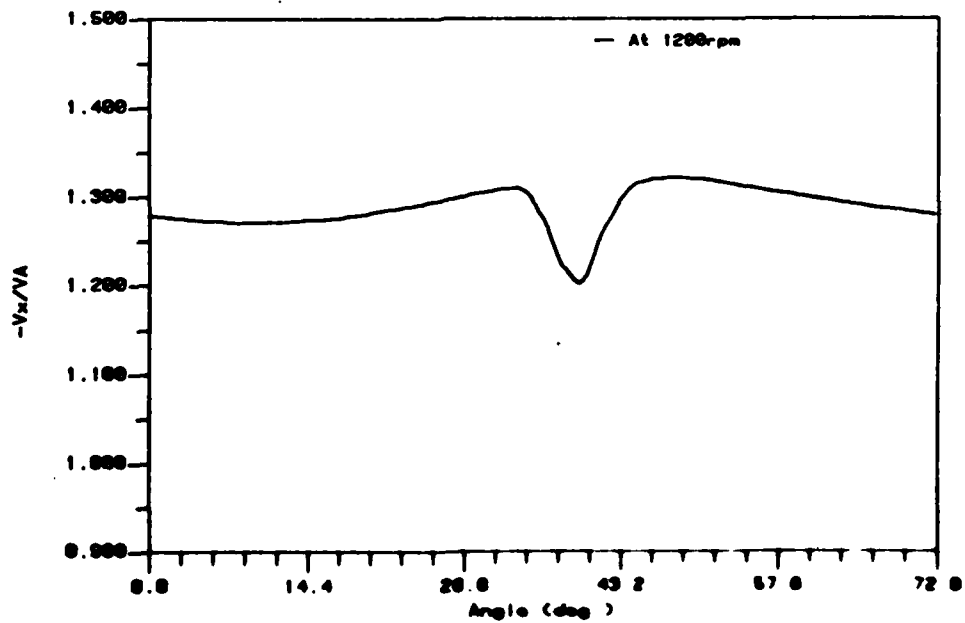


Figure 3-13a Field Point Velocity (Axial component)
Prop. 4381 at $x=-0.333R$, $r=0.700R$ at Design J

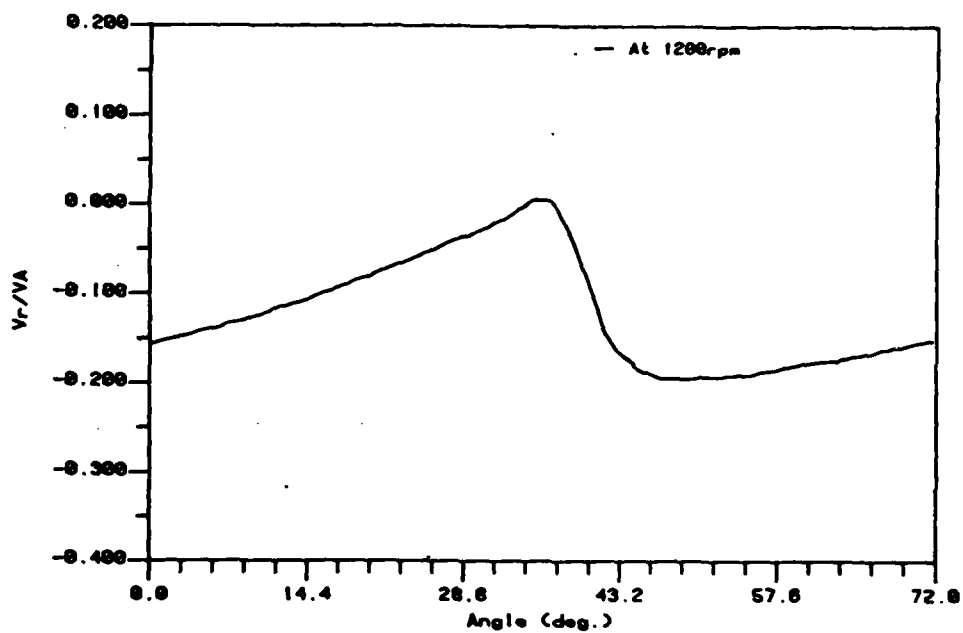


Figure 3-13b Field Point Velocity (Radial component)
Prop. 4381 at $x=-0.333R$, $r=0.700R$ at Design J

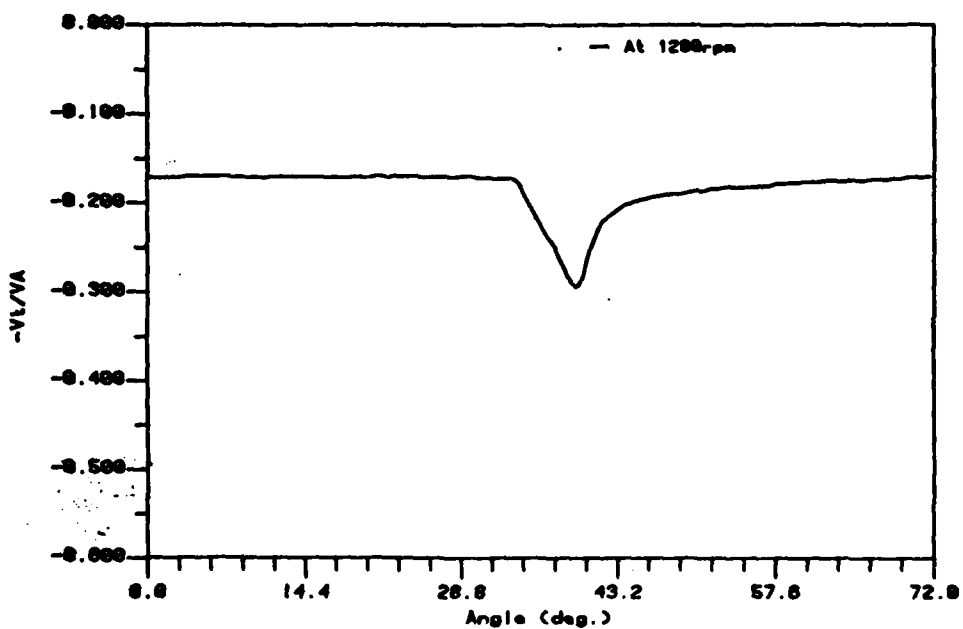


Figure 3-13c Field Point Velocity (Tangential component)
Prop. 4381 at $x=-0.333R$, $r=0.700R$ at Design J

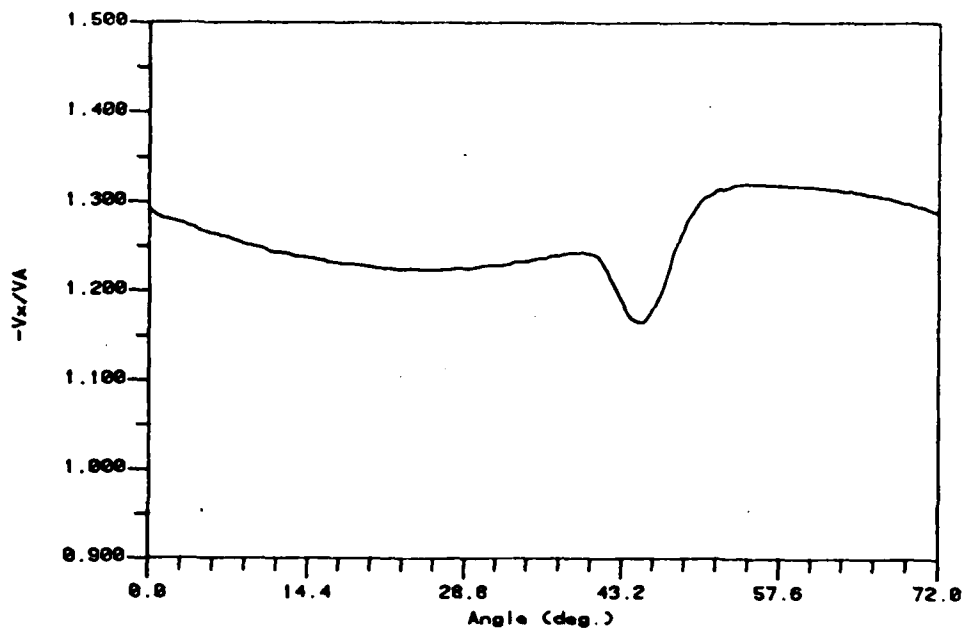


Figure 3-14a Field Point Velocity (Axial component)
Prop. 4381 at $x=-0.333R$, $r=0.800R$ at Design J

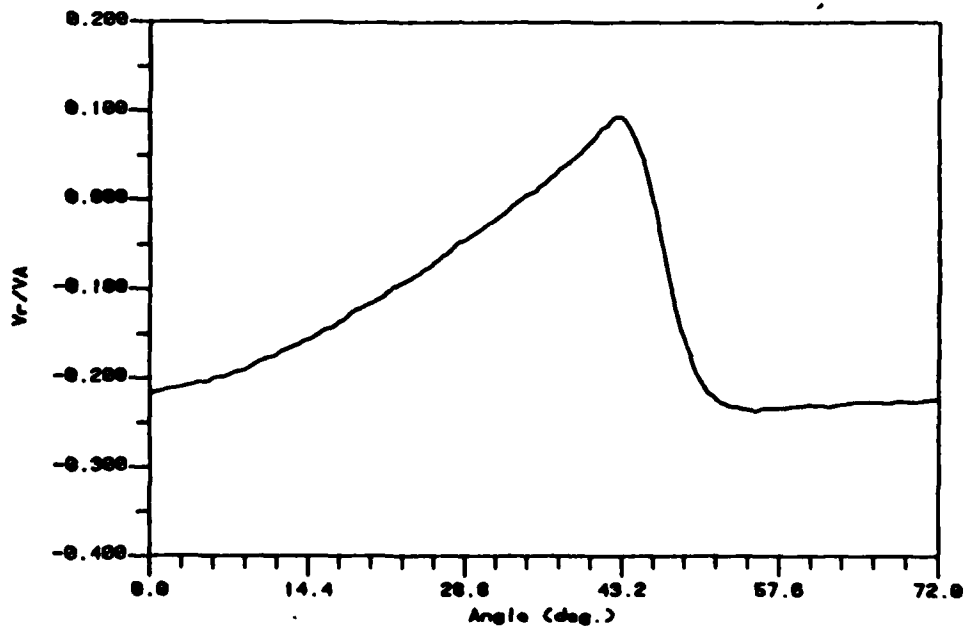


Figure 3-14b Field Point Velocity (Radial component)
Prop. 4381 at $x=-0.333R$, $r=0.800R$ at Design J

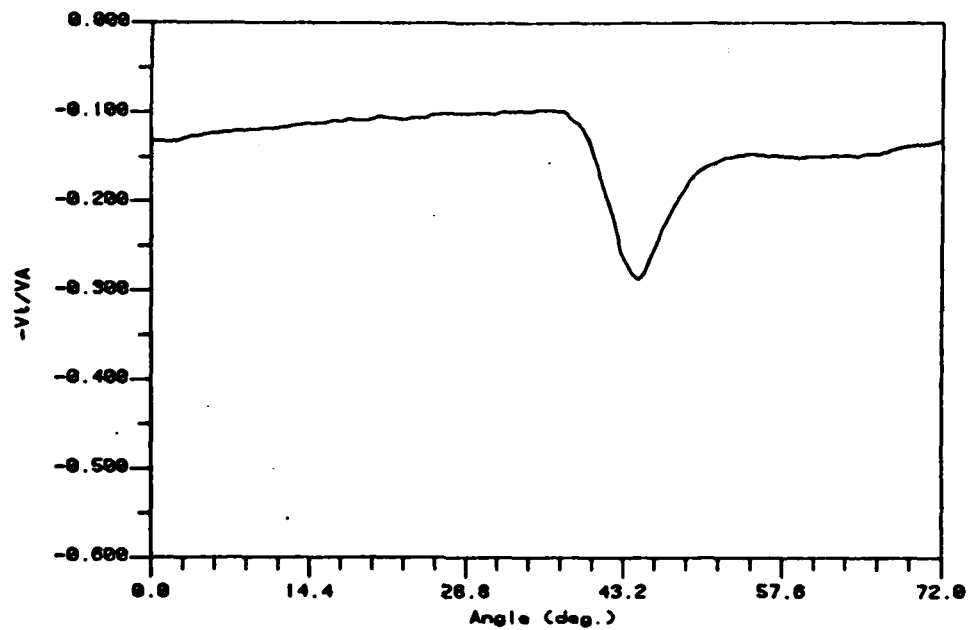


Figure 3-14c Field Point Velocity (Tangential component)
Prop. 4381 at $x=-0.333R$, $r=0.800R$ at design J

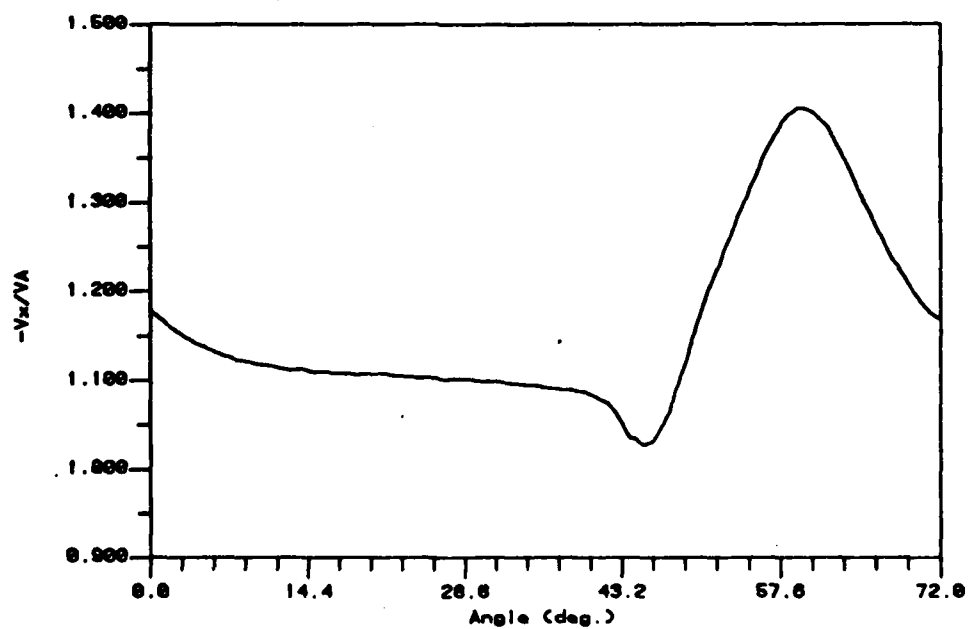


Figure 3-15a Field Point Velocity (Axial component)
Prop. 4381 at $x=-0.333R$, $r=0.875R$ at Design J

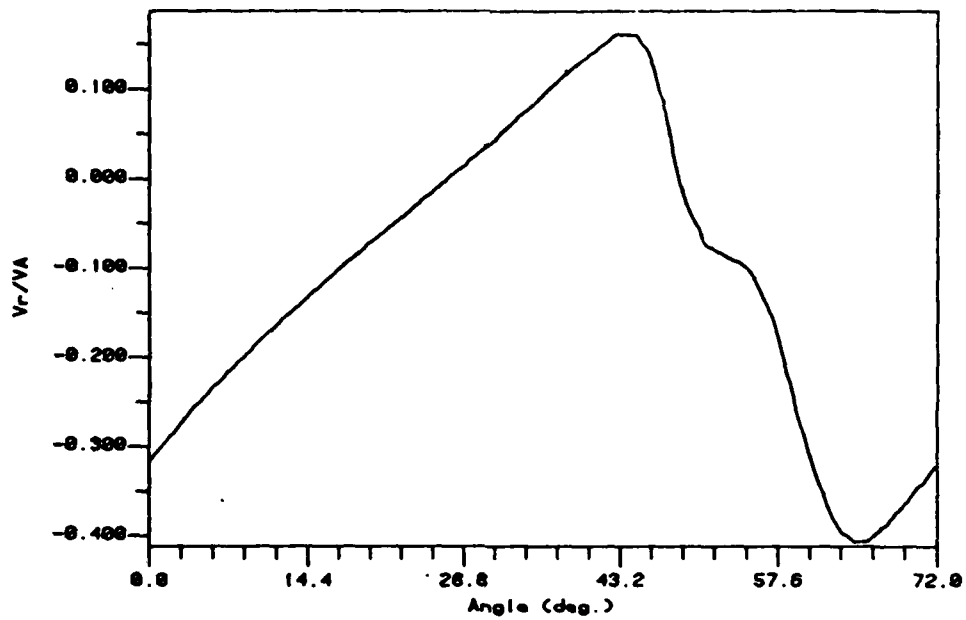


Figure 3-15b Field Point Velocity (Radial component)
Prop. 4381 at $x=-0.333R$, $r=0.875R$ at Design J

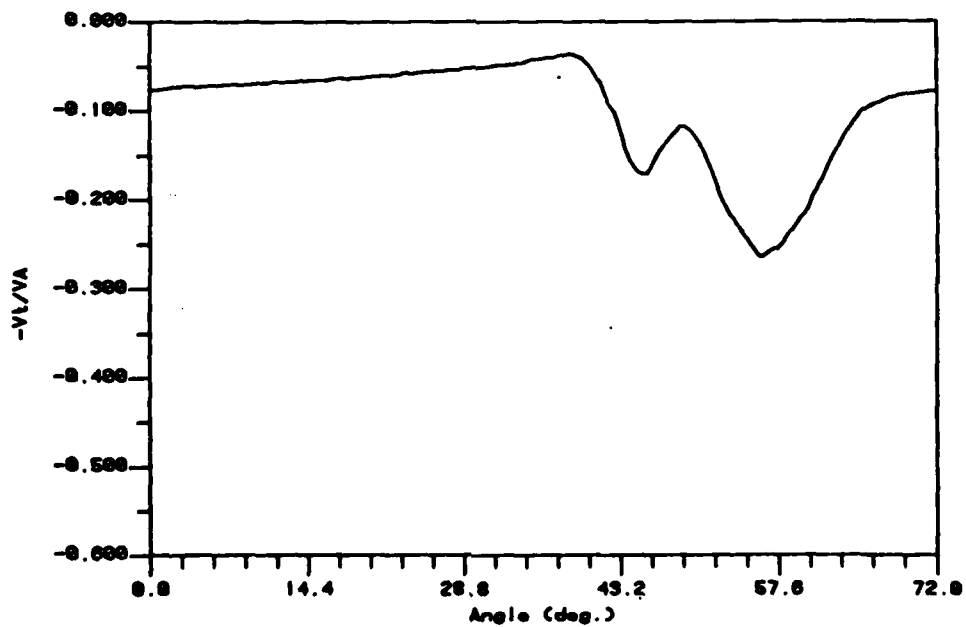


Figure 3-15c Field Point Velocity (Tangential component)
Prop. 4381 at $x=-0.333R$, $r=0.875R$ at Design J

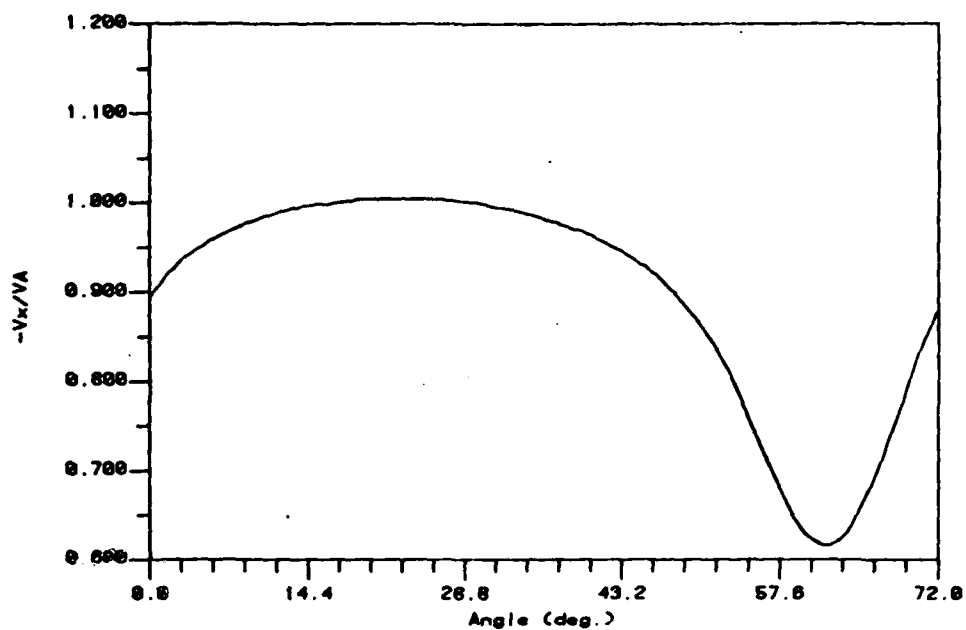


Figure 3-16a Field Point Velocity (Axial component)
Prop. 4381 at $x=-0.333R$, $r=0.950R$ at Design J

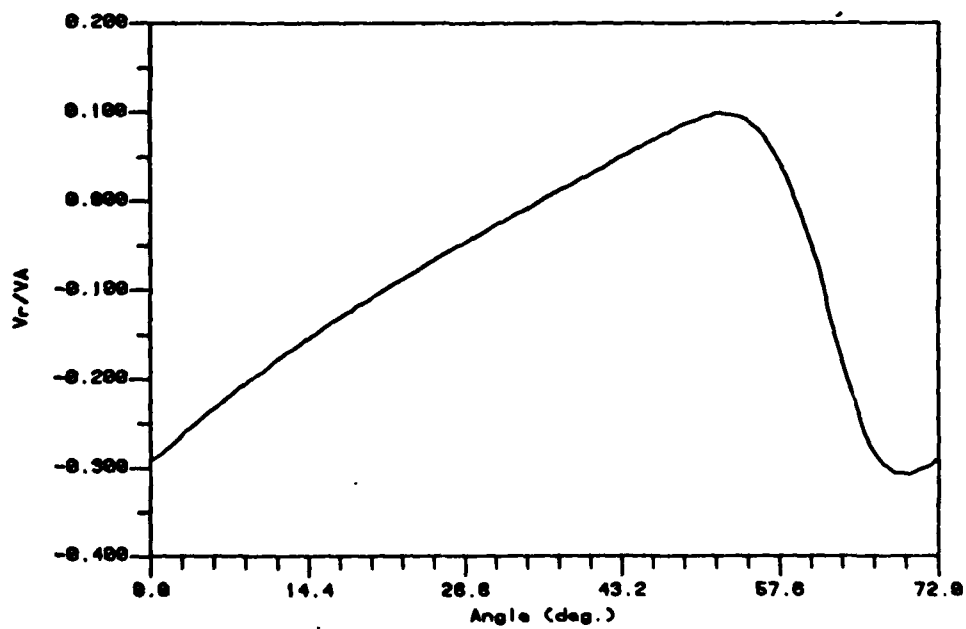


Figure 3-16b Field Point Velocity (Radial component)
Prop. 4381 at $x=-0.333R$, $r=0.950R$ at design J

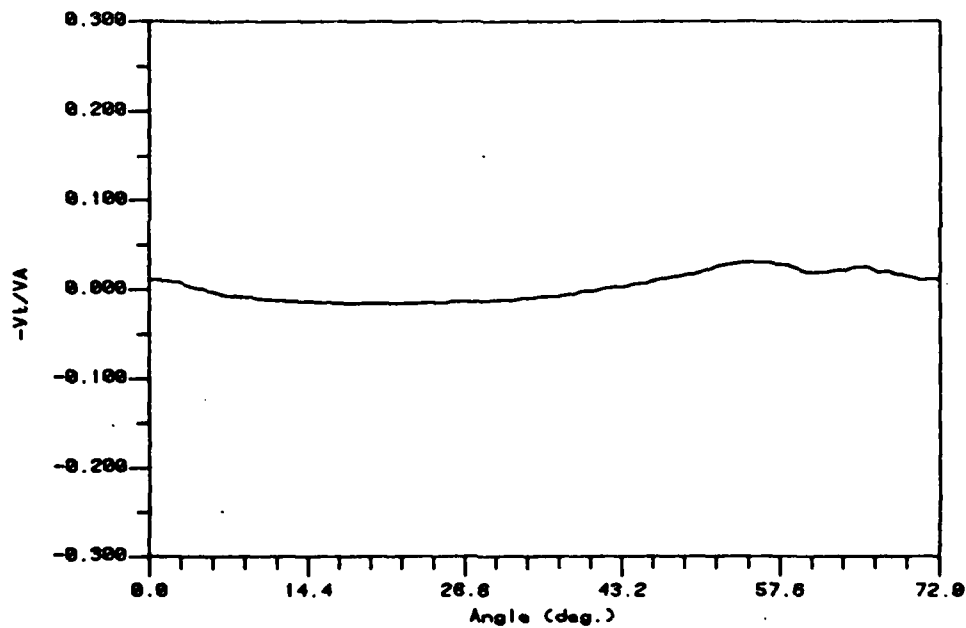


Figure 3-16c Field Point Velocity (Tangential component)
Prop. 4381 at $x=-0.333R$, $r=0.950R$ at Design J

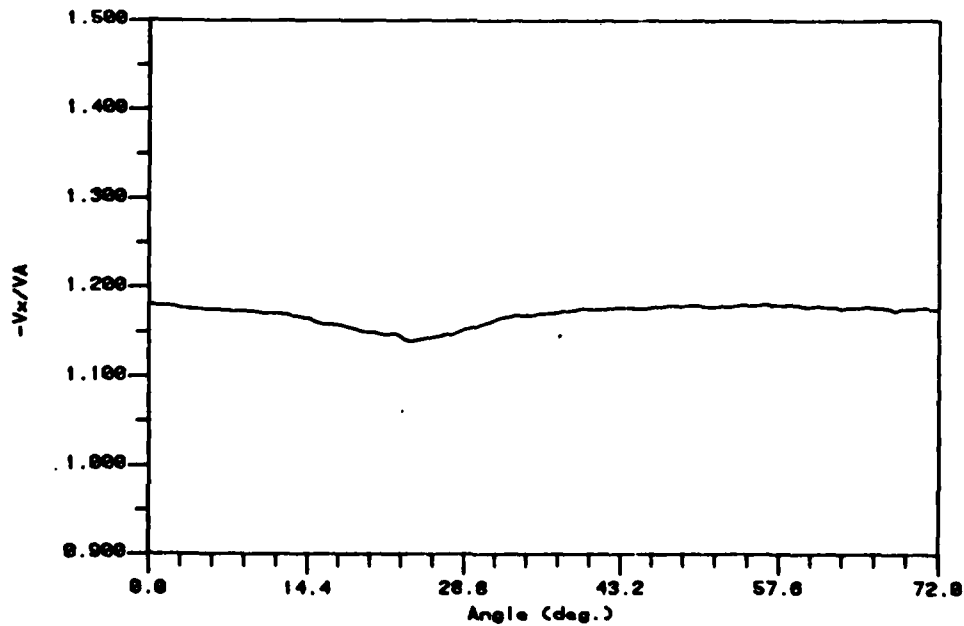


Figure 3-17a Field Point Velocity (Axial component)
Prop. 4383 at $x=-0.488R$, $r=0.300R$ at Design J

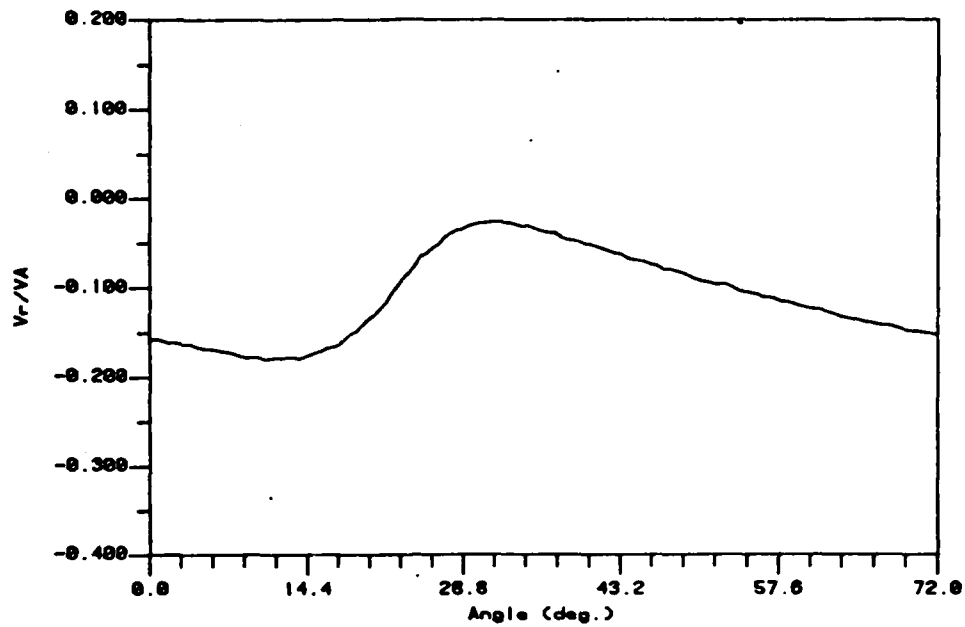


Figure 3-17b Field Point Velocity (Radial component)
Prop. 4383 at $x=-0.488R$, $r=0.300R$ at Design J

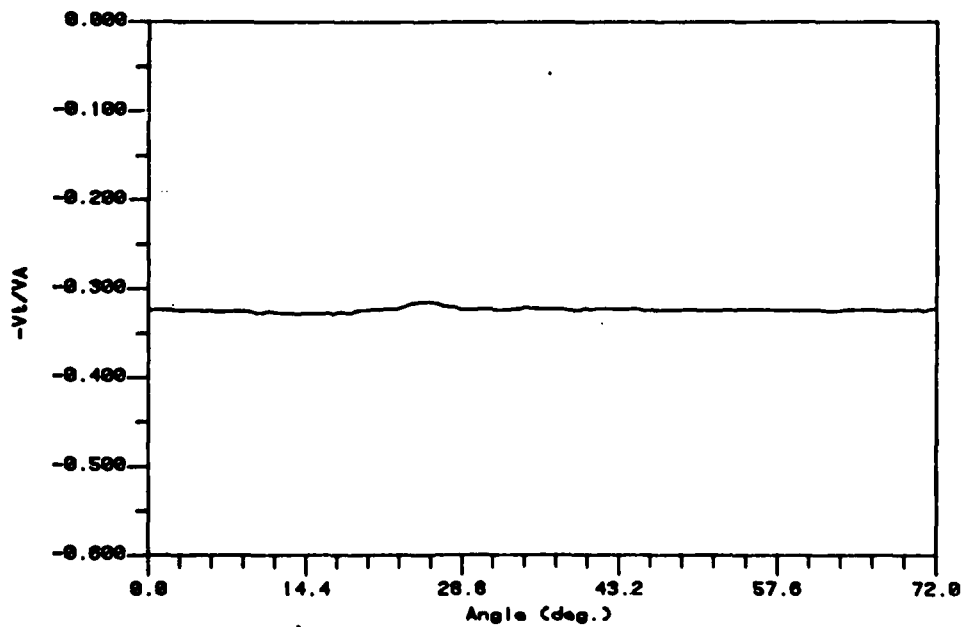


Figure 3-17c Field Point Velocity (Tangential component)
Prop. 4383 at $x=-0.488R$, $r=0.300R$ at Design J

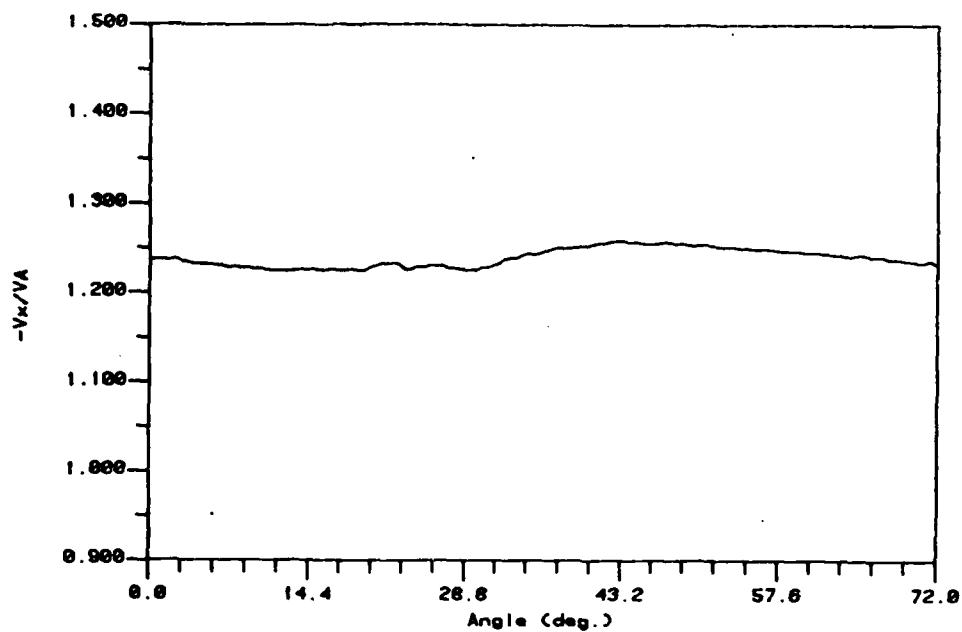


Figure 3-18a Field Point Velocity (Axial component)
Prop. 4383 at $x=-0.488R$, $r=0.400R$ at Design J

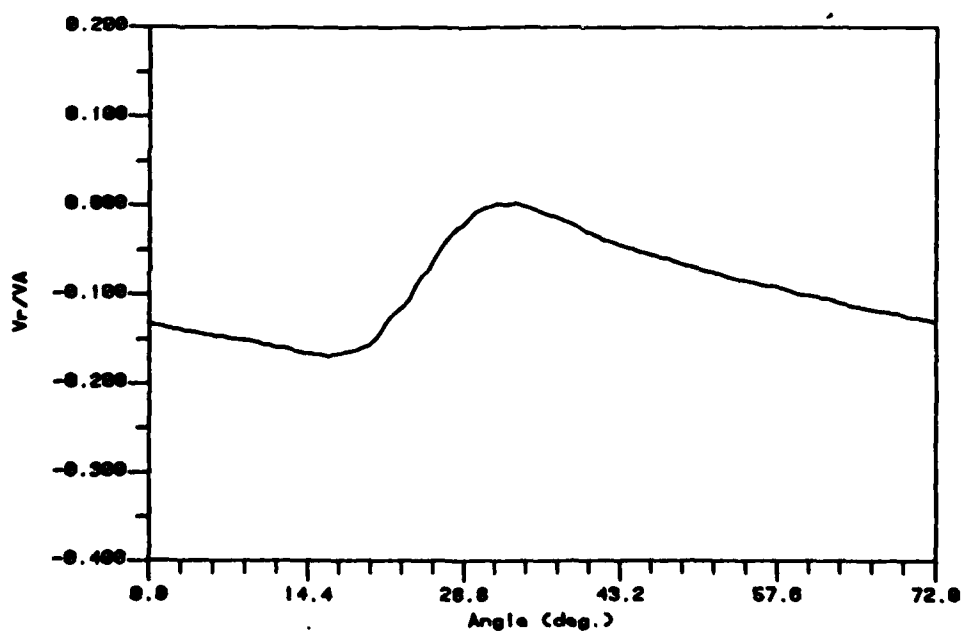


Figure 3-18b Field Point Velocity (Radial component)
Prop. 4383 at $x=-0.488R$, $r=0.400R$ at Design J

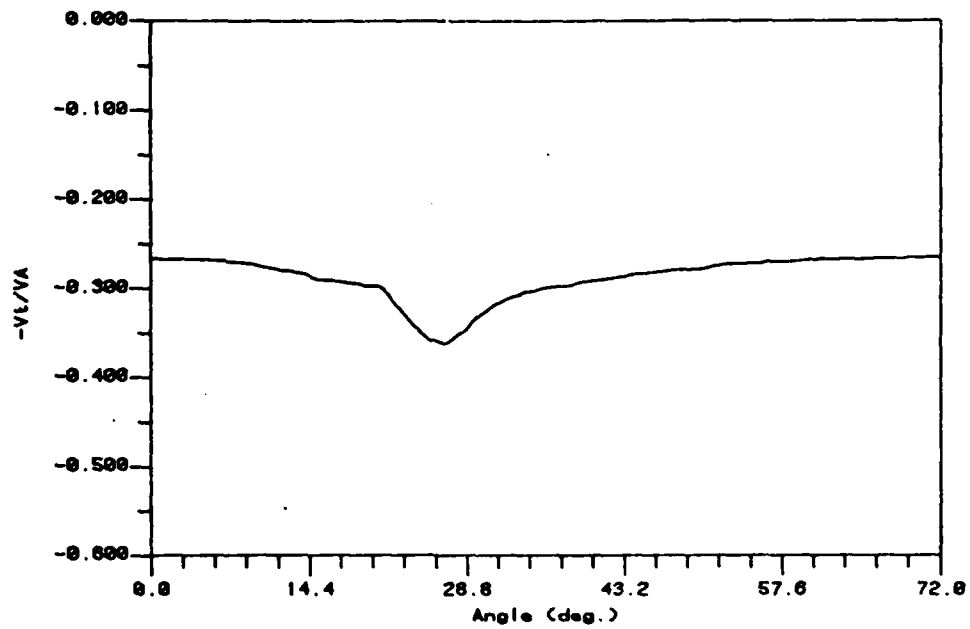


Figure 3-18c Field Point Velocity (Tangential component)
Prop. 4383 at $x=-0.488R$, $r=0.400R$ at Design J

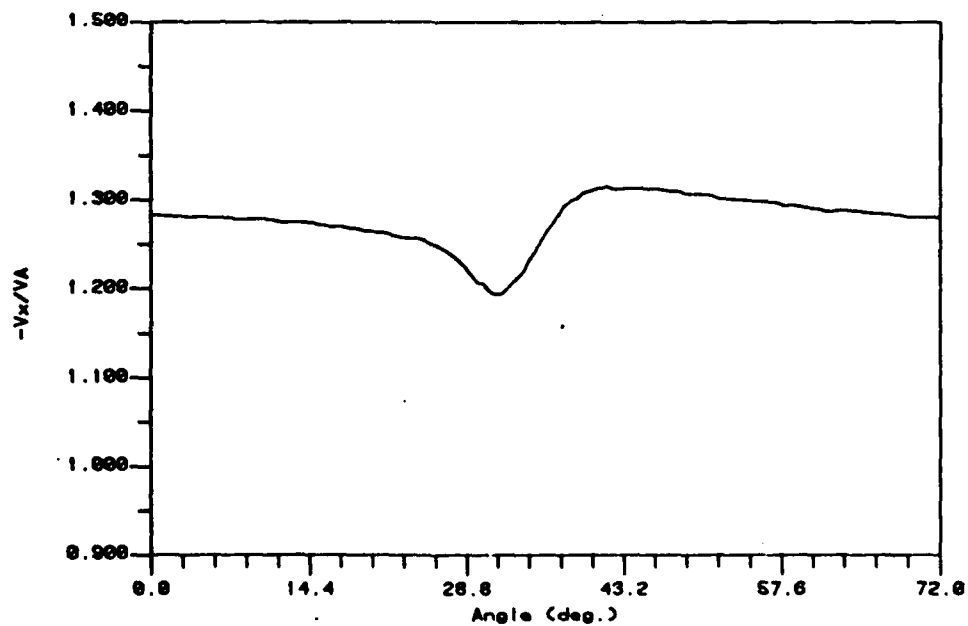


Figure 3-19a Field Point Velocity (Axial component)
Prop. 4383 at $x=-0.488R$, $r=0.500R$ at Design J

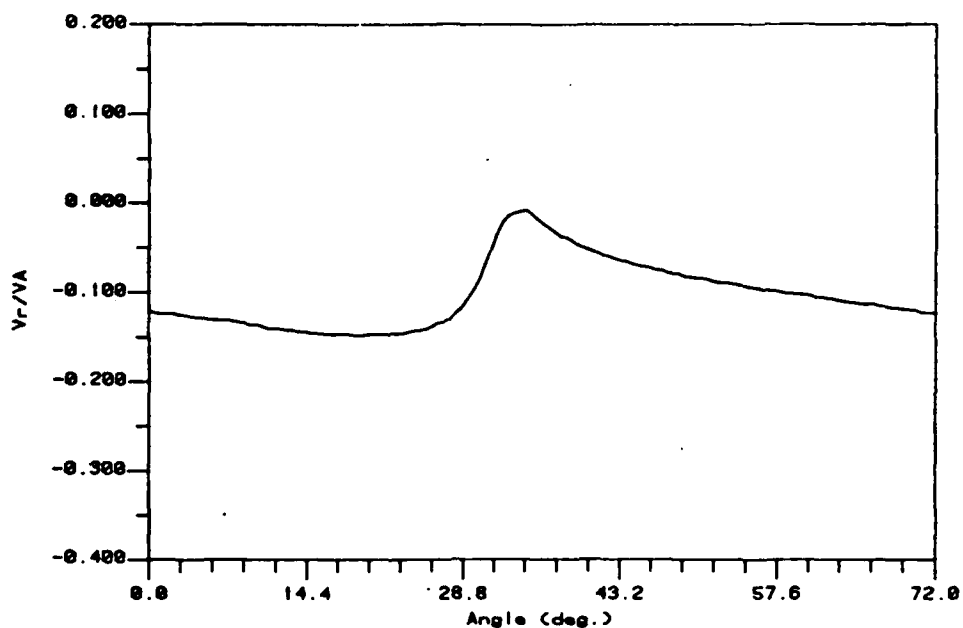


Figure 3-19b Field Point Velocity (Radial component)
Prop. 4383 at $x=-0.488R$, $r=0.500R$ at Design J

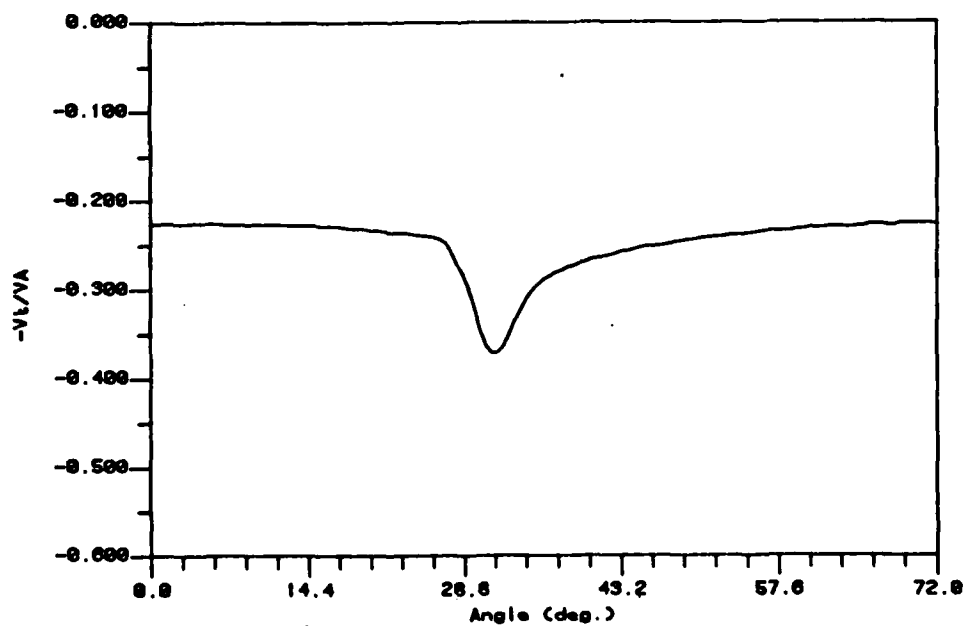


Figure 3-19c Field Point Velocity (Tangential component)
Prop. 4383 at $x=-0.488R$, $r=0.500R$ at design J

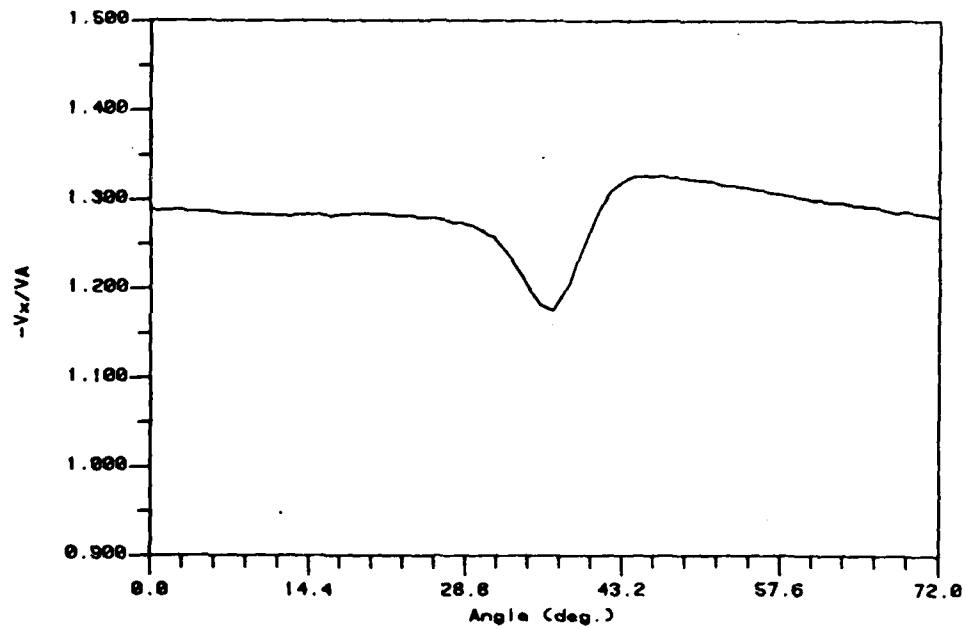


Figure 3-20a Field Point Velocity (Axial component)
Prop. 4383 at $x=-0.488R$, $r=0.600R$ at Design J

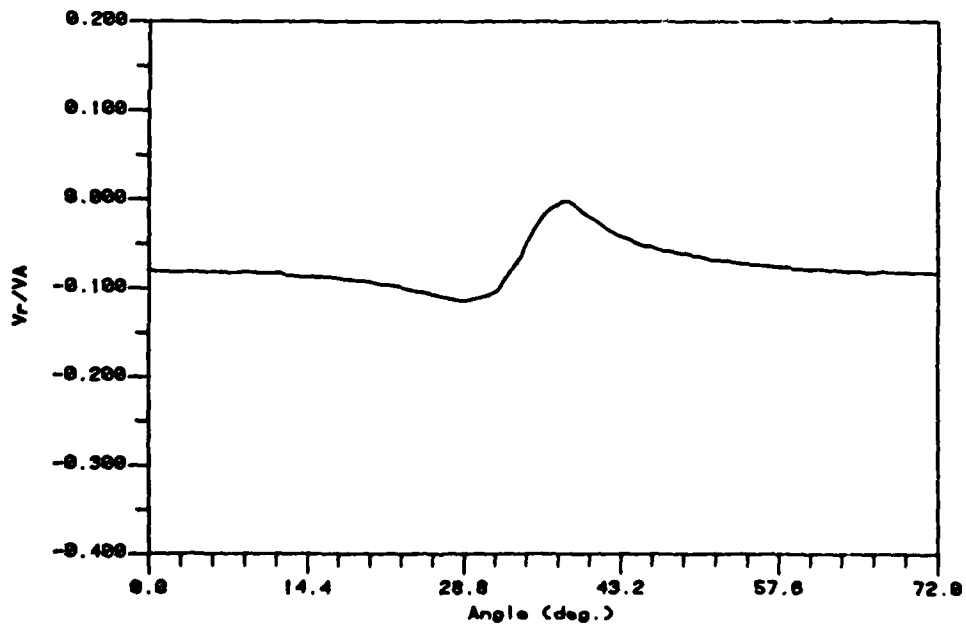


Figure 3-20b Field Point Velocity (Radial component)
Prop. 4383 at $x=-0.488R$, $r=0.600R$ at Design J

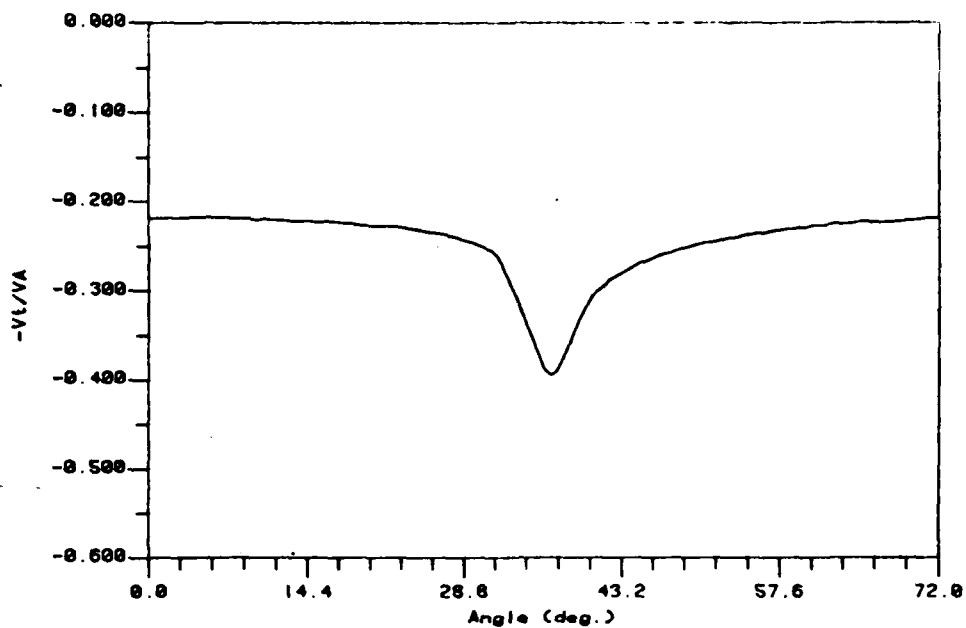


Figure 3-20c Field Point Velocity (Tangential component)
Prop. 4383 at $x=-0.488R$, $r=0.600R$ at Design J

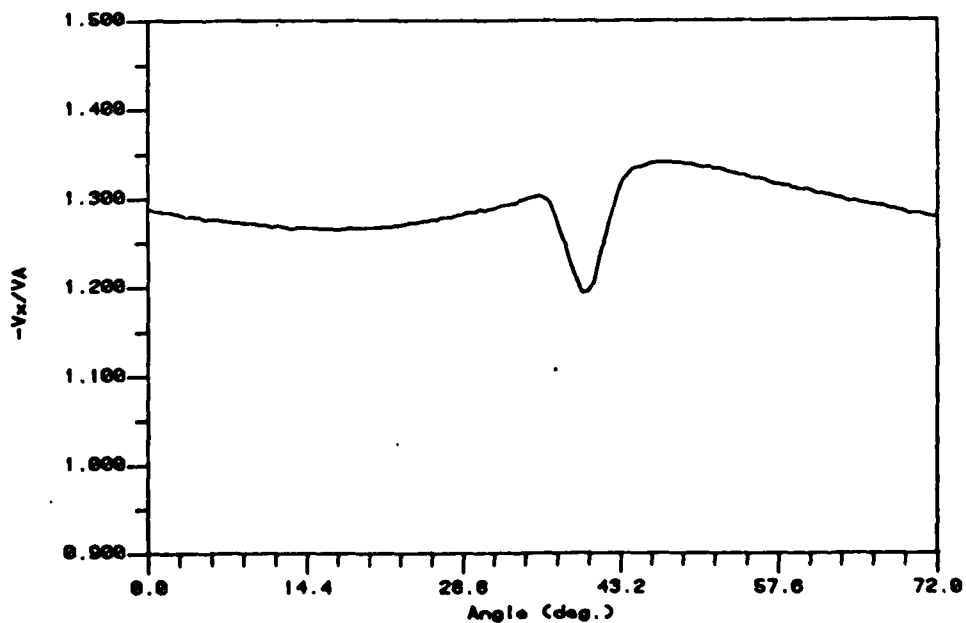


Figure 3-21a Field Point Velocity (Axial component)
Prop. 4383 at $x=-0.488R$, $r=0.700R$ at Design J

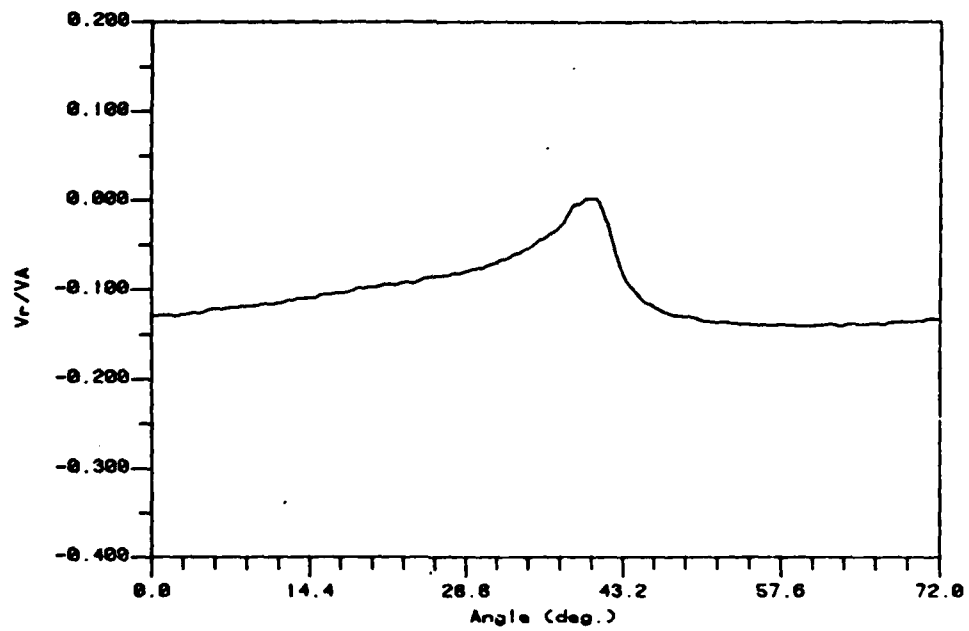


Figure 3-21b Field Point Velocity (Radial component)
Prop. 4383 at $x=-0.488R$, $r=0.700R$ at Design J

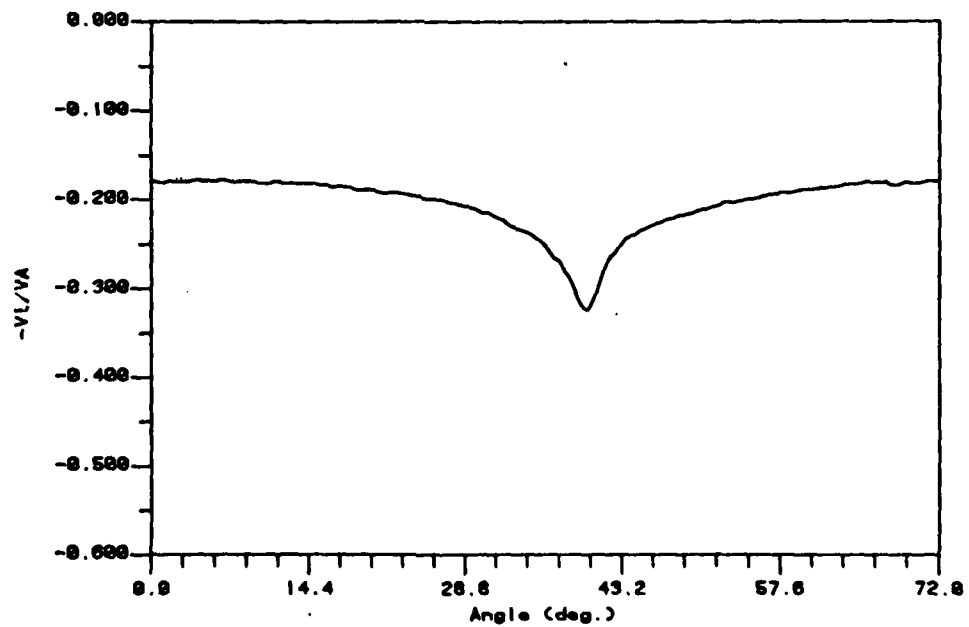


Figure 3-21c Field Point Velocity (Tangential component)
Prop. 4383 at $x=-0.488R$, $r=0.700R$ at Design J

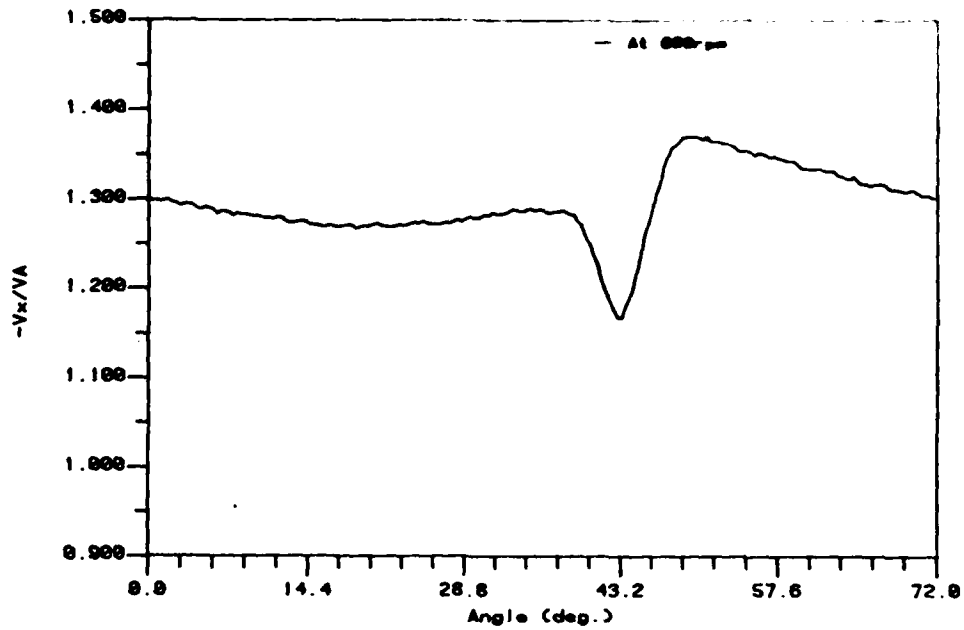


Figure 3-22a Field Point Velocity (Axial component)
Prop. 4383 at $x=-0.488R$, $r=0.700R$ at Design J

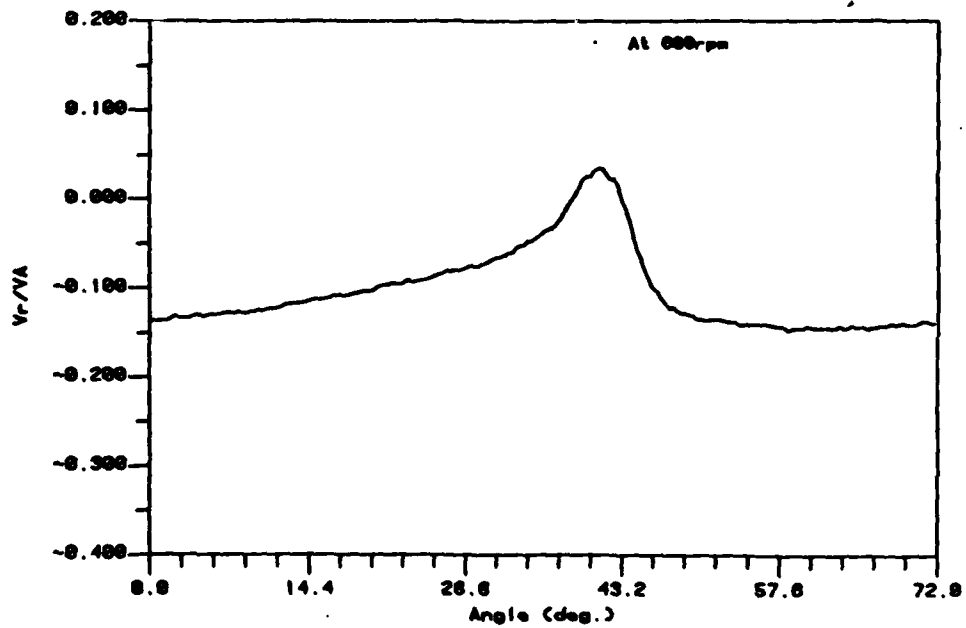


Figure 3-22b Field Point Velocity (Radial component)
Prop. 4383 at $x=-0.488R$, $r=0.700R$ at Design J

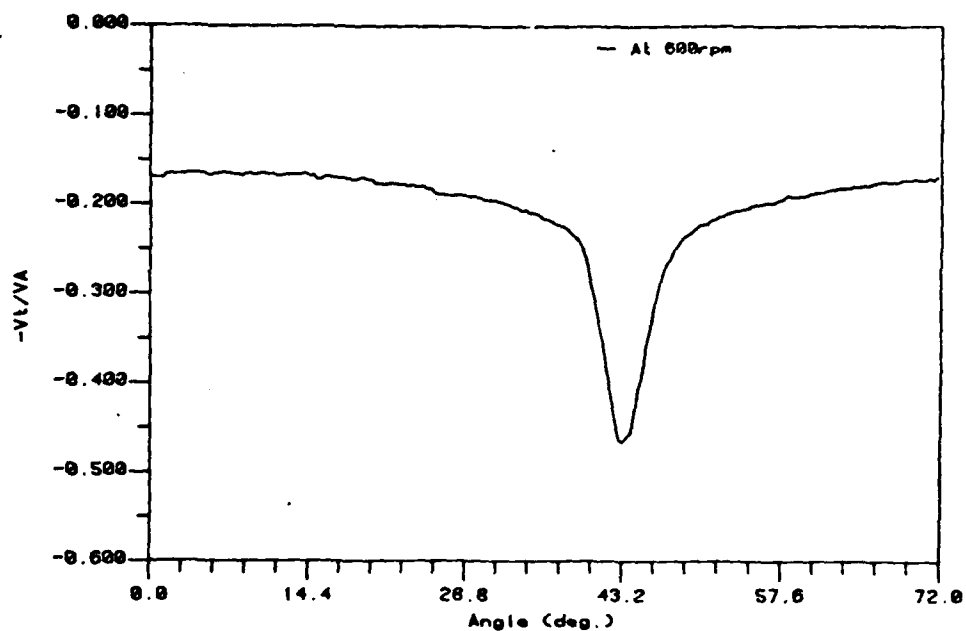


Figure 3-22c Field Point Velocity (Tangential component)
Prop. 4383 at $x=-0.488R$, $r=0.700R$ at Design J

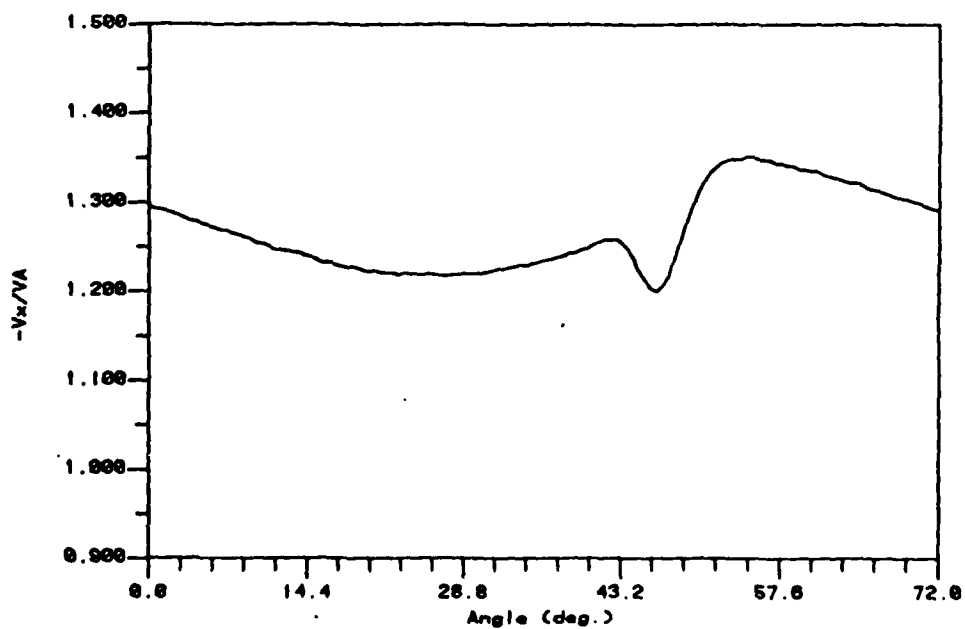


Figure 3-23a Field Point Velocity (Axial component)
Prop. 4383 at $x=-0.488R$, $r=0.800R$ at Design J

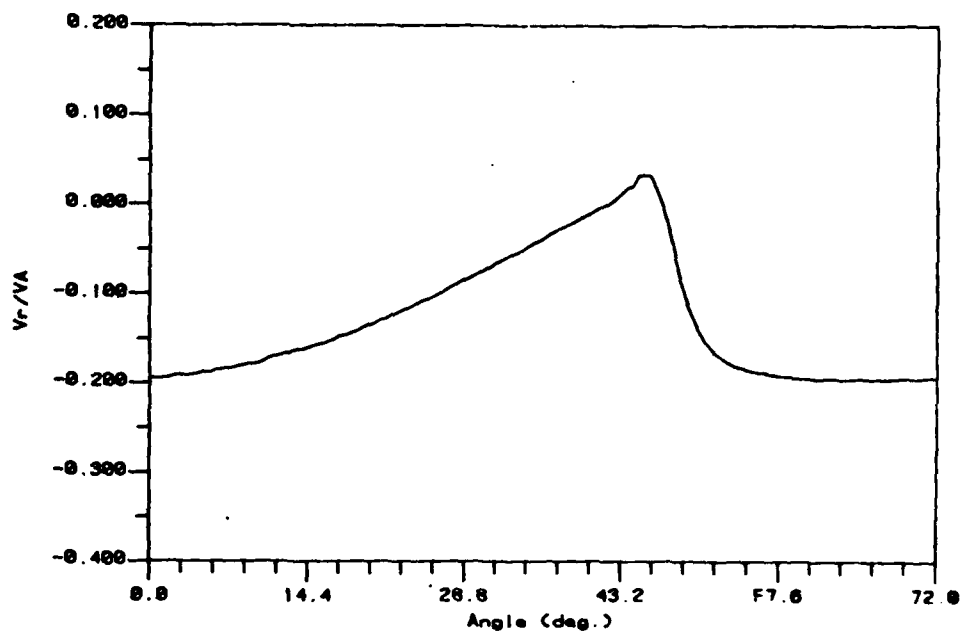


Figure 3-23b Field Point Velocity (Radial component)
Prop. 4383 at $x=-0.488R$, $r=0.800R$ at Design J

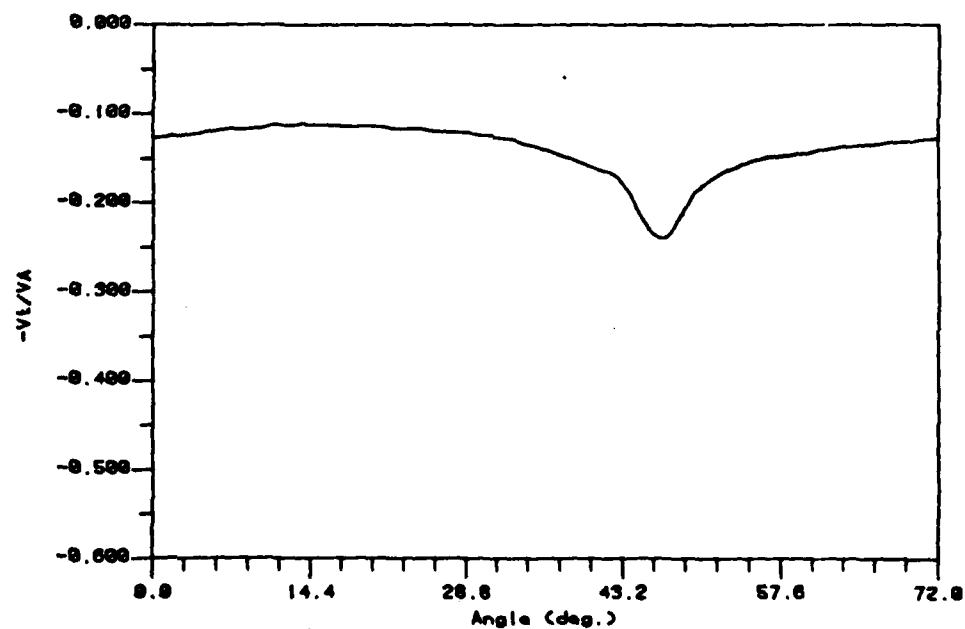


Figure 3-23c Field Point Velocity (Tangential component)
Prop. 4383 at $x=-0.488R$, $r=0.800R$ at Design J

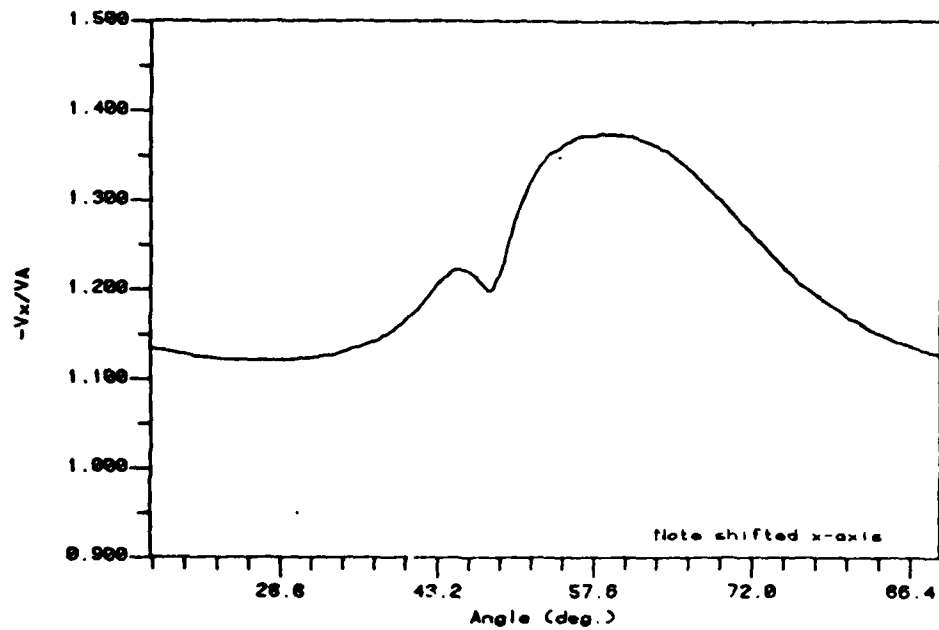


Figure 3-24a Field Point Velocity (Axial component)
Prop. 4383 at $x=-0.488R$, $r=0.875R$ at Design J

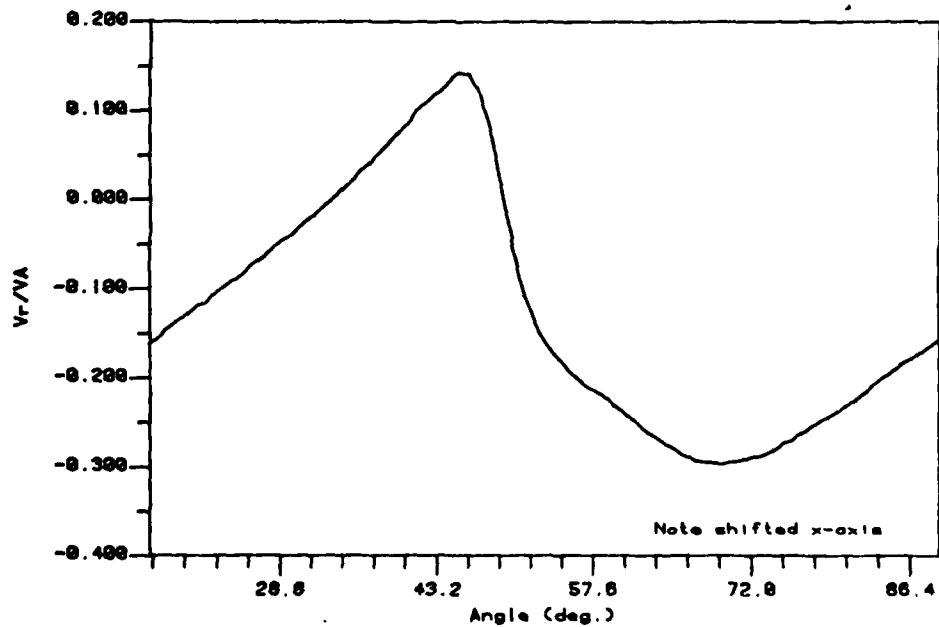


Figure 3-24b Field Point Velocity (Radial component)
Prop. 4383 at $x=-0.488R$, $r=0.875R$ at Design J

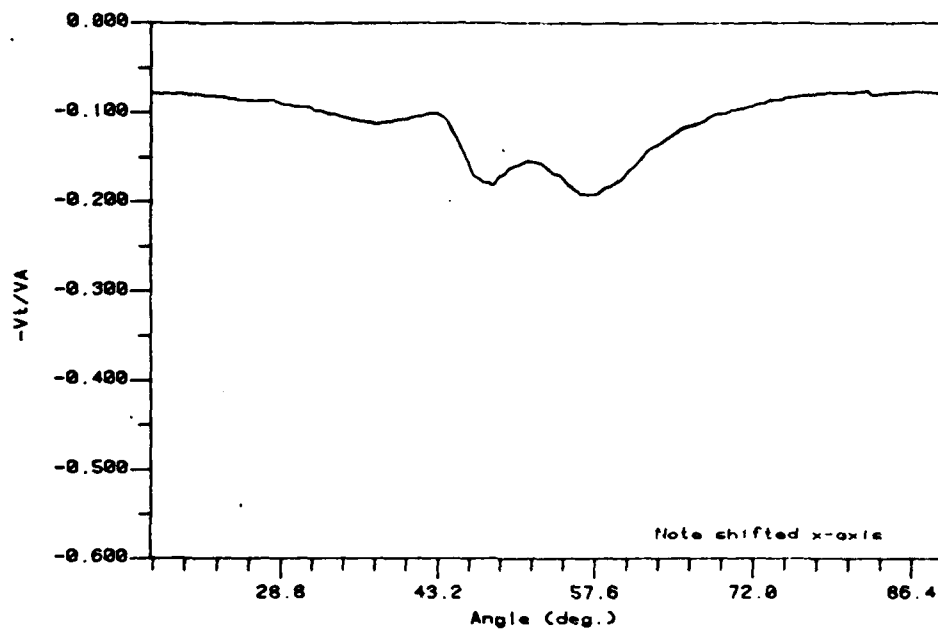


Figure 3-24c Field Point Velocity (Tangential component)
Prop. 4383 at $x=-0.488R$, $r=0.875R$ at Design J

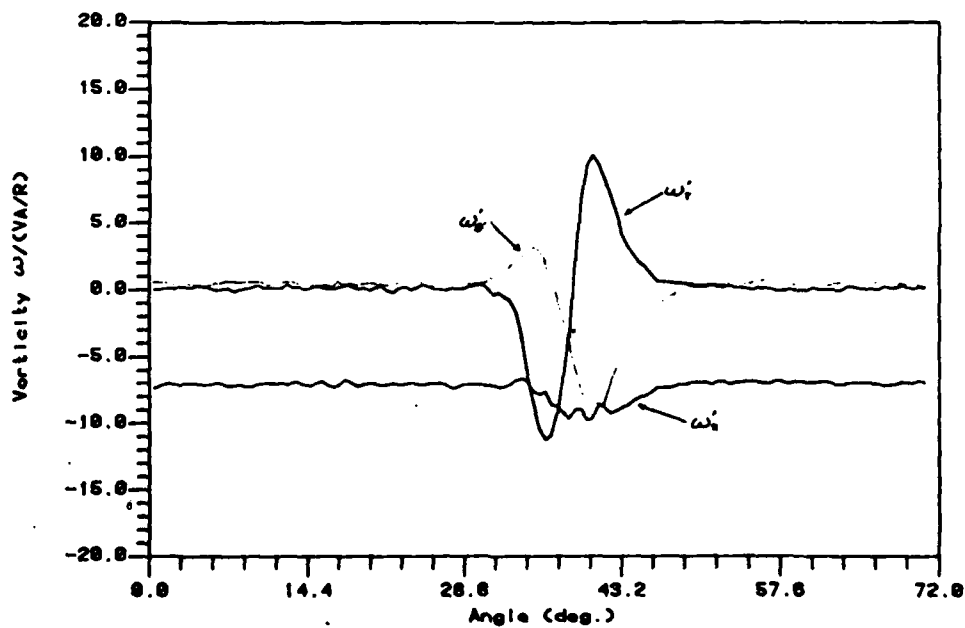


Figure 3-25 Vorticity Distribution
Prop. 4381 at $x=-0.333R$, $r=0.700R$ at Design J

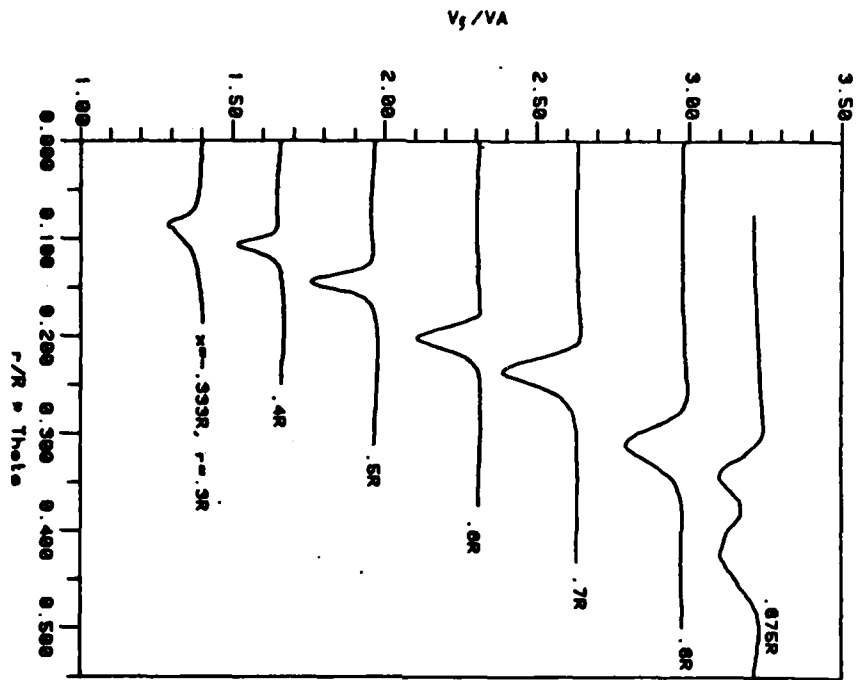


Figure 3-26 Velocity Component Parallel to Viscous Wake Prop. 4381 at Design J

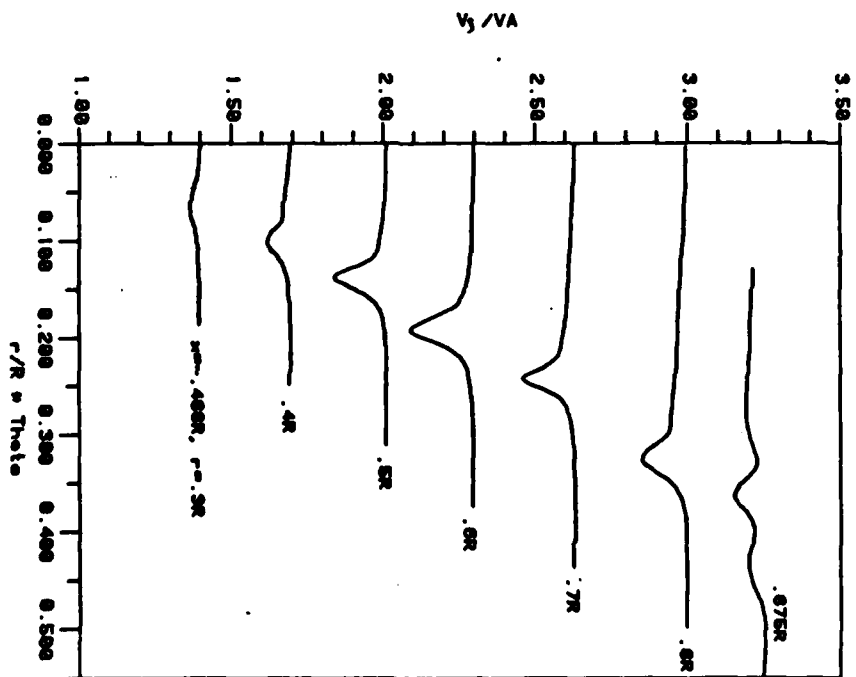


Figure 3-27 Velocity Component Parallel to Viscous Wake Prop. 4383 at Design J

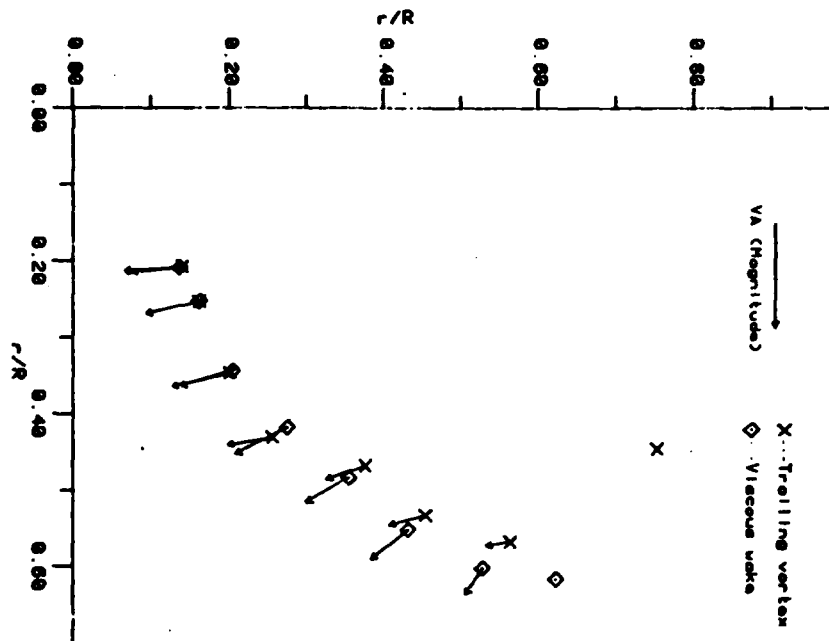


Figure 3-28 Geometry of the Two Vortices
Prop. 4381 at $x = -0.333R$ $J = 0.889$

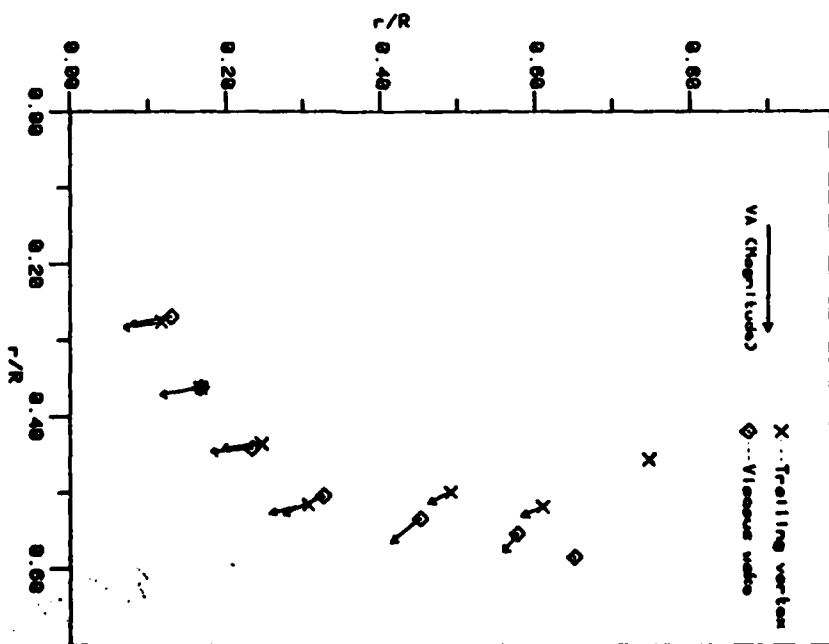


Figure 3-29 Geometry of the Two Vortices
Prop. 4383 at $x = -0.488R$ $J = 0.889$

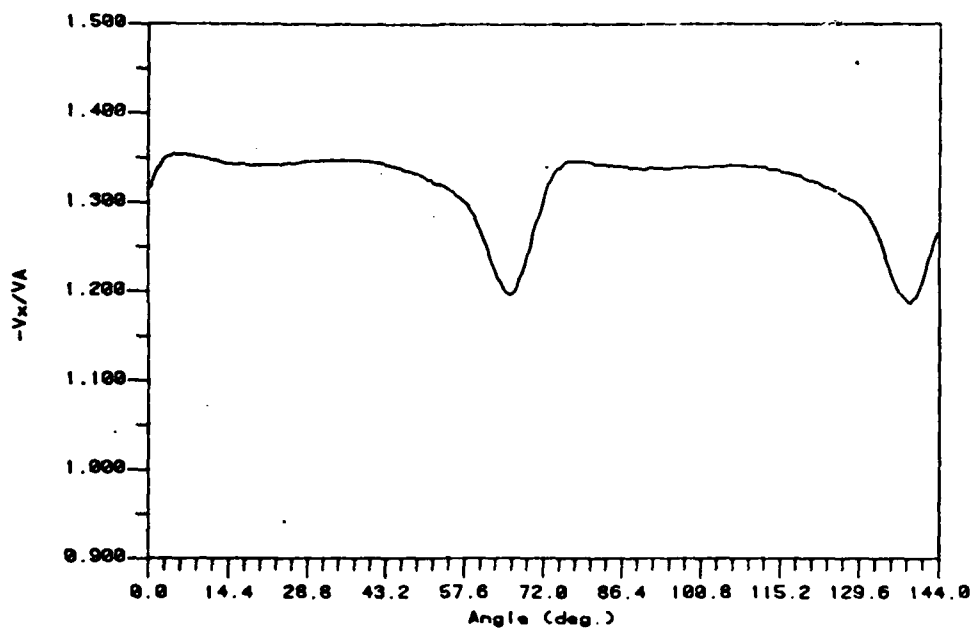


Figure 3-30a Field Point Velocity (Axial component)
Prop. 4381 at $x=-1.000R$, $r=0.700R$ at Design J

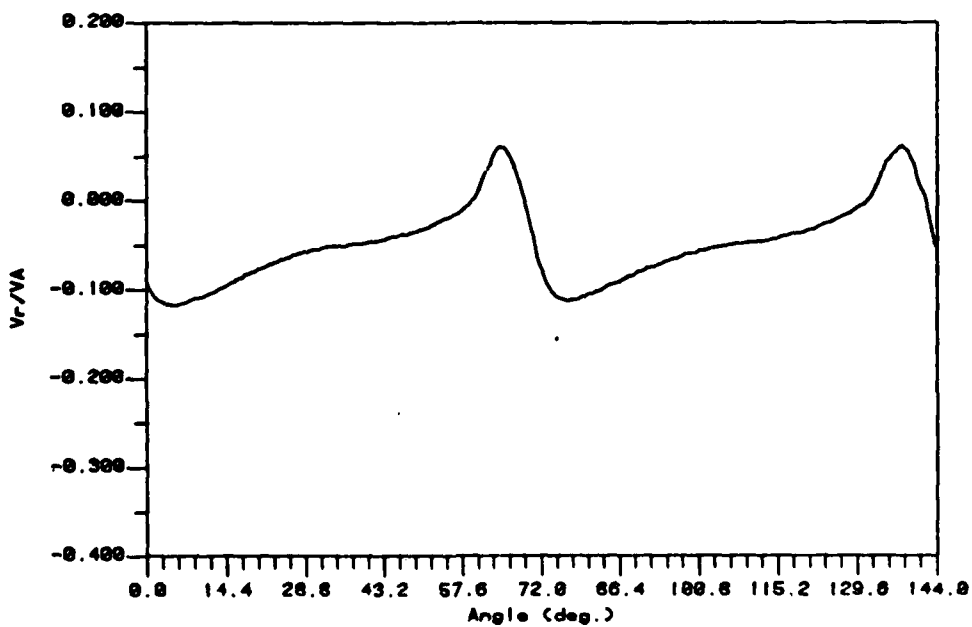


Figure 3-30b Field Point Velocity (Radial component)
Prop. 4381 at $x=-1.000R$, $r=0.700R$ at Design J

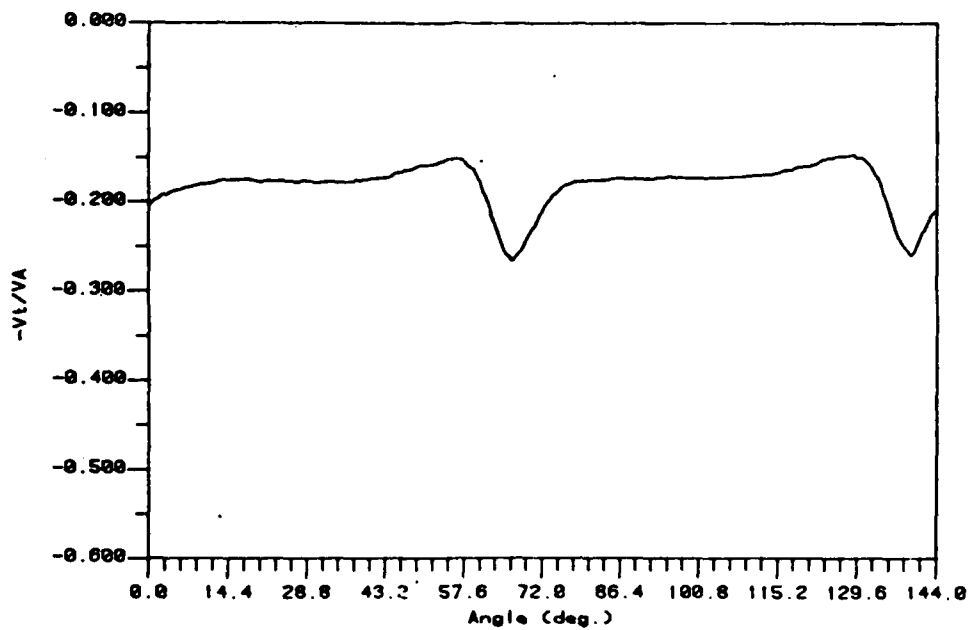


Figure 3-30c Field Point Velocity (Tangential component)
Prop. 4381 at $x=-1.000R$, $r=0.700R$ at Design J

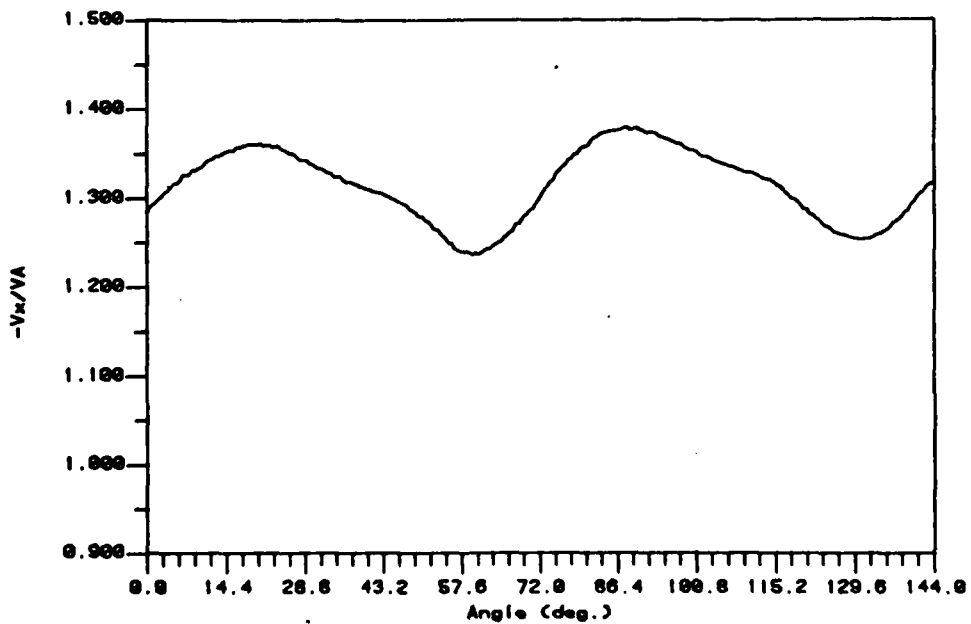


Figure 3-31a Field Point Velocity (Axial component)
Prop. 4381 at $x=-2.000R$, $r=0.700R$ at Design J

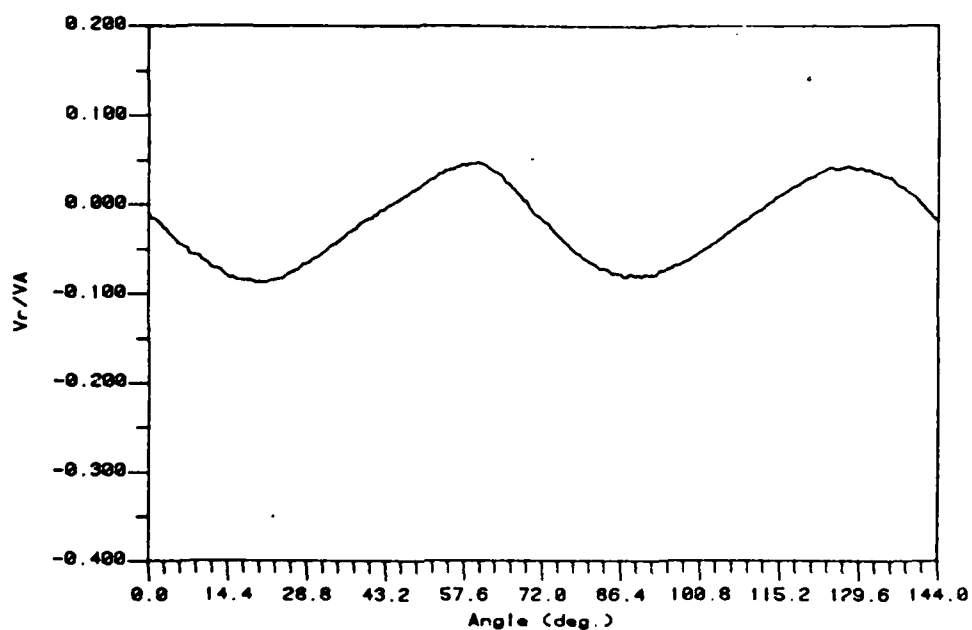


Figure 3-31b Field Point Velocity (Radial component)
Prop. 4381 at $x=-2.000R$, $r=0.700R$ at Design J

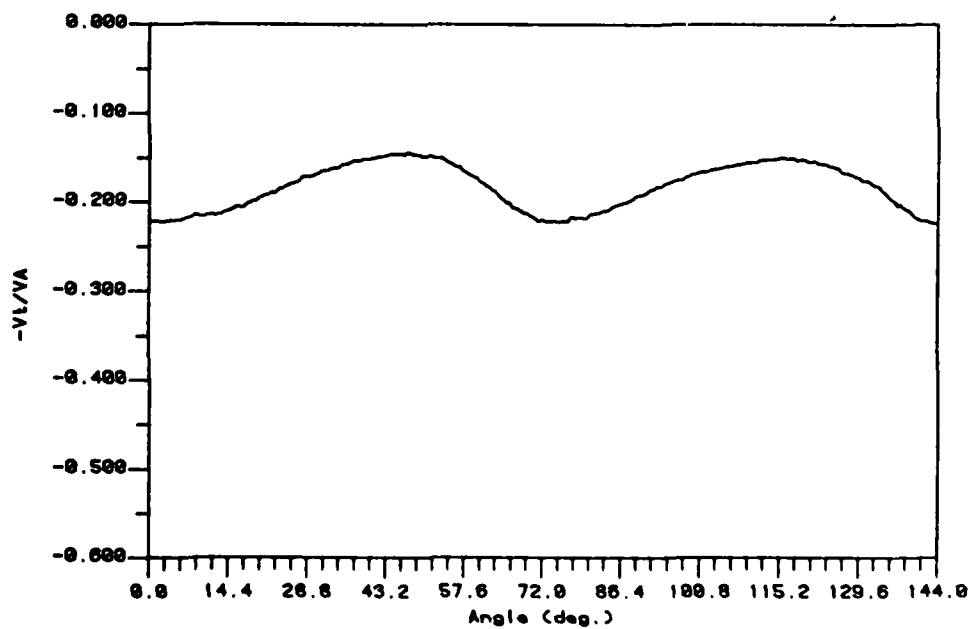


Figure 3-31c Field Point Velocity (Tangential component)
Prop. 4381 at $x=-2.000R$, $r=0.700R$ at Design J

PROPELLER FIELD POINT VELOCITY PROGRAM (FPV-10) RELEASE DATE 12/21/70 RUN DATE 3/28/81 11:38:41.00

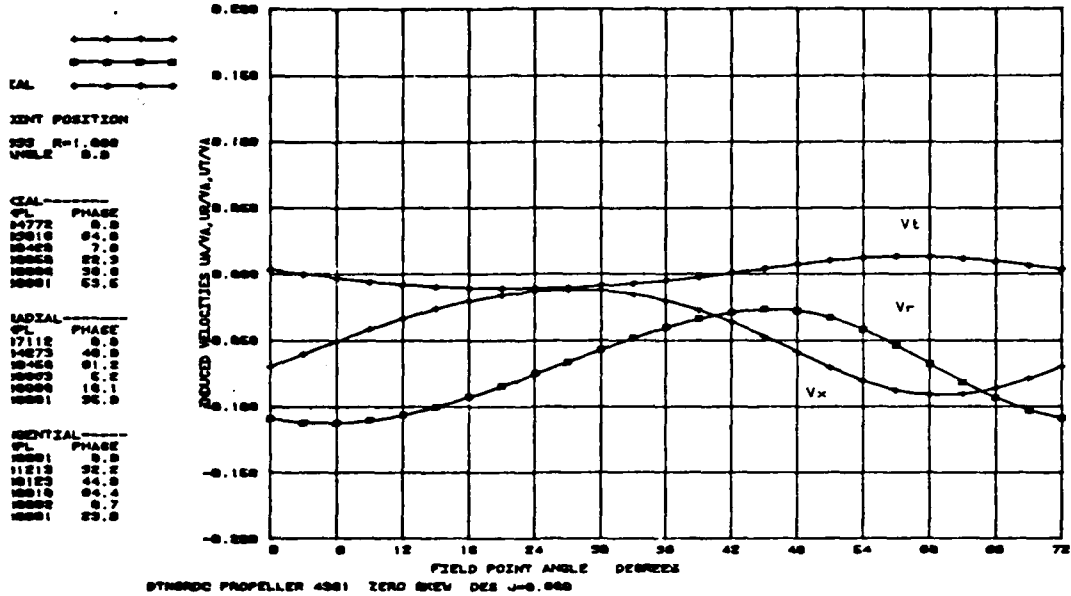


Figure 3-32 FPV-10 Output at $x=-0.333R$, $r=1.0R$ Prop. 4381

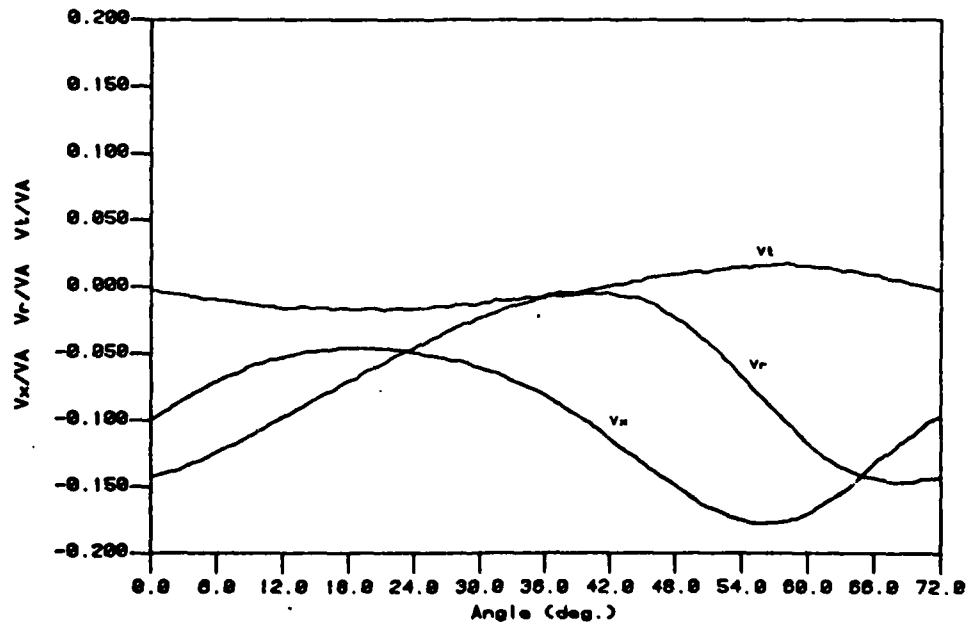


Figure 3-33 Field Point Velocity (Measured)
Prop. 4381 at $x=-0.333R$, $r=1.000R$ at Design J

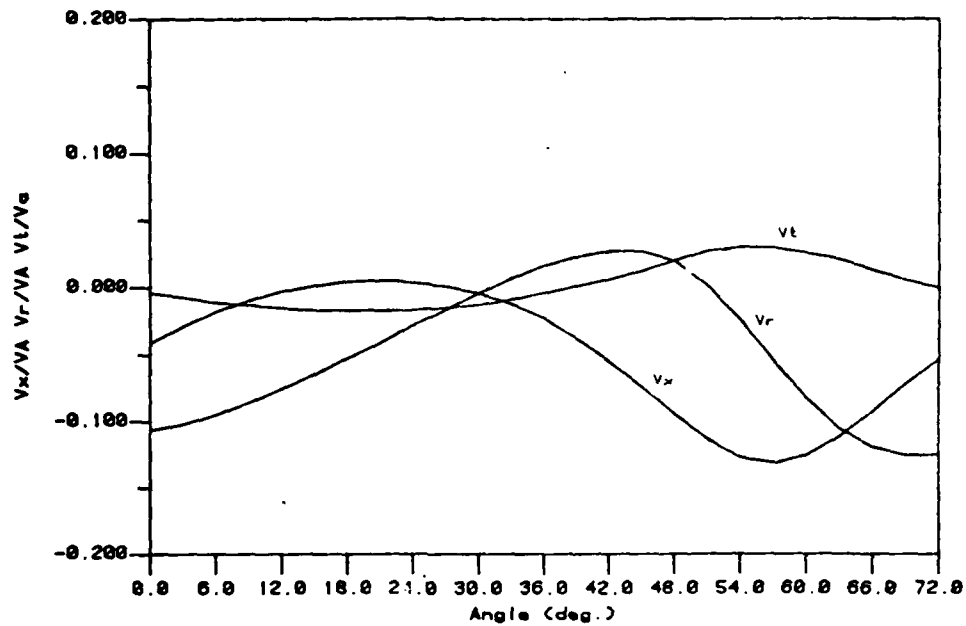
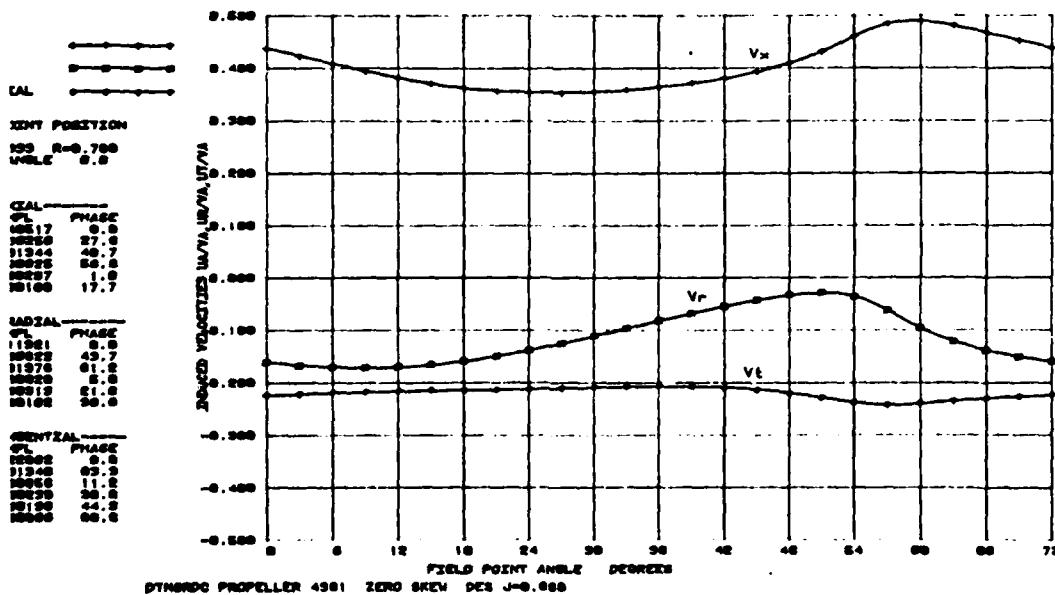


Figure 3-34 PSFFPV Output at $x=-0.333R$, $r=1.000R$
Prop. 4381 at Design J

PROPELLER FIELD POINT VELOCITY PROGRAM (FPV-10) RELEASE DATE 12/21/78 RUN DATE 3/25/81 10:48:09.00



DTN80C PROPELLER 4381 ZERO SKEW DES J-0.688

Figure 3-35 FPV-10 Output at $x=-0.333R$, $r=0.700R$ Prop. 4381

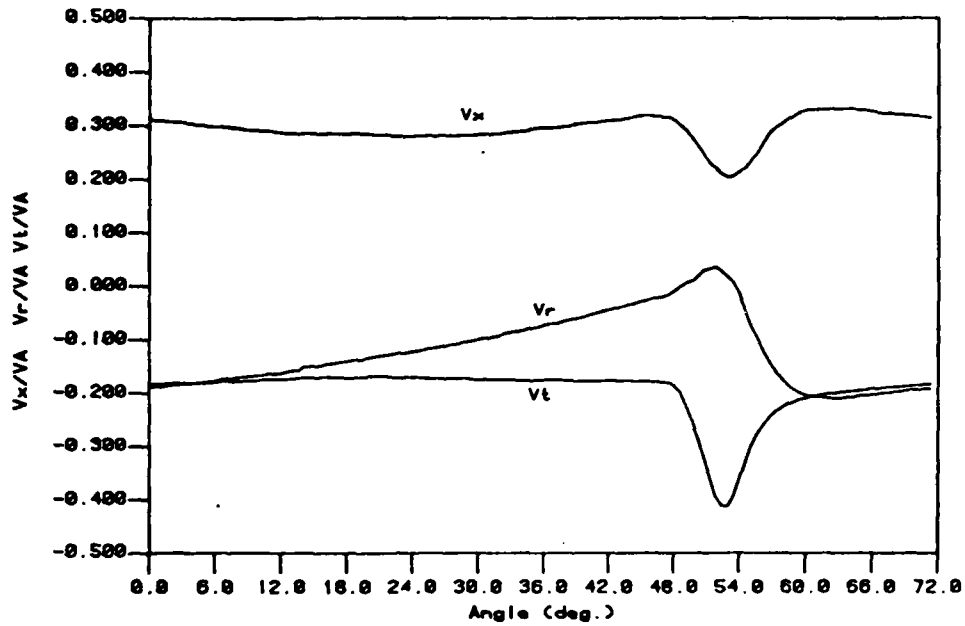


Figure 3-36 Field Point Velocity (Measured)
Prop. 4381 at $x=-0.333R$, $r=0.700R$ at Design J

PROPELLER FIELD POINT VELOCITY PROGRAM (FPV-10) RELEASE DATE 12/21/78 RUN DATE 3/05/81 08:22:04.00

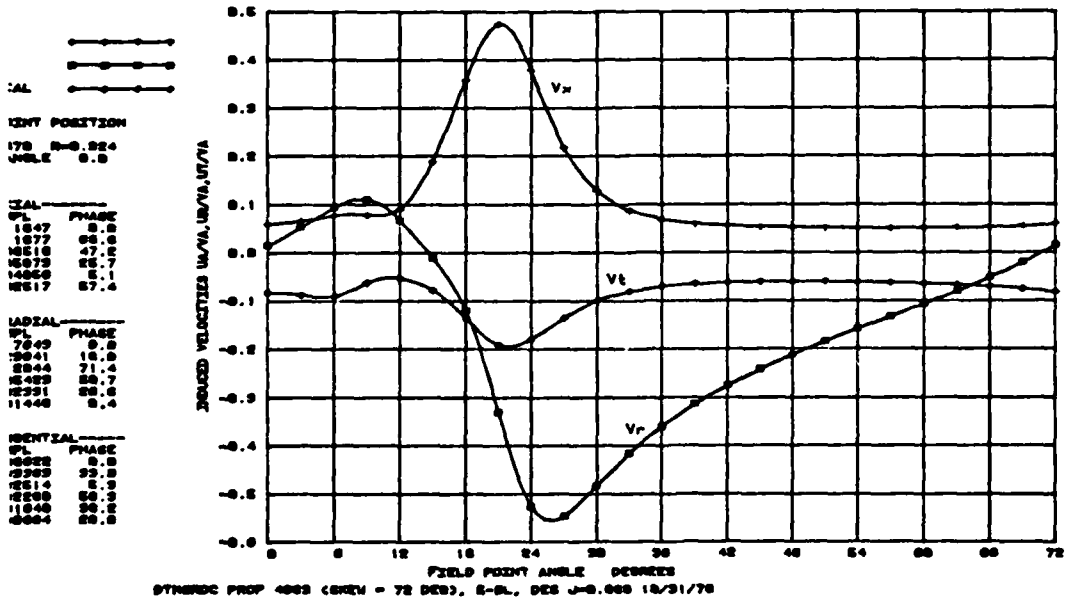


Figure 3-37 FPV-10 Output at $x=-0.470R$, $r=0.924R$ Prop. 4383

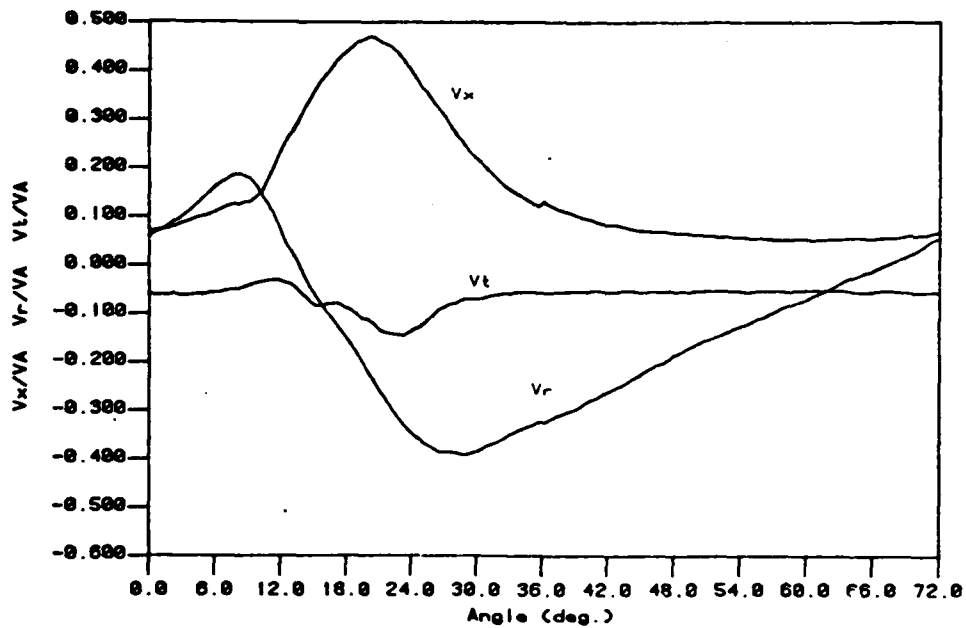


Figure 3-38 Field Point Velocity (Measured)
Prop. 4383 at $x=-0.470R$, $r=0.924R$ at Design J

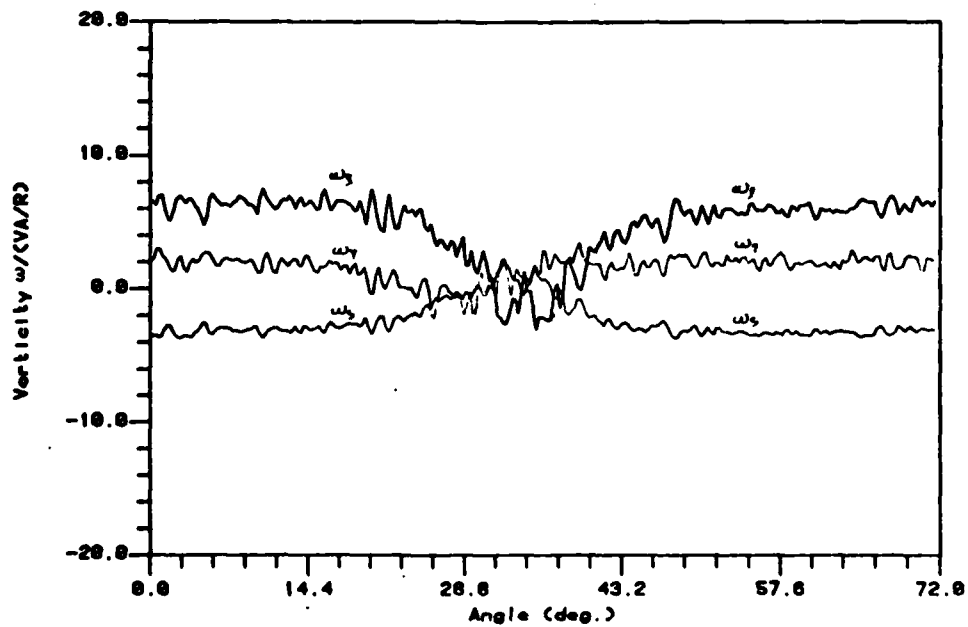


Figure 3-39 Transformed Vorticity
Prop. 4381 at $x=-0.333R$, $r=0.250R$ at Design J

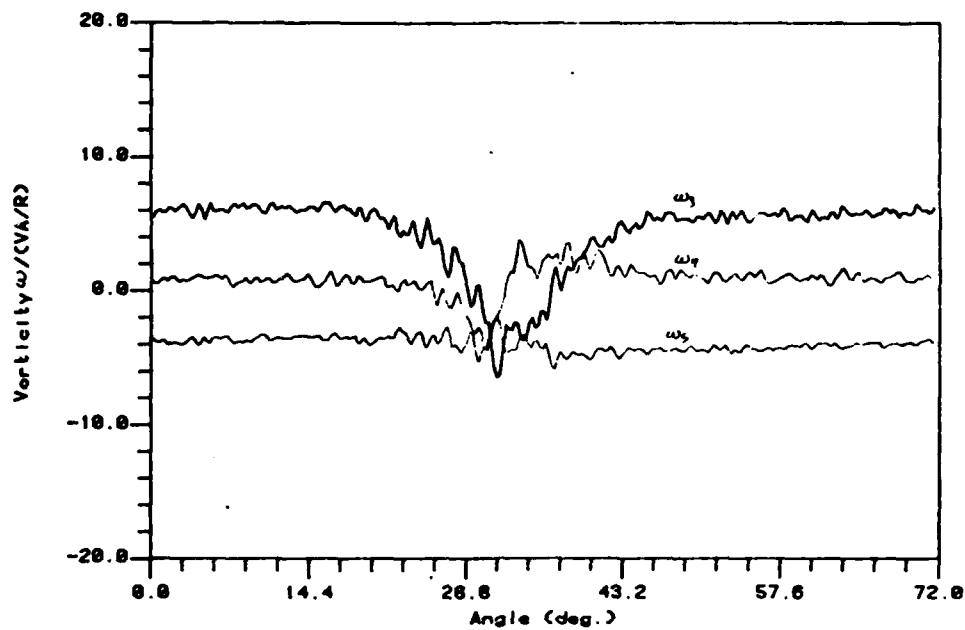


Figure 3-40 Transformed Vorticity
Prop. 4381 at $x=-0.333R$, $r=0.300R$ at Design J

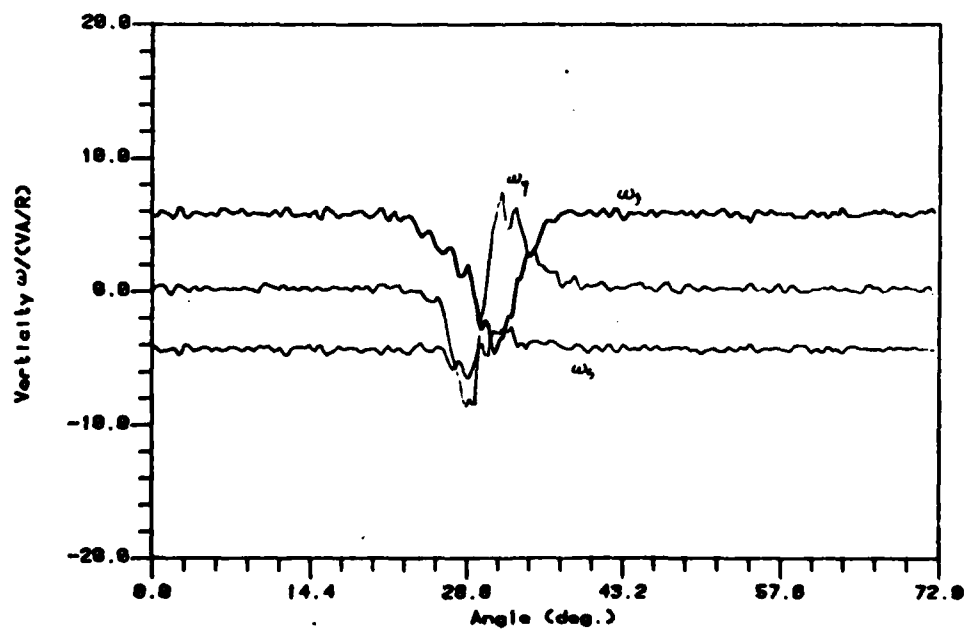


Figure 3-41 Transformed Vorticity
Prop. 4381 at $x=-0.333R$, $r=0.400R$ at Design J

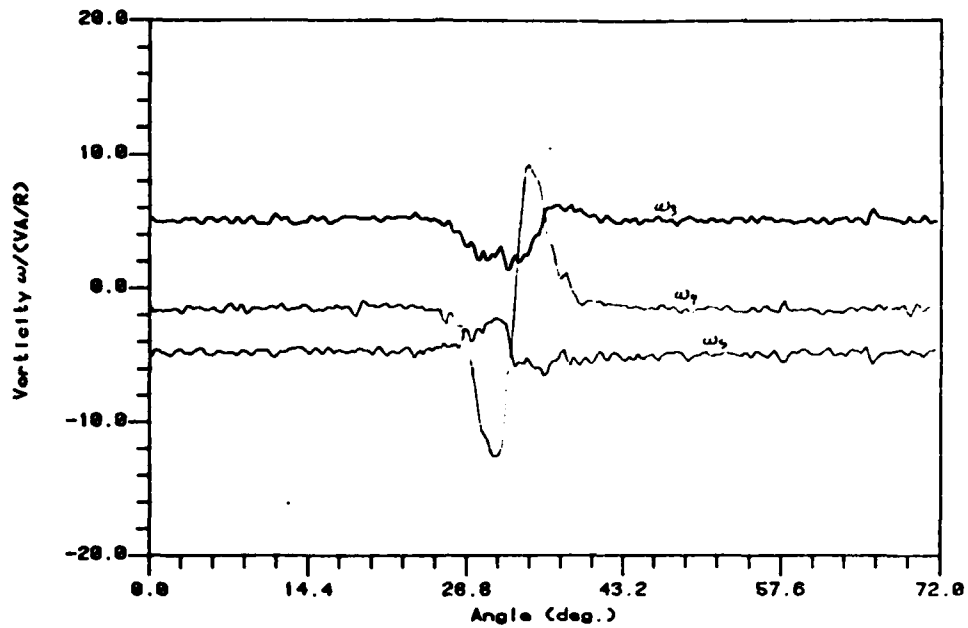


Figure 3-42 Transformed Vorticity
Prop. 4381 at $x=-0.333R$, $r=0.500R$ at Design J

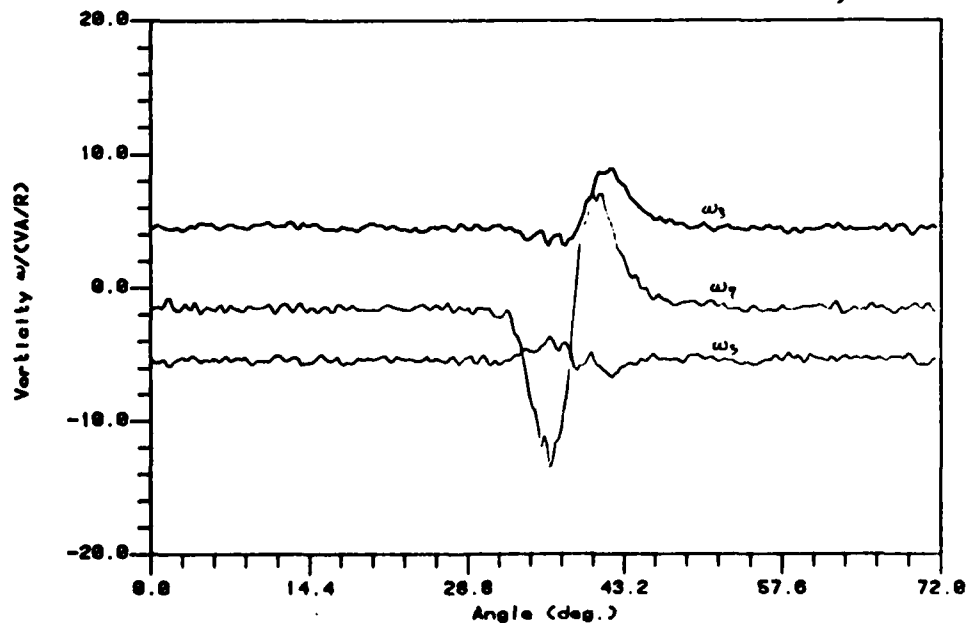


Figure 3-43 Transformed Vorticity
Prop. 4381 at $x=-0.333R$, $r=0.600R$ at Design J

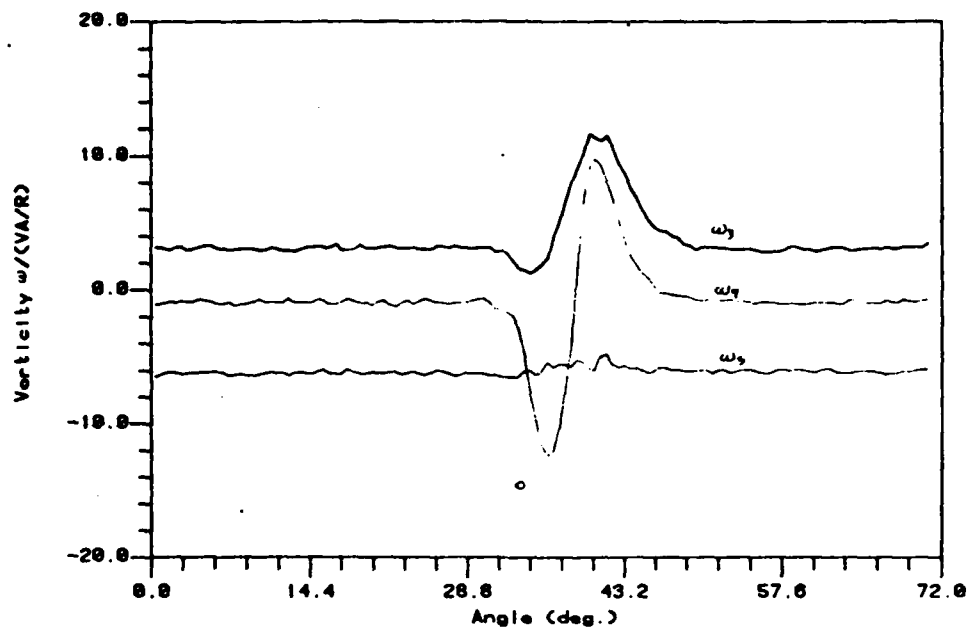


Figure 3-44 Transformed Vorticity
Prop. 4381 at $x=-0.333R$, $r=0.700R$ at Design J

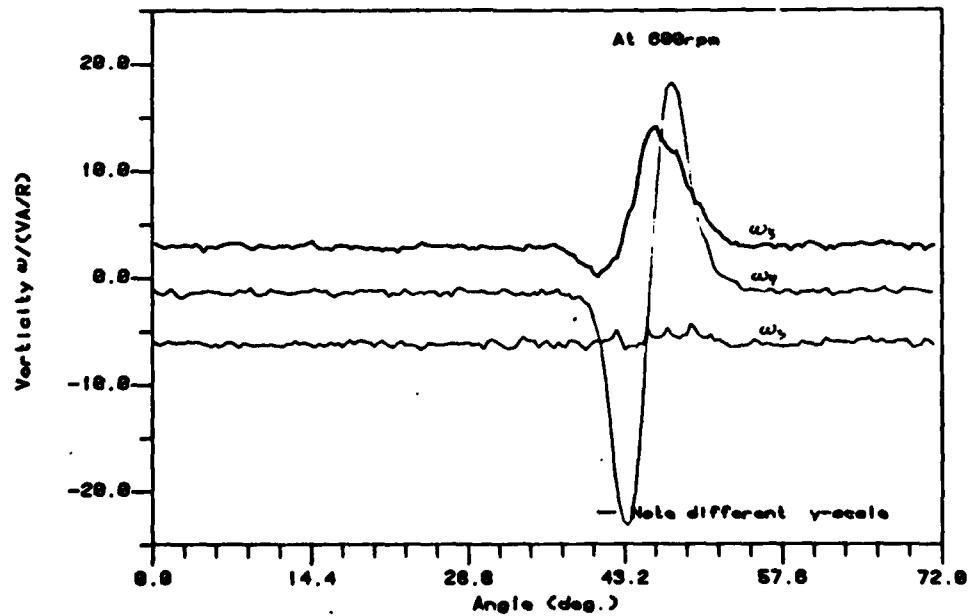


Figure 3-45 Transformed Vorticity
Prop. 4381 at $x=-0.333R$, $r=0.700R$ at Design J

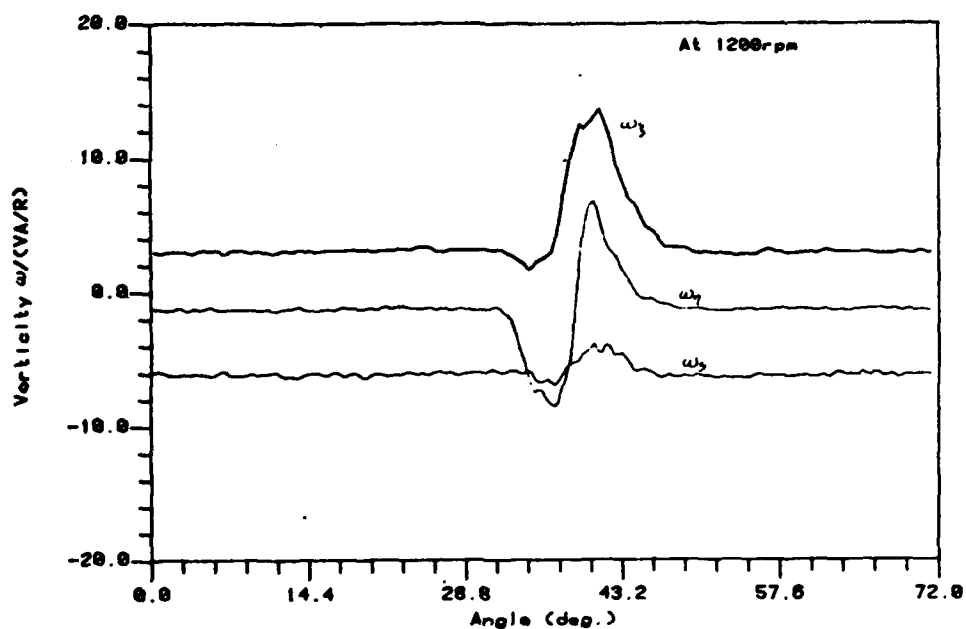


Figure 3-46 Transformed Vorticity
Prop. 4381 at $x=-0.333R$, $r=0.700R$ at Design J

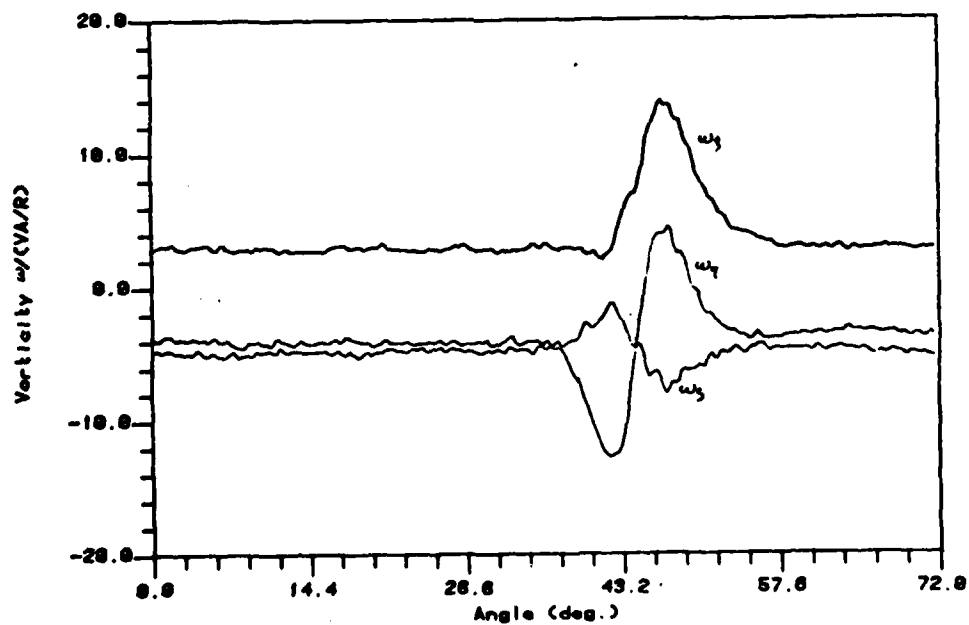


Figure 3-47 Transformed Vorticity
Prop. 4381 at $x=-0.333R$, $r=0.800R$ at Design J

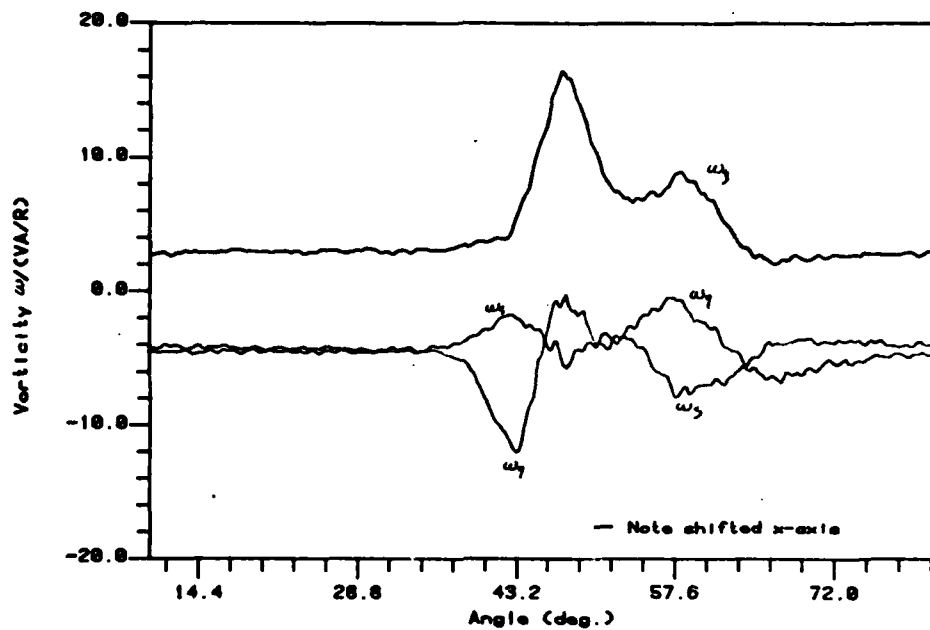


Figure 3-48 Transformed Vorticity
Prop. 4381 at $x=-0.333R$, $r=0.875R$ at Design J

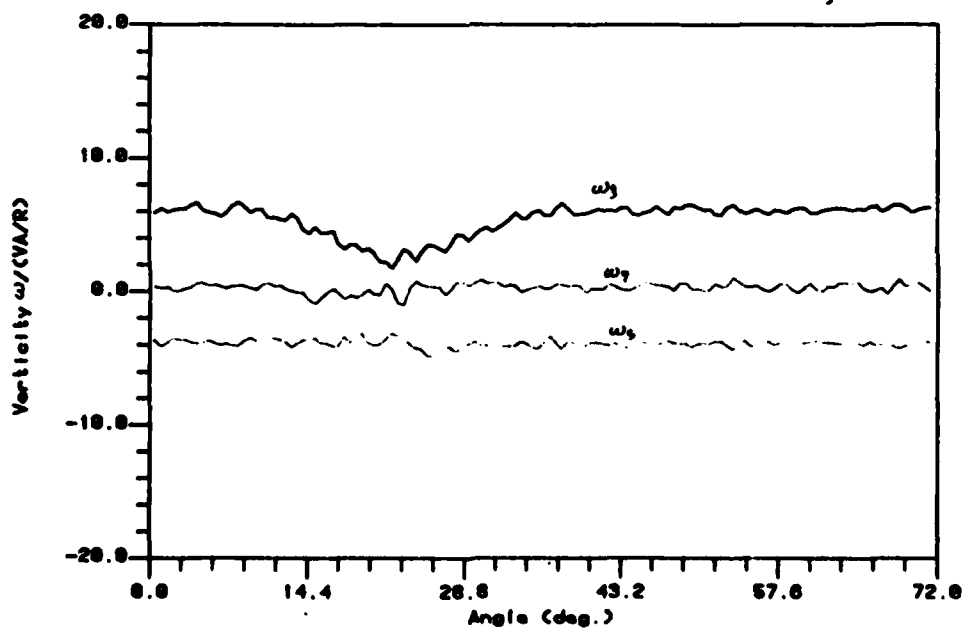


Figure 3-49 Transformed Vorticity
Prop. 4383 at $x=-0.488R$, $r=0.300R$ at Design J

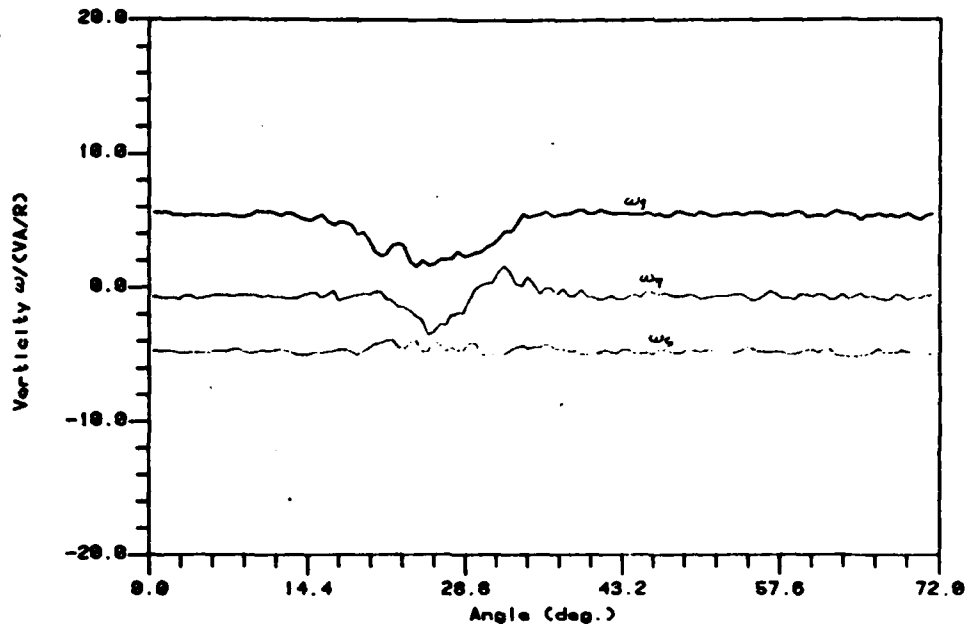


Figure 3-50 Transformed Vorticity
Prop. 4383 at $x=-0.488R$, $r=0.400R$ at Design J

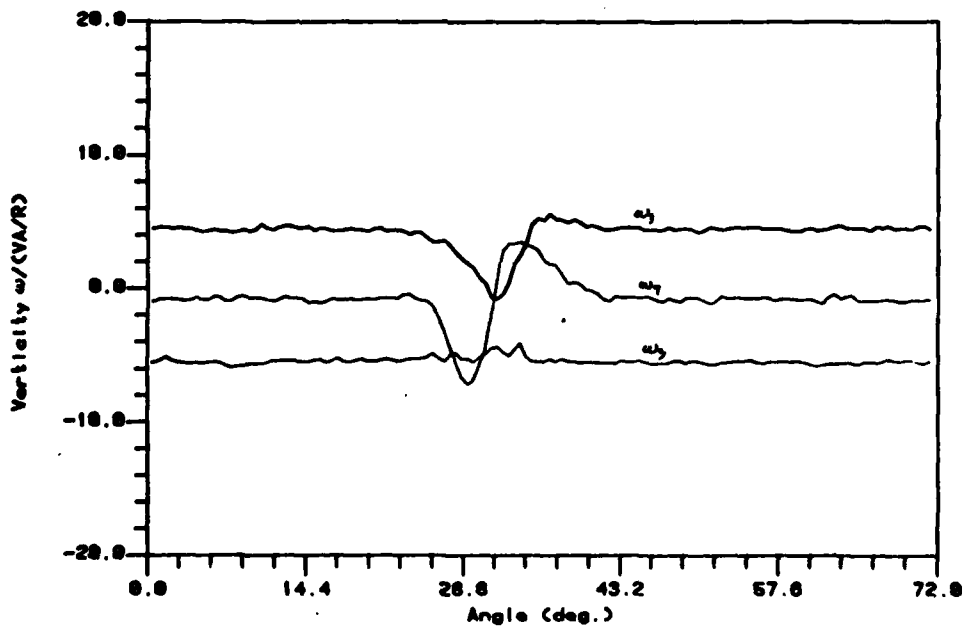


Figure 3-51 Transformed Vorticity
Prop. 4383 at $x=-0.488R$, $r=0.500R$ at Design J

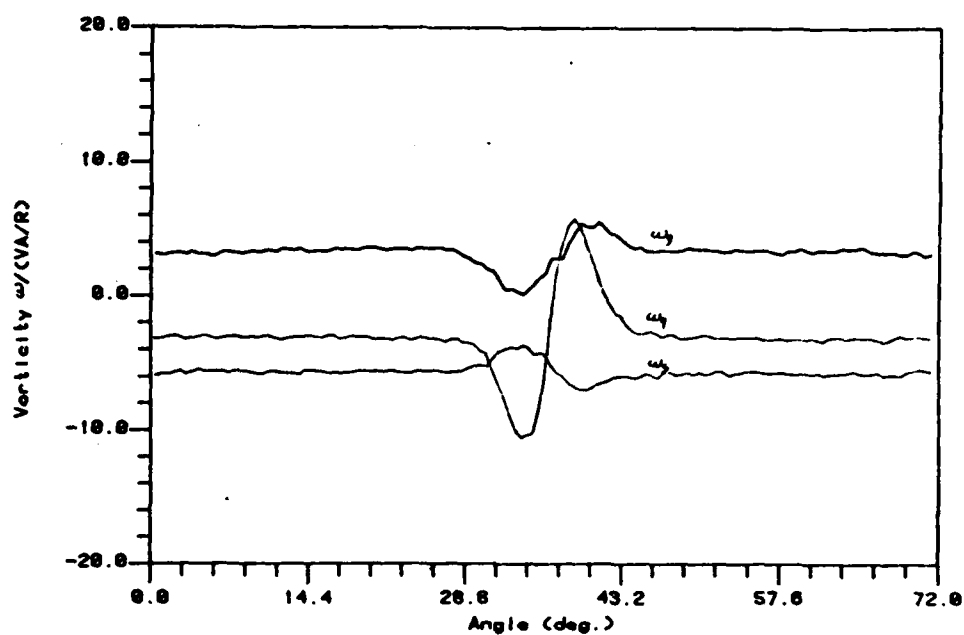


Figure 3-52 Transformed Vorticity
Prop. 4383 at $x=-0.488R$, $r=0.600R$ at Design J

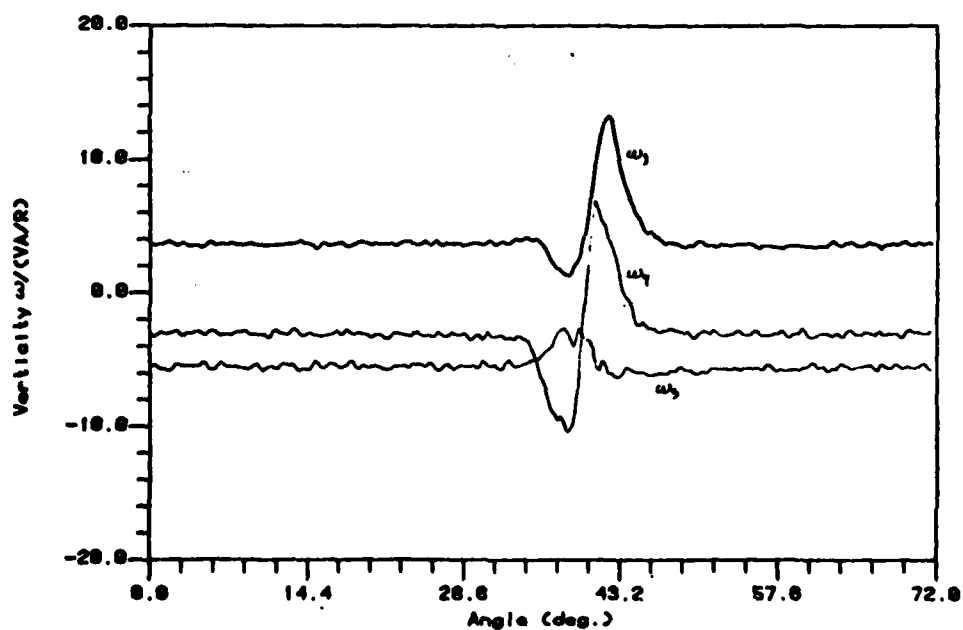


Figure 3-53 Transformed Vorticity
Prop. 4383 at $x=-0.488R$, $r=0.700R$ at Design J

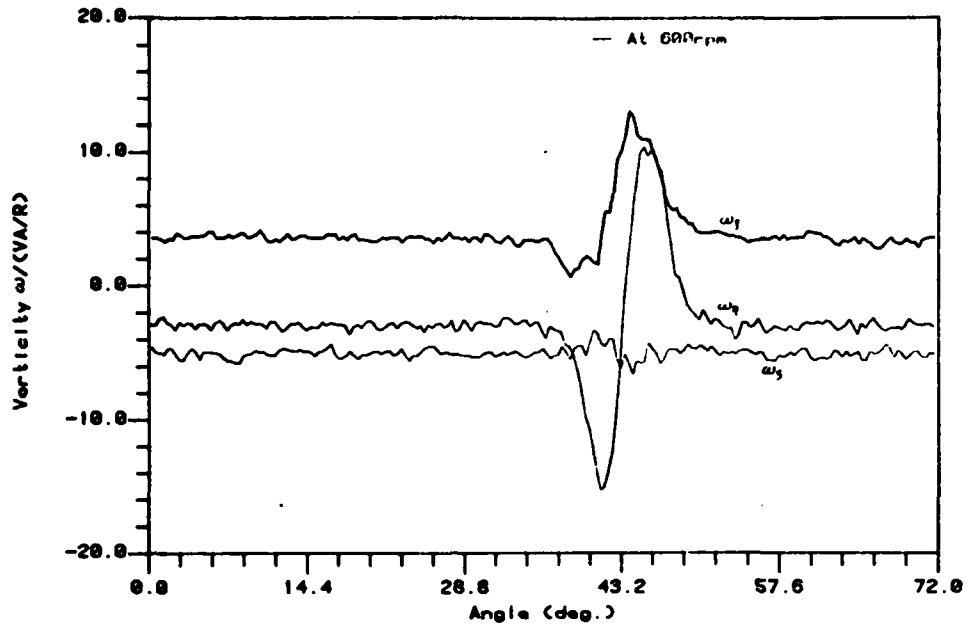


Figure 3-54 Transformed Vorticity
Prop. 4383 at $x=-0.488R$, $r=0.700R$ at Design J

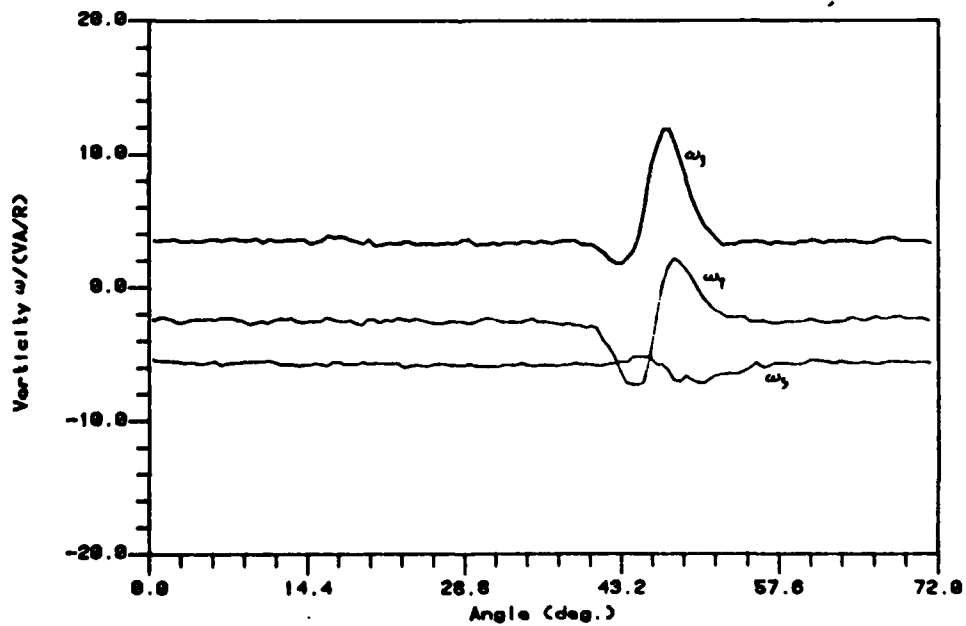


Figure 3-55 Transformed Vorticity
Prop. 4383 at $x=-0.488R$, $r=0.800R$ at Design J

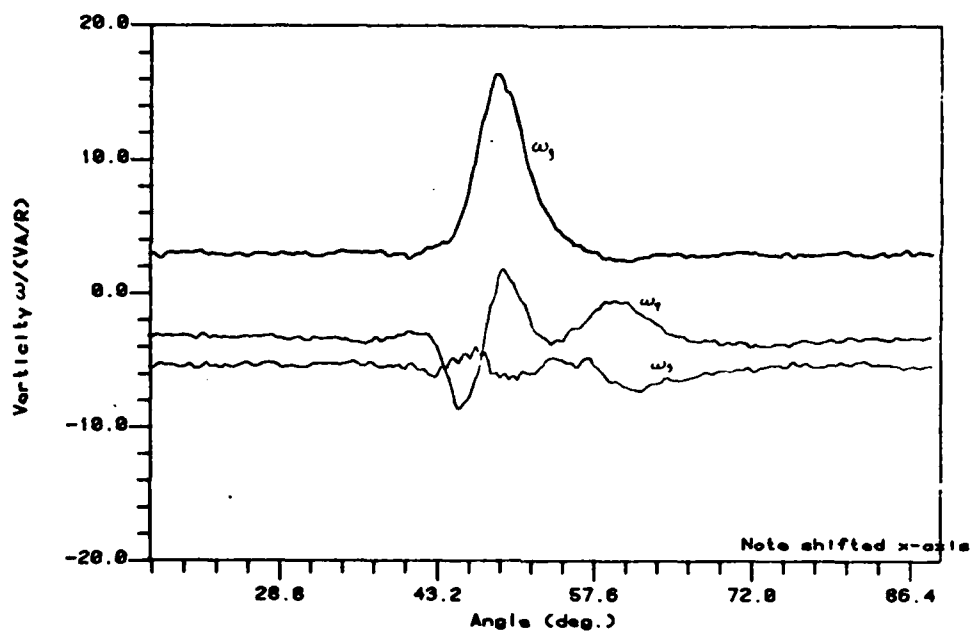


Figure 3-56 Transformed Vorticity
Prop. 4383 at $x=-0.488R$, $r=0.875R$ at Design J

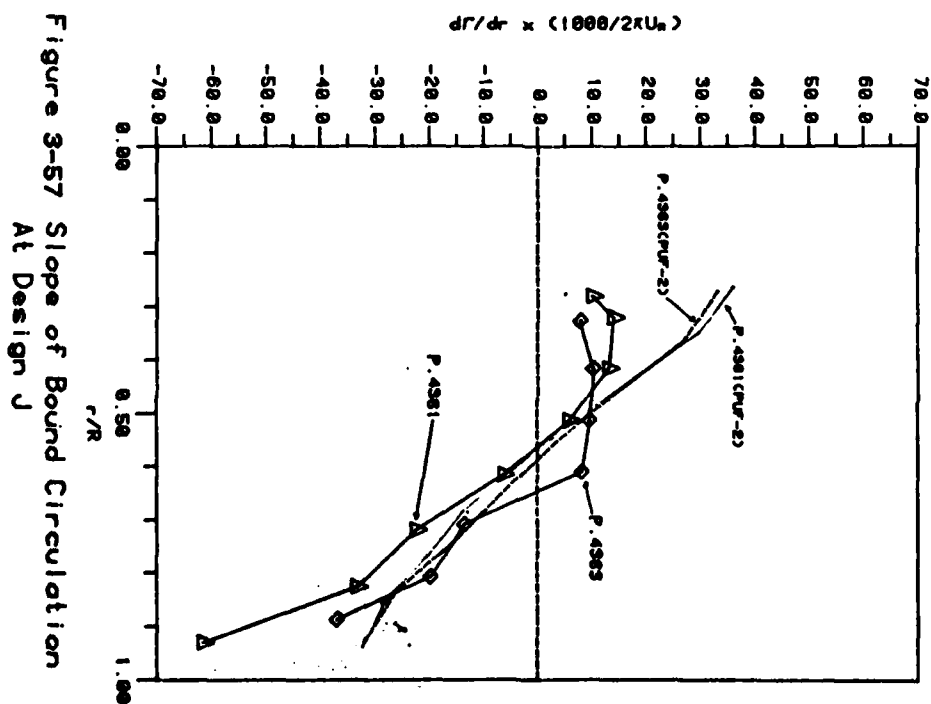


Figure 3-57 Slope of Bound Circulation
At Design J

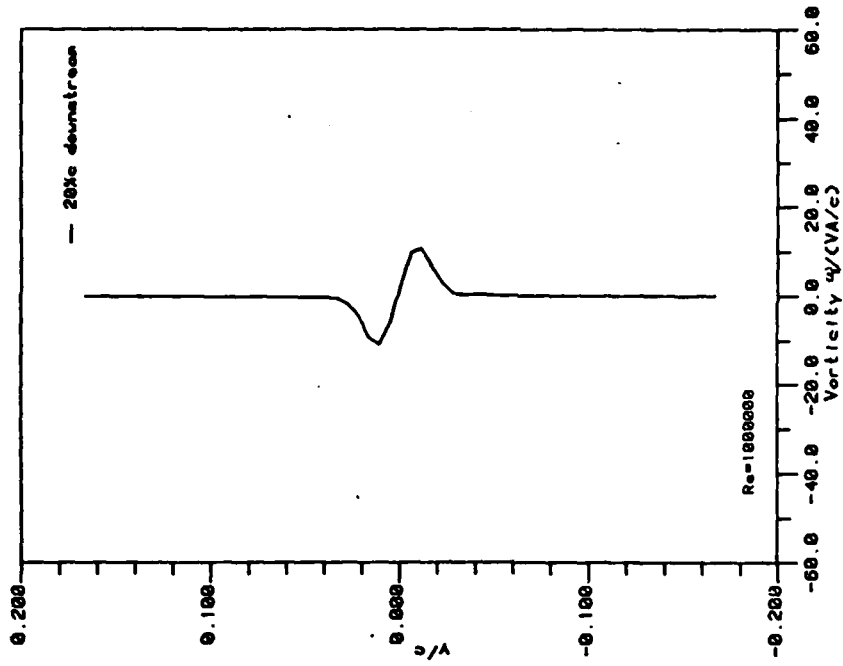


Figure 4-4b Vorticity Distribution
NACA 0012 at 0 angle of attack

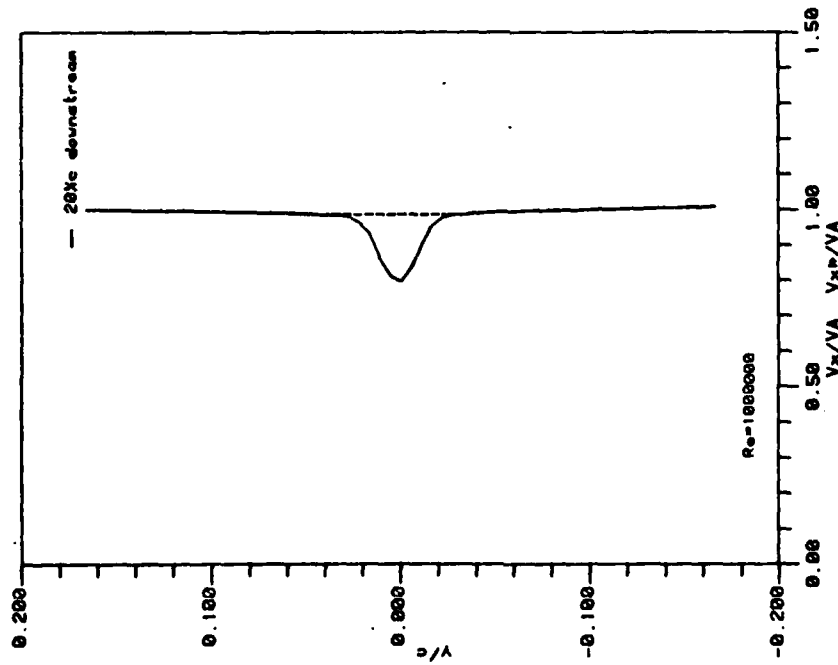


Figure 4-4a Velocity Distributions
NACA 0012 at 0 angle of attack

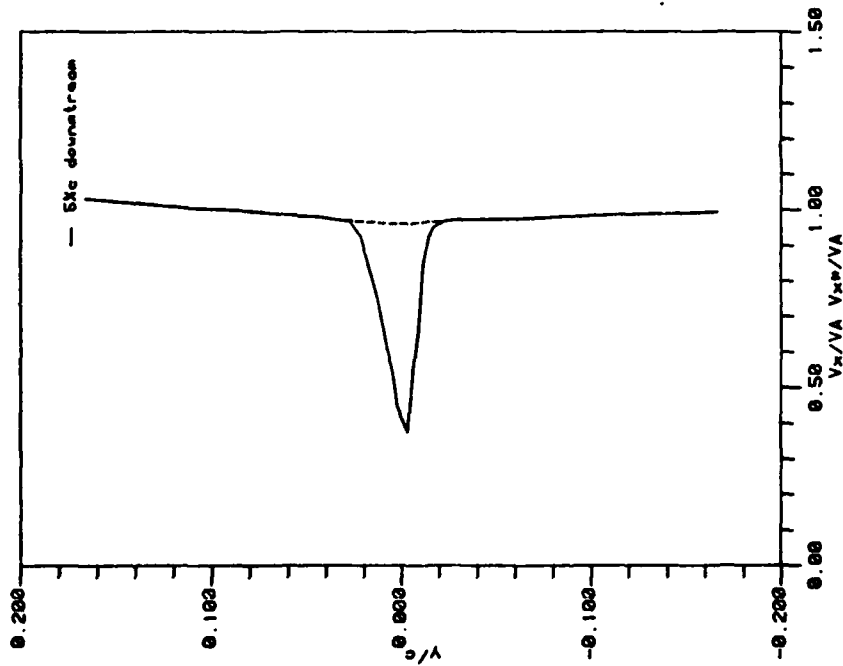


Figure 4-5a Velocity Distributions
NACA 66-309 @ 4.5deg. $Re=900000$

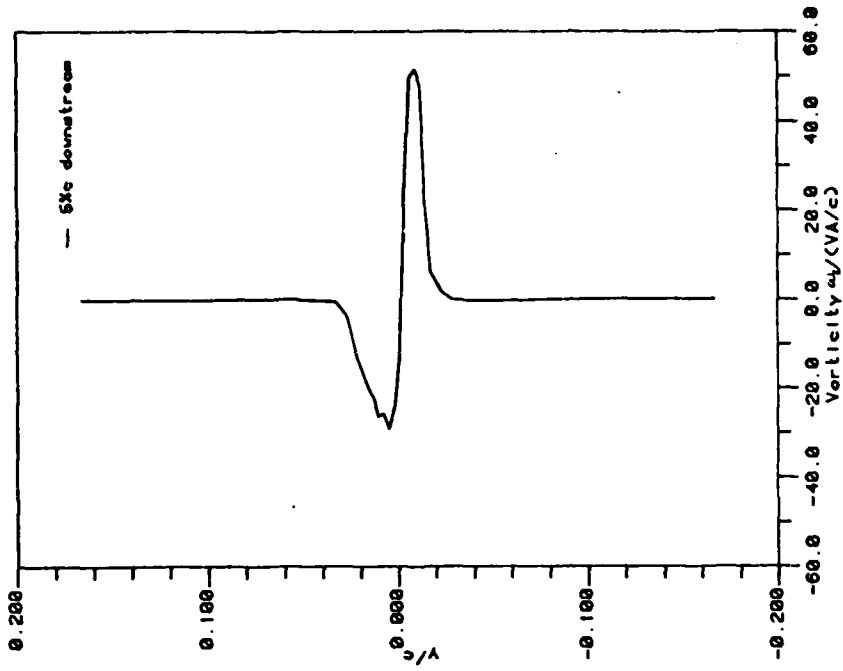


Figure 4-5b Vorticity Distribution
NACA 66-309 @ 4.5deg. $Re=900000$

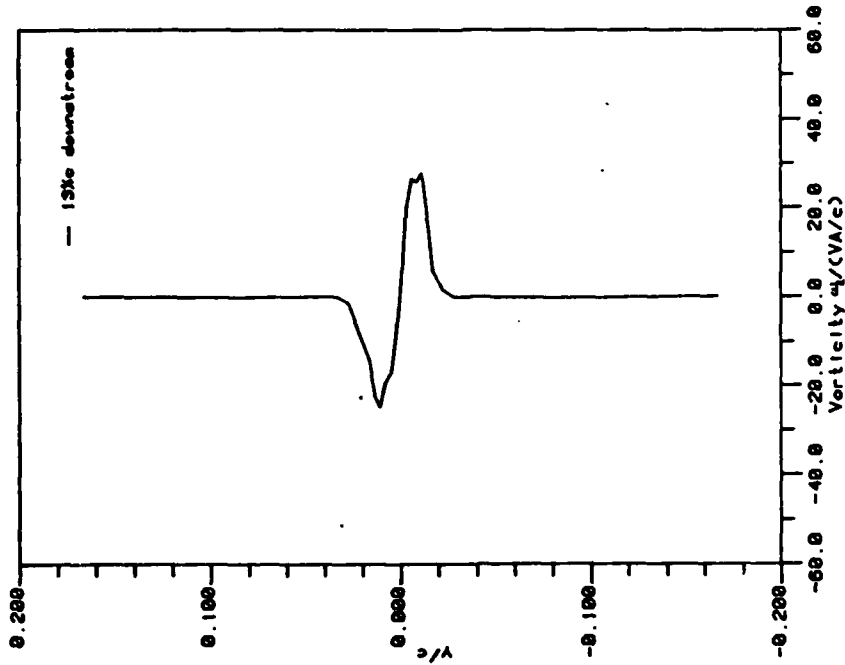


Figure 4-6a Velocity Distributions
NACA 66-309 @ 4.5deg. $Re=2000000$

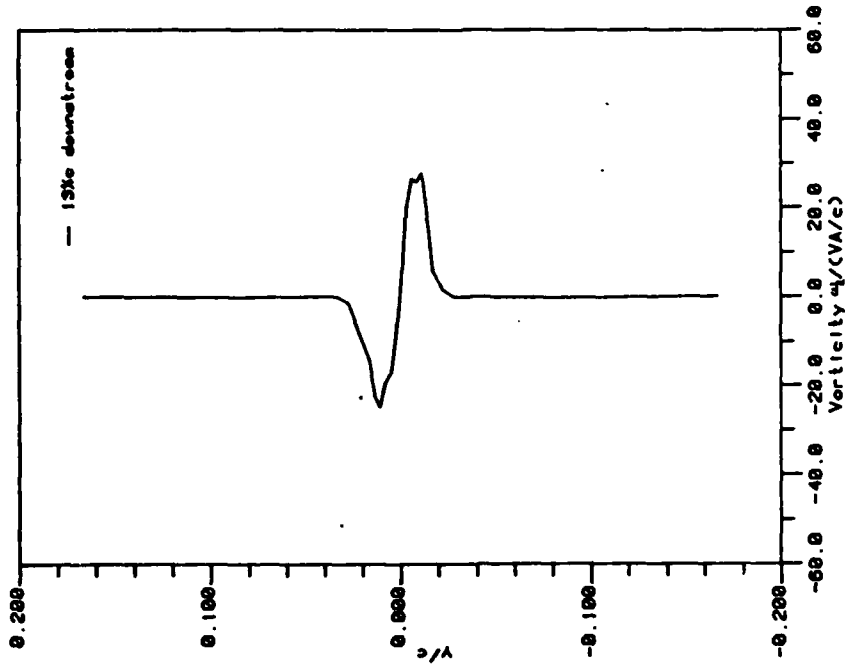


Figure 4-6b Vorticity Distribution
NACA 66-309 @ 4.5deg. $Re=2000000$

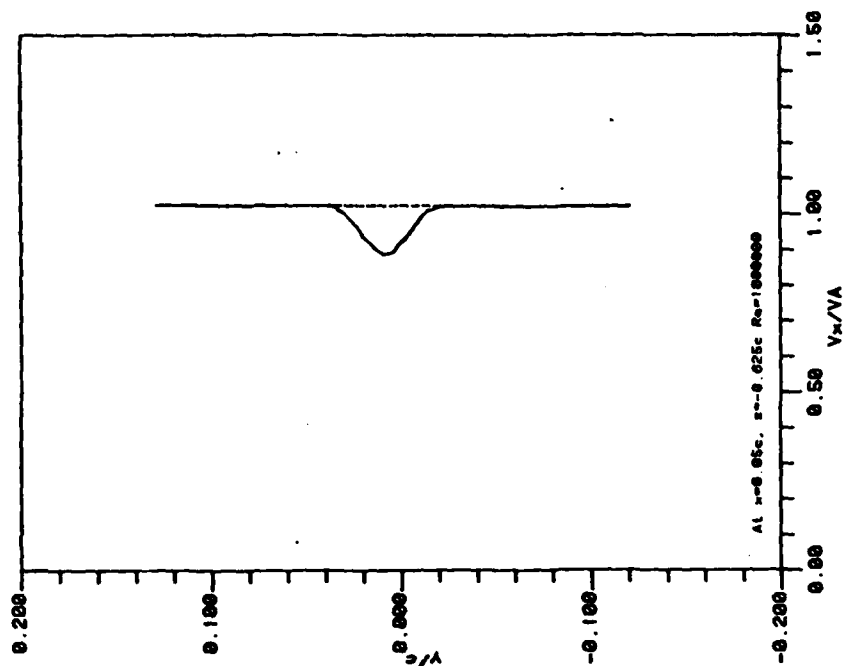


Figure 4-9 Velocity in the Wake
SNAME Keel Model No.3

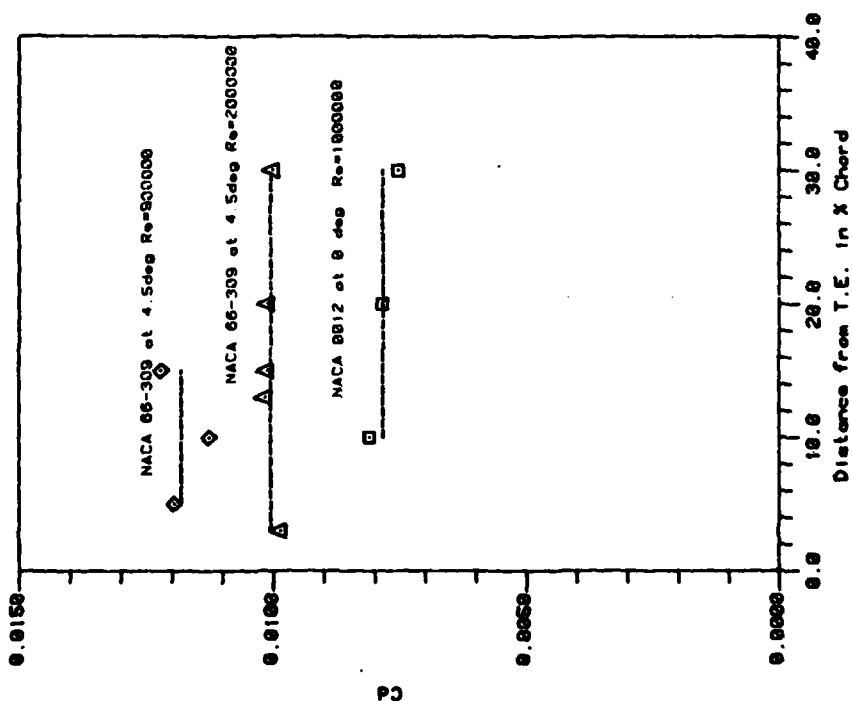


Figure 4-7 Coefficient of Profile Drag
Obtained at Several Measurement Points

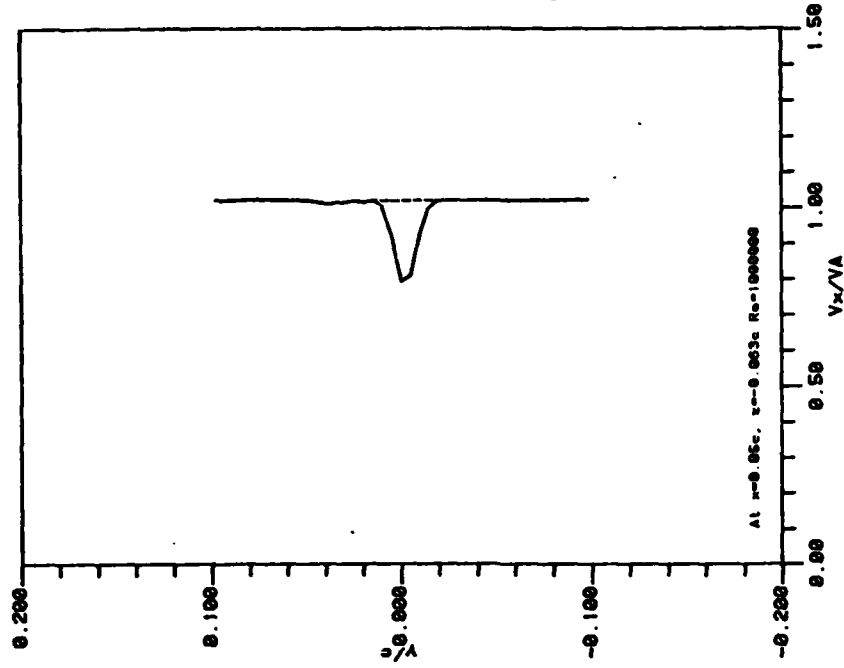


Figure 4-10 Velocity in the Wake
SNAME Keel Model No.3

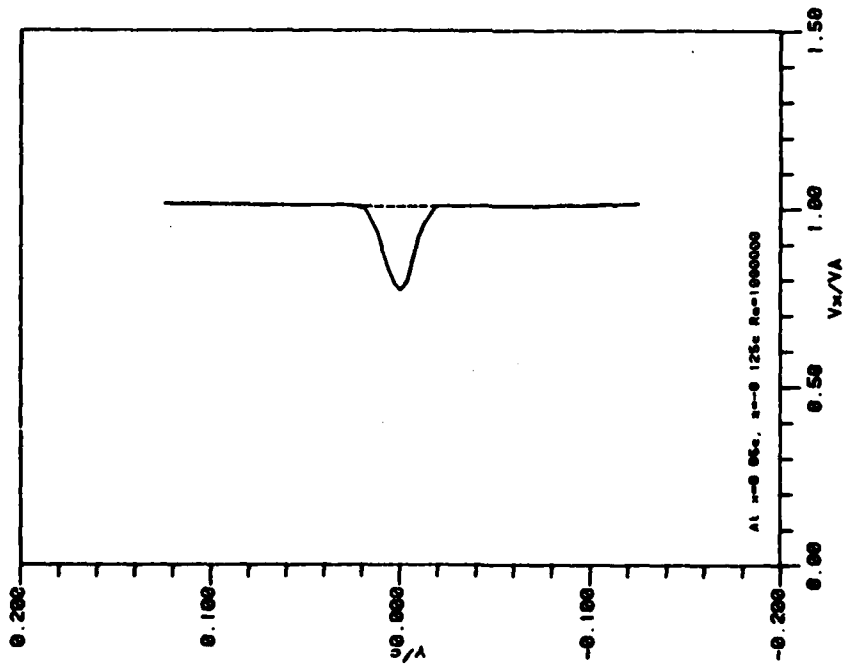


Figure 4-11 Velocity in the Wake
SNAME Keel Model No.3

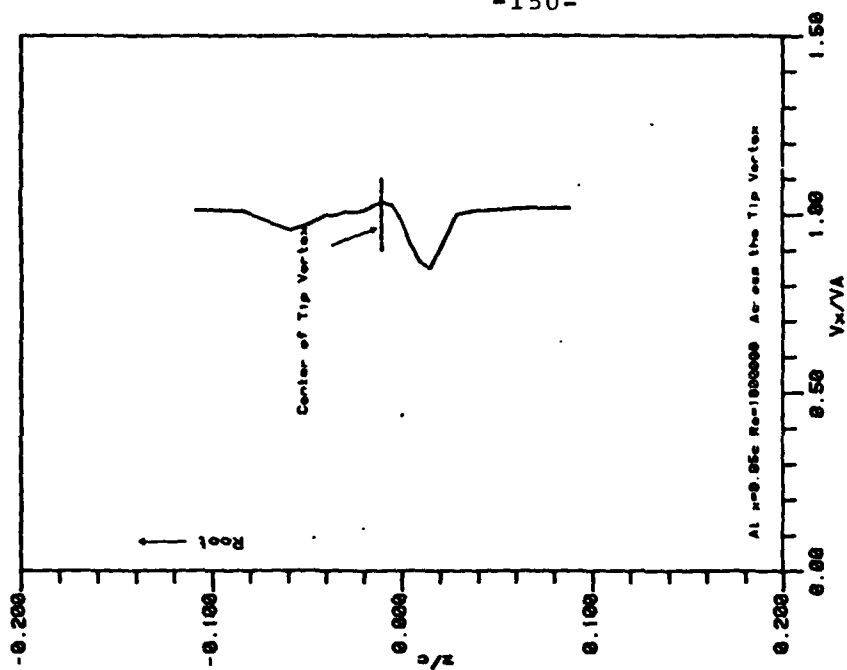


Figure 4-12 Velocity in the Wake
SNAME Keel Model No.3

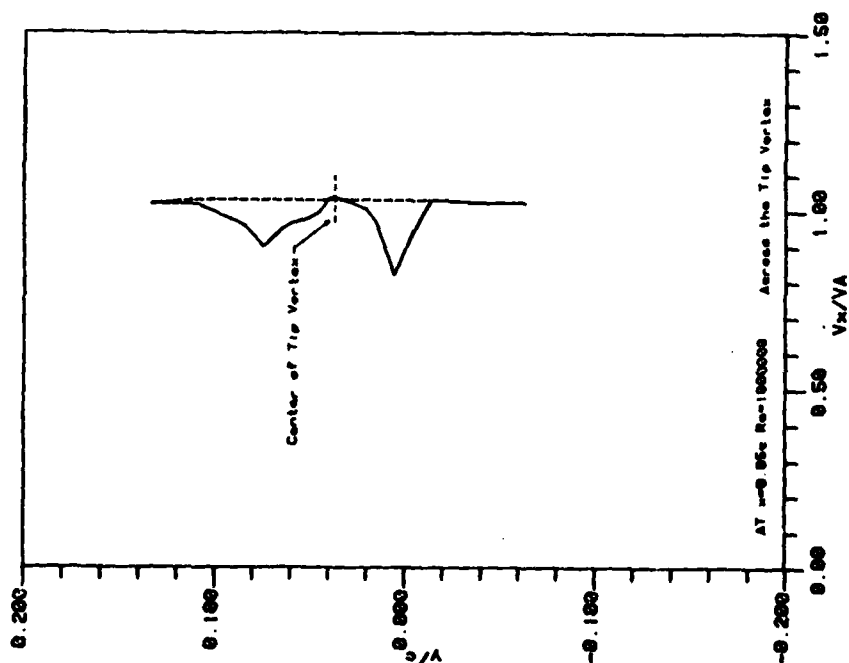


Figure 4-13 Velocity Distribution
SNAME Keel Model No.3

Figure 4-14 Spanwise Distribution of Profile Drag SNAME Keel Model No.3

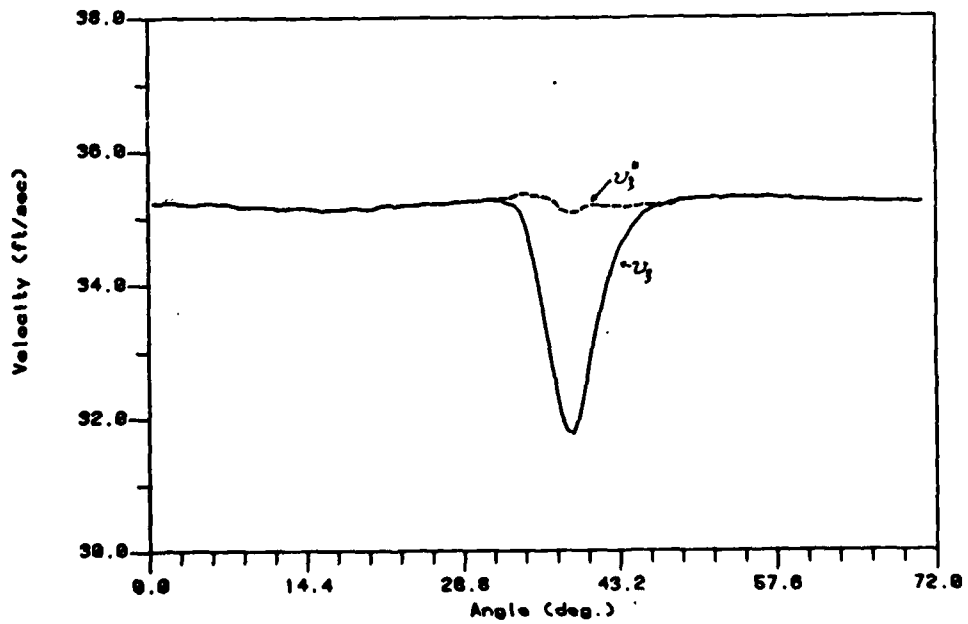
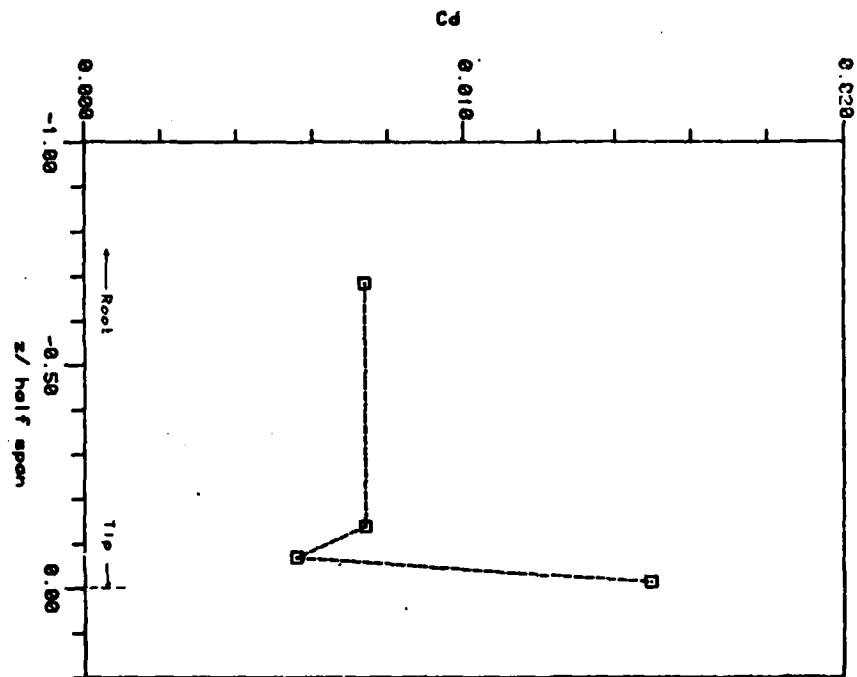


Figure 4-17 Hypothetical Velocity Constructed from Measured Velocity and Vorticity Prop. 4381

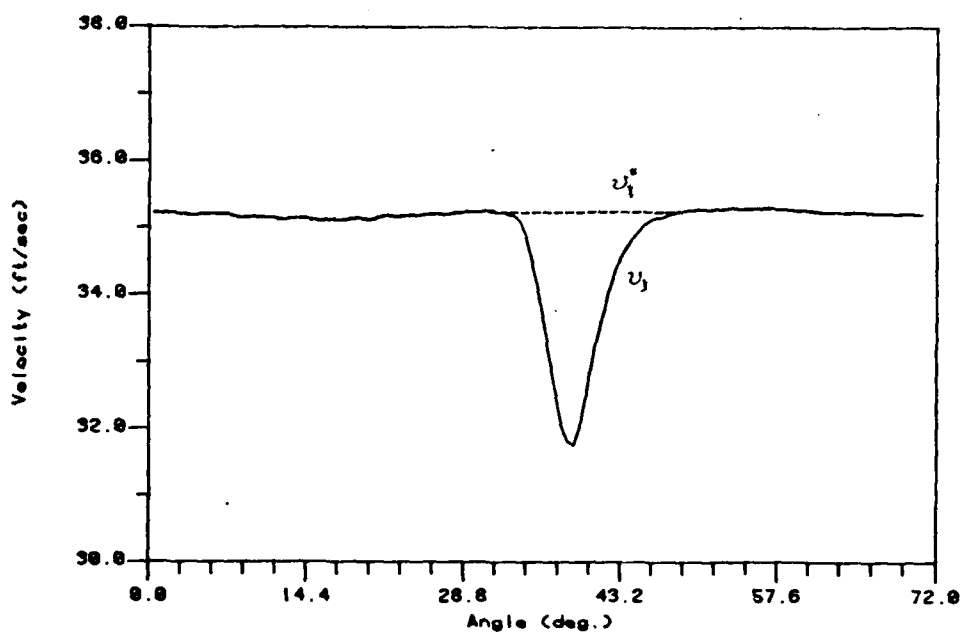


Figure 4-18 Hypothetical Velocity obtained from
Constant Pressure Assumption Prop. 4381

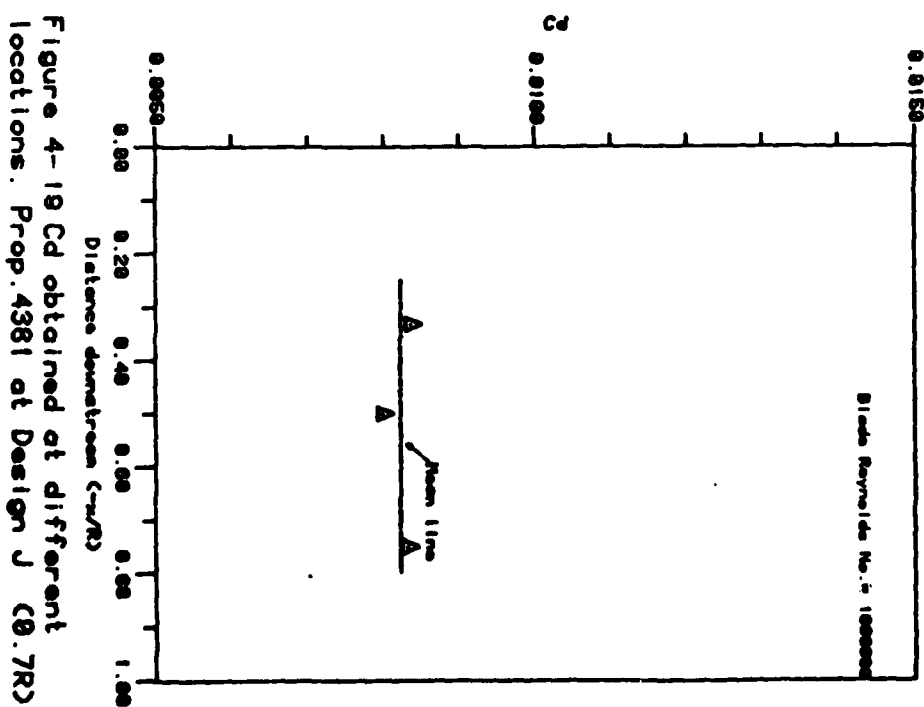


Figure 4-19 C_d obtained at different
locations. Prop. 4381 at Design J (0.7R)

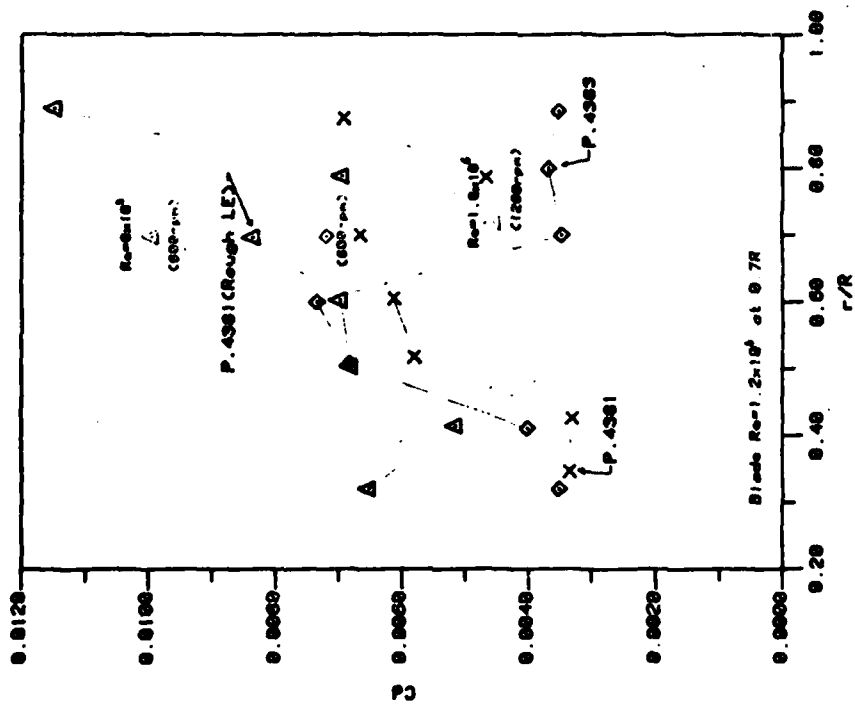


Figure 4-20 Coefficient of Profile Drag
Prop. 4381 and 4383 at Design J (900rpm)

FILMED
2-8